

Investigation into multifunctional nanoparticles for the detection, imaging and intervention of amyloid

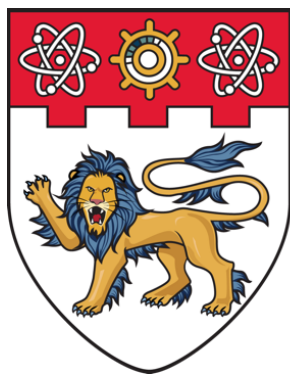
Xia, Yang

2019

Xia, Y. (2019). Investigation into multifunctional nanoparticles for the detection, imaging and intervention of amyloid. Doctoral thesis, Nanyang Technological University, Singapore.

<https://hdl.handle.net/10356/105529>

<https://doi.org/10.32657/10220/47843>



**NANYANG
TECHNOLOGICAL
UNIVERSITY**

SINGAPORE

**INVESTIGATION INTO MULTIFUNCTIONAL
NANOPARTICLES FOR THE DETECTION, IMAGING AND
INTERVENTION OF AMYLOID**

XIA YANG

SCHOOL OF MECHANICAL AND AEROSPACE ENGINEERING

2019

**INVESTIGATION INTO MULTIFUNCTIONAL
NANOPARTICLES FOR THE DETECTION, IMAGING AND
INTERVENTION OF AMYLOID**

XIA YANG

SCHOOL OF MECHANICAL AND AEROSPACE ENGINEERING

A thesis submitted to the Nanyang Technological University in partial fulfilment of
the requirement for the degree of Doctor of Philosophy

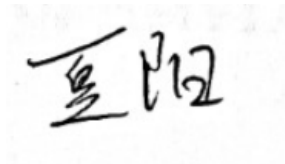
2019

Statement of Originality

I hereby certify that the work embodied in this thesis is the result of original research, is free of plagiarised materials, and has not been submitted for a higher degree to any other University or Institution.

7 Mar 2019

.....
Date

A handwritten signature in black ink, appearing to read 'Xia Yang' in Chinese characters, is placed above a dotted line.

.....
Xia Yang

Supervisor Declaration Statement

I have reviewed the content and presentation style of this thesis and declare it is free of plagiarism and of sufficient grammatical clarity to be examined. To the best of my knowledge, the research and writing are those of the candidate except as acknowledged in the Author Attribution Statement. I confirm that the investigations were conducted in accord with the ethics policies and integrity standards of Nanyang Technological University and that the research data are presented honestly and without prejudice.

11 Mar 2019

.....
Date



.....
Assoc/Prof Murukeshan Vadakke Matham
(Main supervisor)

11 Mar 2019

.....
Date



.....
Prof Balázs Gulyás
(Co-supervisor)

Authorship Attribution Statement

This thesis contains material from 2 papers published in the following peer-reviewed journal

Part of Chapter 2 is published as Y. Xia, V. M. Murukeshan, H. Su, P. Padmanabhan, and B. Gulyás, "Nanoparticulate Contrast Agents for Multimodality Molecular Imaging," *Journal of Biomedical Nanotechnology*, vol. 12, pp. 1553-1584, 2016. DOI: 10.1166/jbn.2016.2258

The contributions of the co-authors are as follows:

- A/P Murukeshan and Prof Gulyás suggested the research area.
- I collected and summarized the published state-of-the-art studies on multimodal nanoprobe.
- I prepared the initial manuscript draft along with Dr. Padmanabhan.
- Dr. Padmanabhan and A/P Su suggested required finer amendments
- A/P Murukeshan, Prof. Gulyás and Dr Padmanabhan reviewed and finalized the manuscript. All authors agreed on the corrected manuscript.

Chapter 4 is accepted to be published as Y. Xia, P. Padmanabhan, B. Gulyás, and V. M. Murukeshan, "Bottom-up Synthesized Biocompatible Carbon Dots for Alteration of A β 42 Fibrillization and Mitigation of Amyloid Toxicity," *Journal of Biomedical Nanotechnology*, 2019

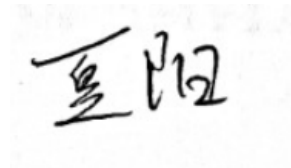
The contributions of the co-authors are as follows:

- A/P Murukeshan and Prof Gulyás provided the initial project direction.
- I designed and conducted the particle synthesis, characterized the particle using transmission electron microscopy, UV-Vis spectra, fluorescence spectra and Zeta-potential measurement.
- I carried out the biocompatibility assay, cell culture and cell staining work under the guidance from Dr. Padmanabhan.
- Confocal microscopy, including sample preparation, was conducted by me in the Lee Kong Chian School of Medicine.

- The initial manuscript was drafted by me. It was then reviewed, corrected and amended by Dr. Padmanabhan, A/P Murukeshan, and Prof. Gulyás.
- A/P Murukeshan, Prof. Gulyás and Dr Padmanabhan finalized the manuscript. All authors agreed on the corrected manuscript.
- A/P Murukeshan, Prof. Gulyás supervised the whole project as Joint supervisors.

7 Mar 2019

.....
Date



.....
Xia Yang

Acknowledgements

I would like to take this opportunity to acknowledge the help and guidance that I received from a number of respectable and warm-hearted people. Without these people, this PhD project cannot be carried out in the right direction.

First, I want to express my sincere appreciation to my PhD supervisor, **Assoc Prof. Murukeshan Vadakke Matham (School of Mechanical and Aerospace Engineering)** and **Prof. Balázs Gulyás (Lee Kong Chian School of Medicine)**, for providing me the research resources and valuable guidance for completing the thesis. Prof Murukeshan and Prof Balázs are both passionate and experienced scientists, who set models that I will strive to follow in my future life.

Next, I would to thank **Dr. Parasuraman Padmanabhan (Lee Kong Chian School of Medicine)**, who has patiently mentored me with his rich research expertise and helped me to solve many technical challenges using his experimental techniques. His continuous support was indispensable for me and without his support this work could not have taken place.

Also, I acknowledge the support that I received from the research staffs in the Centre for Optical and Laser Engineering (COLE-MAE) and the Translational Neuroscience Laboratory (LKCMedicine). By sharing knowledge and experience with me, they have significantly benefited the progress of my research work.

In addition, I acknowledge the support received through an NTU Research Student Scholarship.

Last but not least, I would like to express my deepest gratitude to my family and friends. The constant support that I received from them has encouraged me to overcome the numerous challenges that I came across during the whole PhD period.

Table of Contents

Acknowledgements	xiii
Table of Contents	ii
List of Figures	ii
List of Tables	viiv
Abbreviations	iviii
Abstract	ixiii
Chapter 1: Introduction	1
1.1. Background	1
1.2. Limitations of Current Amyloid Probes and Inhibitors	5
1.3. Objectives	7
1.4. Scope	8
1.5. Thesis Organization	10
Chapter 2: Literature Review	13
2.1. The Amyloid Cascade Hypothesis	13
2.2. Intracellular Amyloid	17
2.3. Intervention Strategies for A β peptides.	19
2.4. Molecular Probes for Amyloid Detection	22
2.4.1 Small Molecule Based Amyloid Probes	23
2.4.2 Nanoparticle Based Amyloid Probes	28
2.5. Multifunctional Nanoprobes	34
2.5.1. Design Principles for Multifunctional Nanoprobes	36
2.5.2. Nanoparticles for the Preparation of MFNPs	40
2.5.3. Targeting Ligands for MFNPs	43
2.6. Amyloid Aggregation Inhibitors	45

2.6.1. Small Molecule Inhibitors	46
2.6.2. Peptides Based Inhibitors	51
2.6.3. Nanoparticle Based Inhibitors.....	53
2.7. Outcome of Literature Review	58
Chapter 3: Bifunctional Nanoprobe for the Detection of Amyloid	61
3.1. Introduction	61
3.2. Design and Synthesis of RB-AuNPs	62
3.3. Characterization of RB-AuNPs	64
3.5. SERS Enhancement of RB-AuNPs	70
3.6. Interaction between A β 42 and RB-AuNPs	72
3.7. SERS detection of A β 42 peptides	75
3.8. Amyloid Detection in Transgenic Mice Brain Slices	77
3.8. Summary	81
Chapter 4: Carbon Dots based Amyloid Inhibitors.....	83
4.1. Introduction	83
4.2. Synthesis of C-dots	85
4.3. Characterization of C-dots	86
4.4. Biocompatibility and Cellular Uptake of C-dots.....	90
4.5. Alteration of the A β 42 fibrillization process.....	91
4.6. Summary	97
Chapter 5: Iron Oxide Nanoparticles for Specific Neuronal Cell Targeting.....	98
5.1. Introduction	98
5.2. Labelling A β 42 with Atto 647 dye	100
5.3. Functionalization and Characterization of IONPs.....	103
5.4. Specific Targeting to SH-SY5Y Cells	107
5.5. MR Relaxivity Measurement	109

5.5. Summary	112
Chapter 6: Conclusions and Suggestions for Future Research.....	113
6.1. Conclusions	113
6.2. Major Contributions.....	116
6.3. Suggestions for Future Research Directions	117
Appendix A. Methodology for the Synthesis and Application of RB-AuNPs	120
Appendix B. Methodology for the Synthesis and Application of C-dots	124
Appendix C. Sucrose Density Gradient Centrifugation for C-dots Separation.....	127
Appendix D. Labelling A β 42 peptides using CD-G	128
Appendix E. Methodology for the Preparation and Application of Atto647-A β 42-IONPs.....	129
List of Publications	132
References	133

List of Figures

Figure 1.1 Research Roadmap	10
Figure 2.1 The amyloid cascade hypothesis	15
Figure 2.2 Schematic illustration of the A β metabolism.....	17
Figure 2.3 Structures of Congo Red and Thioflavin T.....	25
Figure 2.4 The position of NIR optical window in the spectrum	27
Figure 2.5 Examples of fluorescent amyloid probes.....	29
Figure 2.6 B6-conjugated PEG-PLA NP for Enhanced Brain Delivery	31
Figure 2.7 NU4MNs labelling Tg mouse brain slices	31
Figure 2.8 Links between brain and skin amyloid	33
Figure 2.9 AuNP-based SERS sensor for amyloid oligomers (HypF-N)	34
Figure 2.10 Four MFNPs configurations	39
Figure 2.11 Schematic representation of amyloid aggregation process.....	46
Figure 2.12 Photo-induced inhibition of A β 42 using RB	50
Figure 2.13 Schematic representation for the curcumin-amyloid interaction	52
Figure 2.14 Interaction between AuNPs and A β fibrillization	56
Figure 2.15 Inhibition of A β 42 fibrillization using C-dots	57
Figure 3.1 Structure of RB	63
Figure 3.2 Scheme for the EDC/NHS facilitated conjugation.....	64
Figure 3.3 Morphology and zeta potential of RB-AuNPs.....	66
Figure 3.4 Optical properties of RB-AuNPs	68
Figure 3.5 Biocompatibility of RB-AuNPs	70
Figure 3.6 Raman spectra of RB, AuNPs and RB-AuNPs.....	72

Figure 3.7 Schematic illustration of the interaction between RB-AuNPs and A β 42	73
Figure 3.8 Fluorescence enhancement of RB-AuNPs and the effect of RB-AuNPs on ThT fluorescence.....	74
Figure 3.9 The morphology of 10 μ M A β 42 after 6 hours of incubation	75
Figure 3.10 A β 42 induced spectra changes of RB-AuNPs.	76
Figure 3.11 The relationship between Rpeak and A β 42 concentrations.....	78
Figure 3.12 Confocal imaging of transgenic mouse brain slices.	80
Figure 3.13 Raman mapping of mouse brain slices stained with RB-AuNPs.....	81
Figure 4.1 Scheme for the synthesis and purification of C-dots.....	87
Figure 4.2 TEM images and size distribution of CD-G (a and b) and CD-I (c and d).	88
Figure 4.3 (a) UV-Vis spectra of CD-G and CD-I, and the zeta potential of CD-G (c), and CD-I (c).....	89
Figure 4.4 Fluorescence spectra and emission map of CD-G (a and c) and CD-I (b and d).....	90
Figure 4.5 Biocompatibility and cellular uptake of C-dots.	91
Figure 4.6 ThT assay of 20 μ M A β 42 peptides when incubated with/without C-dots..	94
Figure 4.7 TEM images of amyloid fibrils after 24 hours incubation..	95
Figure 4.8 Schematic illustration of the interaction between A β 42 and C-dots.....	96
Figure 4.9 Mitigation of A β 42 toxicity..	97
Figure 5.1 Scheme for the labelling and purification of A β 42 peptides..	102
Figure 5.2 Fluorescence intensity for eluates after SEC purification	103
Figure 5.3 TEM image of Atto647-A β 42-IONPs.....	104
Figure 5.4 DLS measurement of IONPs and Atto647-A β 42-IONPs.....	106
Figure 5.5 Optical characterization of IONPs..	107

Figure 5.6 Cell viability assays for Atto647-A β 42-IONPs..	108
Figure 5.7 Prussian blue staining of SH-SY5Y cells..	109
Figure 5.8 Confocal images of SH-SY5Y and HCT-116 cells.....	110
Figure 5.9 MR images of Atto647-A β 42-IONPs and unconjugated IONPs..	111
Figure 5.10 T ₂ (a) and T ₁ (b) Relaxation curves of Atto647-A β 42-IONPs and unconjugated IONPs.....	112
Figure 6.1 Scheme for the designed animal model for in vivo test of RB-AuNPs.....	119
Figure 6.2 Scheme for the designed double-seeding model to investigate the interactions between IONPs and intracellular amyloid..	121
Figure C1 SDGC separation of CD-G.....	129
Figure D1 A β 42 fibrils labeled using A β 42-C-dots conjugates.....	130

List of Tables

Table 2.1 Advantages and disadvantages of commonly used molecular imaging modalities... ..	36
--	----

Abbreviations

AD	Alzheimer's disease
A β	Amyloid beta
APP	Amyloid precursor protein
A β 40	Amyloid beta peptides with 40 amino acids
A β 42	Amyloid beta peptides with 42 amino acids
PET	Positron emission tomography
SPECT	Single-photon emission computed tomography
MRI	Magnetic resonance imaging
SERS	Surface-enhanced Raman scattering
EPR	Enhanced permeability and retention
F-SERS	Fluorescent and surface-enhanced Raman scattering
FITC	Fluorescein isothiocyanate
3-APS	3-amino-1-propanesulfonic acid
C-dots	Carbon dots
AuNPs	Gold nanoparticles
IONPs	Iron oxide nanoparticles
RB	Rose Bengal
PEG	Polyethylene glycol
PEI	Polyethylenimine
PBS	Phosphate buffered saline
CD-G	PEG passivated C-dots

CD-I	PEI passivated C-dots
A β 42-IONPs	A β 42 functionalized IONPs
ACH	Amyloid cascade hypothesis
BACE	β -secretase
ADAM	A disintegrin and metalloproteinase domain
CTF	C-terminal fragments
APOE	Apolipoprotein E
NFT	Neurofibrillary tangles
MVBs	Multivesicular bodies
BBB	Blood-brain-barrier
HEK293	Human embryonic kidney cells 293
HCT116	Human colon cancer cells 116
CSF	Cerebrospinal fluid
SGSM	Selective γ -secretase modulators
CR	Congo red
ThT	Thioflavin T
PiB	Pittsburgh compound B
NIR	Near infrared
BODIPY	Boron-dipyrromethene
Nanoprobes	Nanoparticle based imaging probes
QD	Quantum dots
wt	Wild type
FRET	Fluorescence resonance energy transfer

MBA	4-mercaptobenzoic acid
MFNPs	Multifunctional nanoprobes
T ₁	Longitudinal relaxation
T ₂	Transverse relaxation
PL	Photoluminescent
UV-Vis	Ultraviolet-visible
CTAB	Cetrimonium bromide
TEM	Transmission Electron Microscopy
AFM	Atomic force microscopy
PDT	Photodynamic therapy
CHC	Central hydrophobic core
CNT	Carbon nanotube
MD	Molecular dynamic
PTT	Photothermal therapy
TiO ₂	Titanium dioxide
EDC	1-ethyl-3-(3-dimethylaminopropyl)carbodiimide hydrochloride
MES	4-morpholinoethanesulfonic acid
NHS	N-hydroxysuccinimide
MTT	3-(4,5-Dimethylthiazol-2-yl)-2,5-Diphenyltetrazolium Bromide
DMSO	Dimethyl sulfoxide
ROS	Reactive oxygen species
PEG-NH ₂	Amine terminated polyethylene glycol
PCC	Pearson's correlation coefficient

MWCO	Molecular weight cut-off
CPP	Cell-penetrating peptides
CTP	Cell-targeting peptides
SEC	Size exclusive chromatography
D/P	Dye/peptide ratio
DLS	Dynamic light scattering
PB	Prussian blue
RhB	Rhodamine B
SDGC	Sucrose density gradient centrifugation

Abstract

Amyloid is defined as insoluble, extracellular, proteinous aggregates formed by misfolding of proteins or peptides which are normally soluble. In the human body, amyloid is toxic and can cause cell death. Therefore, the presence of amyloid is linked with several diseases, including Alzheimer's disease (AD), spongiform encephalopathies and type II diabetes, which are also referred as amyloidosis. AD is one of the most well-known amyloidoses. In AD, the amyloid aggregates appear predominantly in the patients' brain, composed by a certain group of peptides known as amyloid beta (A β) peptides. Current clinical diagnoses of AD are primarily based on cognitive symptoms. However, it is often too late for intervention when the symptoms are detectable and there is no effective treatment for AD. On the other hand, the onset of amyloid aggregation may start years before the appearance of AD symptoms. Therefore, the detection and intervention of AD related amyloid at the molecular level are expected to be developed as powerful diagnostic and therapeutic methods for AD.

Nanoparticle facilitated therapy and diagnosis have recently achieved impressive success in biomedical researches, especially in oncology studies. Compared to small molecule based probes and drugs, nanoparticles are capable to generate more comprehensive diagnosis, enhanced therapeutic effect, and better specific targeting. However, the reported applications of nanoparticles for AD research are still limited. In this context, by identifying the aforementioned research gap, this thesis aims to investigate the potential of nanoparticles for the early detection, imaging, and intervention of amyloid. To fulfill this objective, three nanoparticles: gold nanoparticles (AuNPs), carbon dots (C-dots) and iron oxide nanoparticles (IONPs), have been selected due to their unique physiochemical properties.

Over the past decade, SERS spectroscopy has been utilized as a powerful analytical tool in chemistry, material science, and biomedical research. It is capable of revealing the conformational changes and structural differences between different molecules with high sensitivity. In addition, fluorescent imaging can be integrated with SERS spectroscopy as a comprehensive modality. In this thesis, a bi-functional SERS/fluorescent amyloid nanoprobe was prepared by conjugating Rose Bengal (RB) with AuNPs. Upon this conjugation, the characteristic Raman scattering of RB was significantly enhanced. Furthermore, when exposed to A β 42 peptides, a detectable change was observed in the SERS spectrum of the RB-AuNPs conjugates. Also, the interaction between RB-AuNPs and A β 42 induced fluorescence enhancement, which was utilized to perform *ex vivo* fluorescent imaging of amyloid plaques in transgenic mouse brains.

C-dots are quantum sized (<10 nm) photoluminescent (PL) carbon particles. Bottom-up synthesized C-dots were prepared by hydrothermal pyrolysis of sucrose. Two types of passivation agents were added prior to the pyrolysis to generate PEG passivated C-dots (CD-G), and PEI passivated C-dots (CD-I). Both types of C-dots were then used to modulate the fibrillization process of A β 42. Opposite effects were observed when mixing the two types of C-dots with A β 42 peptides: CD-G could promote A β 42 fibrillization while CD-I could inhibit it. Through a cell viability assay it was found that both types of C-dots could effectively reduce the cytotoxicity of A β 42 peptides. These findings demonstrate that C-dots hold a great potential as low-cost, biocompatible nanoinhibitors for AD treatment.

While most AD researches are focused on extracellular amyloids, intracellular amyloid is also playing a vital role in the pathogenesis of AD. The cellular uptake of extracellular amyloid by certain neuronal cells is a major source for intracellular amyloid build-up. To target these neuronal cells, dye labelled A β 42 peptides were conjugated with IONPs. The produced magnetofluorescent

IONPs shows enhanced and selective targeting of SH-SY5Y neuroblastoma cells. This research shows that A β 42 functionalized IONPs can be used as bifunctional nanoprobe to interrogate the cellular uptake of amyloid.

In general, this PhD thesis investigated the synthesis and utilization of multifunctional nanoparticles for the detection, imaging, and intervention of amyloid. It is envisaged that the results and research outcomes detailed in this thesis can lead to the realization of such nanoparticle-based amyloid probes for the diagnosis, and inhibitors for the treatment, of AD

Chapter 1: Introduction

This chapter begins with the background of, and motivation for, undertaking this research, followed by a brief introduction to the amyloid cascade hypothesis which explains the pathological mechanism of Alzheimer's disease. The importance and challenges in developing diagnostic and therapeutic agents for AD are also explained. The objectives and scope of this thesis are outlined, and the designed research roadmap for achieving the objectives is presented. The chapter concludes with a description of the thesis' organization.

1.1. Background

Alzheimer's disease (AD) is the leading cause of dementia, responsible for 60% to 70% of recorded dementia cases. The early symptoms of AD include short-term memory loss, difficulty in problem-solving, mood swinging and disorientation. At the advanced stage, patients will lose the capability of walking and swallowing. The ultimate consequence of AD is fatal, and the average post-diagnosis life is three to nine years [1]. Like many other neurodegenerative diseases, AD is a chronic disease where the risk of getting the disease increases with age. Therefore, with a progressive increase of older people in the world population, AD is projected to become a more severe health threat, especially in developed countries, in which the life expectancy is usually greater than 80 years [2].

One of the pathological hallmarks of AD is the abnormal aggregation of amyloid beta ($A\beta$) peptides. These peptides are produced by proteolytic cleavage of a transmembrane protein called the amyloid precursor protein (APP). $A\beta$ peptides have various lengths depending on the site of cleavage, but most $A\beta$ peptides are those with 40 ($A\beta_{40}$) or 42 ($A\beta_{42}$) amino acids. Once produced, the $A\beta$ peptides have a high tendency to assemble into oligomers and to further develop into large insoluble plaques. The processing of APP is a fundamental cellular process in the brain throughout life. The difference between the physiological and pathological processes is that whereas in young

and healthy individuals the normal metabolism could rapidly clear the produced A β peptides before they can form aggregates, in aged and diseased brains A β peptides are deposited due to an increased production rate or/and a decreased clearing/transportation rate [3]. In addition to this, a various toxic metabolites are also produced during the amyloid aggregation process, and this eventually leads to the death of neurons [4].

Conventionally, the clinical diagnosis of AD is mainly based on the observation of behavioral changes and cognitive tests. Sometimes, brain-imaging techniques are also used, since the deposition of amyloid plaques is capable to induce conformational changes in the patients' brain. However, the onset of amyloid aggregation may start a decade before the appearance of detectable symptoms. Therefore, it is often too late to conduct efficient therapeutic methods to reverse, retard or stop the pathological development of AD after a determinative diagnosis has been made [5].

Recently, molecular imaging of amyloid beta peptides has shown a great potential in the early diagnosis of AD [6]. In the bio-imaging field, molecular imaging refers to techniques that are capable to reveal biological activities at cellular and subcellular levels. These techniques usually utilize specially designed molecular probes that target certain disease-related biomarkers. For AD diagnosis, a series of molecular probes has been reported capable of identifying and visualising A β peptides, fibrils, oligomers, tau proteins or plaques as biomarkers. These probes have been applied for amyloid detection in positron emission tomography (PET), single-photon emission computed tomography (SPECT), fluorescence imaging and magnetic resonance imaging (MRI) [7].

The detection of soluble A β in body fluids is another challenge that researchers are actively working on. One of the emerging protein detection techniques is based on the Surface-enhanced Raman scattering (SERS). SERS is a phenomenon which shows dramatically enhanced (10^2 - 10^{10}

factors) Raman scattering when molecules are present in the close vicinity of nanostructures consisting of certain noble metal, transition metal, or semiconductors [8]. The most widely accepted explanation for SERS is based on the enhancement of the electromagnetic field provided by the metal surface. When the incident laser strikes the nanostructure, the surface plasmons are excited and then emit a dipole field that can coherently interact with the incoming light. This interaction leads to a re-distribution of the electric field intensity around the nanostructure. Molecules that are close enough to the nanostructures will be exposed to an enhanced excitation light and will consequently produce stronger Raman signals. Once the Raman signals are produced, their electromagnetic field undergoes the same enhancement process as the exciting light. The extraordinary high magnification of SERS effect is actually a result of a two-time enhancement [9]. Over the past decade, SERS spectroscopy has been utilized as a powerful analytical tool in chemistry, material science, and biomedical research. It is capable of revealing the conformational changes and structural differences between different molecules with high sensitivity. However, for protein detection, some obstacles still exist. First of all, significant SERS effect is generally restricted within 2 nm around the surface of nanostructures, therefore hinders the direct detection of large biomolecules such as protein [10, 11]. In addition, the intrinsic molecular and conformational complexity of proteins often generates complicated spectral patterns, which makes it very difficult to identify the characteristic Raman fingerprints. The protein-probes interactions may vary due to the different surrounding media, which lead to a low batch-to-batch reproducibility [10, 12]. To overcome the aforementioned limitations, an indirect SERS strategy has been proposed: instead of interrogating the Raman signals from the proteins, an additional Raman reporter with large Raman cross-section can be attached to the nanostructures and the reporter is allowed to react with the target protein in order to generate detectable changes in the

Raman spectra [13, 14]. This type of SERS probes has been successfully applied to detect DNA, protein and other bio-molecules [15].

Apart from diagnostic applications, A β peptides are also actively studied in order to develop effective therapies for AD. Currently, several drugs have been approved by regulatory authorities to be used in the clinical treatment of AD, but they only provide temporary relief from symptoms. No treatment has been proved effective to stop the progression of AD [16]. A β -targeting therapeutic agents are normally designed to achieve one of the following effects: to reduce the production of A β peptides, to enhance the clearance of A β peptides or to prevent the aggregation of A β peptides. A variety of effective inhibitors has been found by the screening of peptides [17], protein [18], antibodies [19], organic dyes [20, 21], and other small molecules [22, 23].

In addition to the small molecular-based inhibitors, nanoparticles based inhibitors have also attracted growing interests in recent years. The advantages of nanomedicines include the large surface area for drug load, prolonged circulation time, and better specific targeting. Particularly, nanotherapy has achieved impressive progress in cancer treatment. One reason for that success is attributed to the enhanced permeability and retention (EPR) effect of nanoparticles: the leaky neovasculature and low-effective lymphatic drainage of tumor tissue causing a passive accumulation of nanoparticles in the tumor tissue. In addition, the large loading area of nanoparticles has made it possible to conjugate contrast agents and therapeutic agents into one particle to produce a multifunctional particle that can simultaneously function as imaging probe as well as nanomedicine. This concept is now known as theranostics. In contrast to the conventional “diagnostics followed by therapy” approach, theranostics helps to eliminate the discrepancy in bio-distribution and selectivity between separated imaging and therapeutic agents. The ultimate goal of theranostics is to shift the current generalized medicine, which applies similar

therapy to all patients with the same disease, into an era of personalized medicine, i.e. tailor-made therapy for an individual patient [24]. Encouraged by the successful application of nanoparticles, researchers have started to develop nanotherapy for AD treatment. A series of therapeutic nanoparticles has been reported, either to inhibit the aggregation of A β peptides or to facilitate the ablation of A β aggregates [25, 26].

1.2. Limitations of Current Amyloid Probes and Inhibitors

Regarding MRI amyloid probes, the most crucial limitation is the relatively low spatial resolution of MRI, therefore, it can only be applied to detect large amyloid plaques that only appear at the late stage of AD [27]. Compared to MRI, radioisotope based imaging techniques such as PET and SPECT could provide much higher resolution and sensitivity. So far, the most advanced progress in the field of A β molecular imaging probes is achieved with PET. Several ^{18}F -based PET probes have been introduced to clinical diagnosis since 2012 [28, 29]. However, the high-cost of instruments and the inevitable radiation exposure have limited wide applications of PET, especially for the early diagnosis of AD, which requires large-scale screening of potential patients with high AD risks. SPECT imaging has a broader availability and lower costs due the relatively easier preparation and longer half-life of SPECT radioisotopes ($[^{125}\text{I}]$, $t_{1/2} = 60.1$ days, $[^{123}\text{I}]$, $T_{1/2} = 13.2$ hours, and $[^{99\text{m}}\text{Tc}]$, $T_{1/2} = 6.0$ hours), but the concern of radio exposure still exists. In addition, the current available AD SPECT probes exhibit high background signals due to their high lipophilicity and nonspecific binding, which in turn reduce the sensitivity and precision of SPECT diagnosis.

Another problem with the currently available amyloid probes is that in most cases they are designed to work for a single modality. To achieve a comprehensive diagnosis, it is often necessary to use multiple diagnostic techniques in the patients. For example, optical imaging is highly

sensitive and can achieve a temporal resolution in the second scale, but its spatial resolution and *in vivo* penetration depth are limited. On the other hand, MRI is capable to achieve high spatial resolution and theoretically infinite penetration depth. By combining these two modalities, high resolution and excellent sensitivity can be obtained simultaneously. Whereas great efforts have been made to design hybrid molecular imaging instruments (e.g. PET/CT and PET/MRI system [30]), the requirement of a single probe with multiple signaling capacities has arisen. Compared to individual single modality contrast agents, multimodality probes provide better image registration, consistent pharmacokinetics and reduced administration load for the patient.

SERS probes have been used for bio-imaging applications such as cell labeling, tissue diagnosis and *in vivo* imaging on small animal models [31]. While SERS based Raman imaging shows great advantages in terms of sensitivity and multiplexing capability, the long image acquisition time and the requirement of post-processing have limited the temporal resolution of Raman imaging [32]. To overcome this limit and also extend the capability of SERS probes, other imaging moieties, including fluorescent imaging [32-34], MRI [35] and X-ray CT [36], have been integrated with SERS. Such integrations of modalities generated a requirement of multifunctional SERS probes. Among these multifunctional SERS probes, the fluorescent SERS (F-SERS) probe is the most well studied probe. One reason is that fluorescence imaging is an intuitive method and can achieve real-time image acquisition, which makes it an ideal complementary imaging modality for Raman imaging. Another advantage of F-SERS probes is that many fluorescent dyes, such as fluorescein isothiocyanate (FITC) [33] and Rhodamine B derivatives [37], can be readily used as Raman reporters when they are conjugated with nanostructures, which makes the preparation of F-SERS probes more facile. Whereas F-SERS probes have been used for tumor imaging, there are only a few reported F-SERS probes that have been reported for amyloid detection.

Conventionally, amyloid aggregation inhibitors have been developed based on small molecules such as organic molecules and peptides. However, few of them have entered into a clinical trial due to their low efficacy. 3-amino-1-propanesulfonic acid (3-APS, AlzhemedTM, tramiprosate) is the only inhibitor that reached phase III trials, but the results turned out to be disappointing and the further trial was suspended after 2007 [38]. The failure of these inhibitors is attributed to the low blood-brain-barrier permeability, the complexity of their synthesis and the low *in vivo* stability [39]. Recently, the usage of nanoparticles as amyloid inhibitors has been attracting increasing interest in the research community. Compared to small molecules inhibitors, nanoinhibitors can achieve stronger inhibition efficacy, longer circulation, and better amyloid targeting. However, most of the reported nanoinhibitors are prepared based on metallic nanoparticles, which may induce neurotoxicity [40]. Non-metallic nanoparticles such as carbon dots (C-dots) might be a more appropriate choice for amyloid inhibitors. Currently, the interactions between C-dots and A β peptides are poorly investigated. Only one study has reported the use of C-dots as amyloid inhibitor, and the C-dots used in that research is obtained from top-down synthesis. The other preparation approach, bottom-up synthesis, has not been used to prepare C-dots-based amyloid inhibitor.

1.3. Objectives

Currently, most of the reported amyloid nanoprobe are designed to target the extracellular amyloid. Intracellular amyloid, which also plays a crucial role in the pathogenesis of AD [41], has not been well investigated. One major source of intracellular amyloid is the uptake of extracellular amyloid by neuronal cells. Logically, the detection of this cell uptake event can help the diagnosis of AD. However, no nanoprobe have been reported to interrogate this event. Further, limitations of the current state of arts, concepts, and methodologies used for amyloid detection and inhibition are detailed in the previous section. Based on these perspectives, the main objectives of this

research are directed towards the investigation on novel multifunctional nanoparticles that can be used for amyloid detection and intervention. These include:

- a) Investigation into the research and development of SERS-fluorescent bi-functional nanoprobes for amyloid diagnosis. Research will also investigate the efficiency of the nanoprobes to exhibit detectable changes when they interact with amyloid beta.
- b) Investigation into facile approaches to synthesize C-dots for their use as amyloid inhibitors. The effect of passivation agents should also be explored in order to optimize the inhibition efficacy.
- c) Research and development of functionalized IONPs as nanoprobes that can selectively enhance the targeting of neuronal cells which are involved in the cellular uptake of amyloid.

1.4. Scope

To meet the aforementioned objectives, the planned research scope is summarized as follow:

1. Design and synthesis of a SERS-fluorescent bi-functional nanoprobe that can be used for amyloid diagnosis:
 - Design and synthesizes of Rose Bengal (RB) conjugated AuNPs through carbodiimide crosslinking reaction.
 - Characterization of the conjugated RB-AuNPs in terms of morphology, optical properties, SERS property, and biocompatibility.
 - Investigation of the interaction between RB-AuNPs and A β 42 peptides and demonstration of SERS-based detection of A β 42 peptides.
 - Conceptualization and development of a Raman mapping strategy to distinguish amyloid-containing mice brains.

- Study and analysis on RB-AuNPs as fluorescent probes for the imaging of amyloid plaques in transgenic mice brains.
2. Explore the potential of bottom-up synthesized C-dots as amyloid inhibitors:
- Design and optimization of a bottom-up synthesis approach to prepare C-dots with two different passivation agents.
 - Characterization and elucidation of optical properties of C-dots with UV-Vis and fluorescence spectrometer.
 - Investigation into the cellular uptake of C-dots by neuronal cells.
 - Research into the intervention of amyloid aggregation induced by C-dots, monitored through dye-binding assay and electron microscopy.
 - Experimental demonstration and validation on the mitigation of amyloid toxicity by C-dots through cell proliferation assay.
3. Investigation into the cellular uptake of amyloid peptides using nanoprobe:
- Design and fabrication of a magnetofluorescent nanoprobe by conjugating dye-labeled amyloid peptides with IONPs.
 - Examine the morphology, optical properties, and biocompatibility of the functionalized IONPs.
 - Conceptualization of an SH-SY5Y cell model to study the cellular uptake of A β 42 and demonstration of specific neuron targeting by the IONPs.
 - Application of IONPs for contrast enhancement in MR imaging of phantom samples.

As shown in Figure 1.1, a detailed research roadmap is plotted to illustrate all the essential research tasks in this thesis.

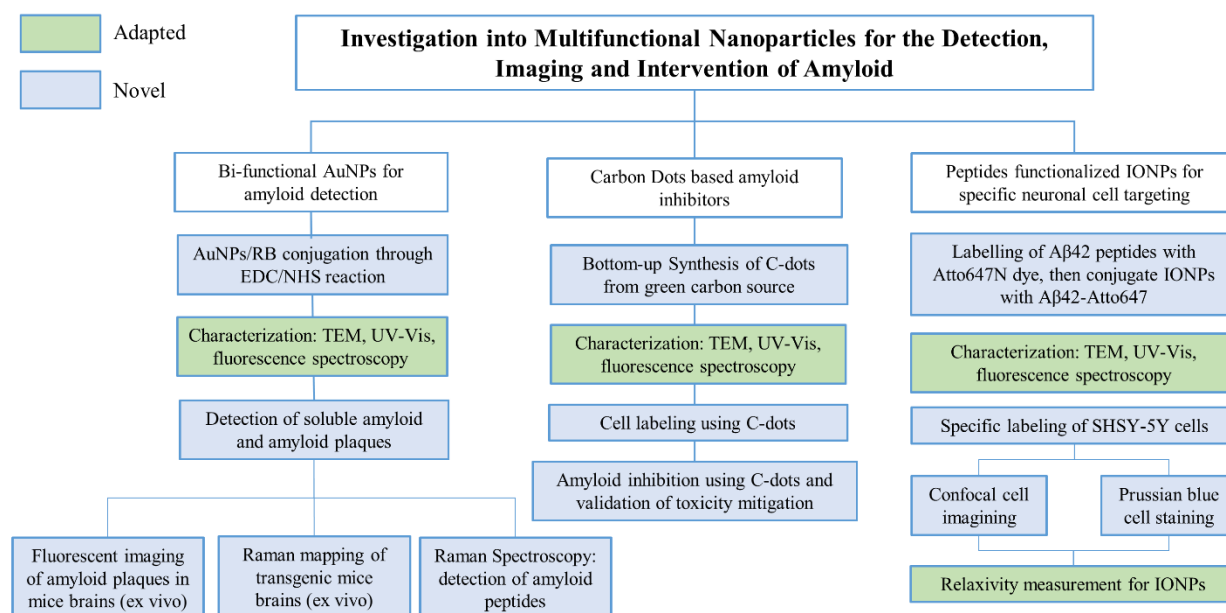


Figure 1.1 Research Roadmap

1.5. Thesis Organization

This thesis has 6 chapters:

Chapter 1 introduces the background and motivation for undertaking this research project, followed by a brief introduction of the amyloid hypothesis for Alzheimer's disease. The importance and challenge of the development of diagnostic and therapeutic agents for AD were also explained. The objectives and scope of this thesis are outlined, and the designed research roadmap for achieving the objectives is presented. The chapter ends with a description of the thesis' organization.

Chapter 2 is a literature review chapter that summarizes the reported researches related to the scope of this thesis. It starts with an introduction to the Amyloid Cascade Hypothesis, which states that the deposition of amyloid peptides is the central event for the pathological development of AD. The second part of this chapter talks about the molecular probes and sensors that are targeting amyloid peptides. The design principle and targeting mechanism of these probes are discussed in detail. The following part elaborates the concept of multimodal molecular probe and its advantages

over monomodal probes. The role of nanoparticles is particularly emphasized as the platform for the preparation of multimodal probes. The fourth part of this chapter introduces the development of nanoparticle based amyloid inhibitors for the treatment of AD. The idea of theranostic agents, in which diagnostic and therapeutic agents are combined, is addressed. The outcomes of literature reviews are presented at the end of this chapter.

Chapter 3 describes the development of a Raman/fluorescent bi-functional nanoprobe that can be used for the detection of amyloid. This nanoprobe prepared by conjugating gold AuNPs with Rose Bengal (RB) dye. RB is chosen due to its unique Raman fingerprints and affinity with A β peptides. The morphology and optical properties of the nanoprobe have been analyzed through comprehensive characterization techniques. Particularly, the SERS effect of the nanoprobe is discussed in detail. The interaction between nanoprobe and A β 42 are carefully investigated. Upon binding with A β 42 peptides, a spectrum change was detected in the nanoprobe's Raman spectrum, and the magnitude of the spectrum changes can be correlated with the concentration of target peptides. The peptide/probe interaction also induced a remarkable enhancement in the probes' fluorescence emission. This fluorescence enhancement was further utilized to image amyloid plaques in the brain slices from transgenic mice.

Chapter 4 elaborates the possibility of C-dots as amyloid inhibitors. Two types of C-dots were synthesized through a bottom-up process, in which sucrose is hydrothermally pyrolyzed using microwave irradiation. Two types of passivation agents were added prior to the pyrolysis to generate polyethylene glycol (PEG) passivated C-dots (CD-G) and polyethylenimine (PEI) passivated C-dots (CD-I). Inhibition assays where A β 42 peptides were incubated with CD-G or CD-I show that CD-G could promote A β 42 fibrillization while CD-I could inhibit it. Cell viability assays further revealed that both types of C-dots could effectively reduce the cytotoxicity of A β 42

peptides. The observed results suggest that passivation agents used in the synthesis of C-dots play vital roles in the interactions between C-dots and amyloid peptides, and bottom-up synthesis holds a great potential as a facile and low-cost method for the preparation of C-dots-based amyloid inhibitors.

Chapter 5 discusses the utilization of IONPs for the specific targeting of SH-SY5Y cells. The chapter begins with the description of the preparation of A β 42 functionalized IONPs (A β 42-IONPs). The A β 42 peptides were first labelled with Atto 647 dyes and then conjugated with amine-functionalized IONPs. Due to the pre-labeled Atto 647 dyes, the as-prepared A β 42-IONPs is magnetofluorescent. When incubated with SH-SY5Y cells, the cellular uptake of A β 42-IONPs was enhanced, compared with bare IONPs. Further, by labelling SH-SY5Y and HCT-116 cells, it was found that the A β 42-IONPs are selectively targeting the neuronal cells. This enhanced and specific neuronal targeting is attributed to the cellular uptake of extracellular amyloid by SH-SY5Y cells. In addition, the ability of the A β 42-IONPs as MR contrast agents is preserved after the peptide functionalization. The experimental results suggest that the A β 42 functionalized magnetofluorescent IONPs can be used as a bimodal probe to interrogate the cellular uptake of amyloid.

Chapter 6 is the conclusion chapter. It summarizes the major contributions that are made as part of this thesis, followed by suggestions for future research directions.

Chapter 2: Literature Review

This chapter briefly reviews the previous works reported in the literature that are related to the proposed research. The chapter begins with an introduction of the Amyloid Cascade Hypothesis, which states that the deposition of amyloid peptides is the central event for the pathological development of AD. The second part of this chapter is about the molecular probes and sensors that are targeting amyloid peptides. The design principle and targeting mechanism of these probes are discussed in detail. The following part elaborates the concept of multimodal molecular probes and their advantages over monomodal probes. The role of nanoparticles is particularly emphasized as the platform for the preparation of multimodal probes. The fourth part of this chapter introduces the development of nanoparticle based amyloid inhibitor for the treatment of AD. The idea of theranostic agents, in which diagnostic and therapeutic agents are combined, is addressed. The outcome of literature reviews is presented at the end of this chapter.

2.1. The Amyloid Cascade Hypothesis

AD was first systematically reported as a presenile dementia syndrome by a German psychiatrist, Alois Alzheimer, in 1907, and therefore this disease is named after Dr. Alzheimer [42]. Shortly after that, scientists started to recognize a close correlation between the onset of dementia and the deposition of abnormal proteins in the brain. Amyloid is one of the most important forms of proteinaceous aggregates found in AD patients. Amyloid is actually discovered much earlier than AD. The name amyloid means ‘starch’ in Latin, and it comes from a misidentification by Rudolf Virchow, who believed that amyloid is composed of carbohydrates. Later studies defined amyloid as an extracellular, proteinaceous deposit with rich β -sheet structure. Amyloid can be found throughout the whole body and are considered relevant to a group of diseases known as amyloidoses.

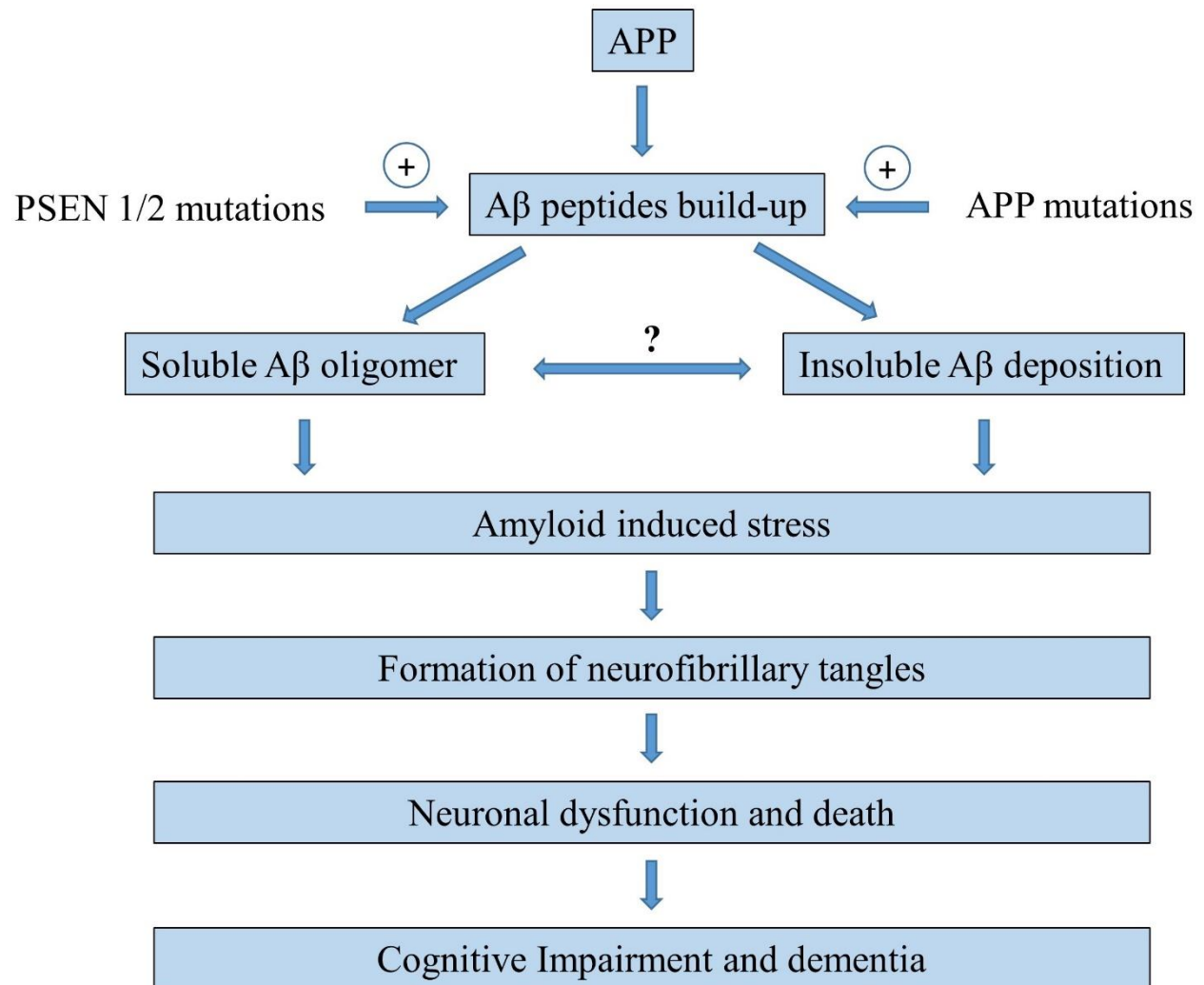


Figure 2.1 The amyloid cascade hypothesis. The aggregation of Aβ peptide is considered as the central step for the development of AD. Adapted from reference [43].

Although the interrogation of AD and amyloid started more than a hundred years ago, the exact mechanism that links AD and amyloid remained a mystery until the 1990s. The development of molecular biology revealed that brain amyloid is composed of Aβ peptides. And the latest genetic technologies helped to identify that the mutation of the amyloid precursor protein (APP), presenilin 1 (PSEN 1), and presenilin 2 (PSEN 2) genes are responsible for familial AD [44-46]. With all these new findings, the amyloid cascade hypothesis (ACH) was first proposed in 1992 to explain

the pathological progression of AD at molecular level. It soon became the most widely accepted model for AD. As shown in Figure 2.1, the ACH considers the deposition of cerebral A β peptide as the fundamental event that eventually causes AD. The mutations in the aforementioned three genes lead to an enhanced A β aggregation. Mutation in the APP gene leads to a promoted expression of APP, which is the raw material for A β production. First, APP is cleaved by α -secretase or β -secretase (BACE). Proteolysis by the α -secretase is the major cleavage reaction and it is executed by one of several members of the ADAM (a disintegrin and metalloproteinase domain) protease family. BACE cleaves APP at the N-terminal boundary of the A β peptide domain. Both α - and β -secretase produce membrane-bound C-terminal fragments (CTF) that later undergo further proteolysis known as the γ -secretase to produce the final A β peptides [47]. Mutations in PSEN1 and PSEN2 promoted the formation of the catalytic active site of γ -secretase. Another important gene that affects the A β aggregation is the apolipoprotein E (APOE) gene. There are three different alleles of APOE in human: APOE2, APOE3, and APOE4. The APOE proteins were found playing a central role in the clearance of A β peptides. Therefore, a mutation in APOE genes may cause an insufficient clearance of cerebral A β peptides and consequently promotes the aggregation [48]. The original hypothesis stated a linear pathway that starts with an imbalanced A β formation/clearance and ends with dementia. That means that the neurotoxicity of amyloid should increase linearly with the aggregation process of A β . But recent studies have shown that the actual relationship between A β deposition and cognitive degradation is not linear. Diffusible ligands that are derived from A β peptides and soluble oligomers that are formed during the A β aggregations are now deemed as the major contributors for the neuron death of AD patients [49, 50]. Therefore, the modified ACH now suggests that synaptotoxicity and neurotoxicity are induced mainly by the soluble intermediates formed during the aggregation process. Unfortunately, the

vibrant nature of these multimeric species and the poorly defined mechanism of amyloid toxicity still cause some ambiguity. For probe and drug development, the ambiguity is reflected by the diversified selection of biological targets, which ranges from soluble A β monomers to mature form of amyloid fibrils.

Another modification of the original ACH is the addition of neurofibrillary tangles (NFTs). NFTs is another hallmark for AD, they are intracellular aggregates formed by hyperphosphorylated tau proteins inside neurons. When they form, they normally fill the cell body and take its shape. The main structure of NFTs is the paired helical filaments. Conventionally, amyloid aggregation and NFT formation are considered as two separated processes. But recently transgenic studies found that certain types of monomeric A β peptides can induce the aggregation of tau proteins [43].

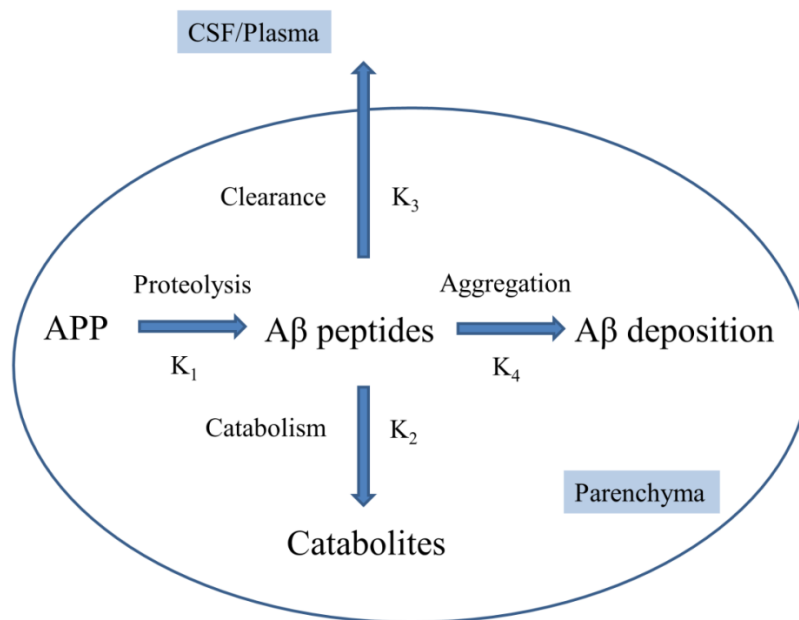


Figure 2.2 Schematic illustration of the A β metabolism. The steady-state amount of cerebral A β peptides is a function of the APP amount, the rate constants for APP proteolysis, [K_1], in-brain degradation, [K_2] and out-of-brain clearance, [K_3]. And the amount of A β deposition is a function of available A β peptides.

The kinetic of the cerebral amyloid metabolism is illustrated in Figure 2.2, K_1 , K_2 , K_3 , and K_4 represent the rate constants for production, in-parenchyma degradation, out-of-brain clearance and aggregation of $A\beta$ peptides respectively. To simplify the model, all these rate constants are assumed to be independent of each other. In addition, the aggregation process of $A\beta$ peptides is assumed to be a perfect reaction that no $A\beta$ is lost during the reaction. The relationship between the densities of [APP] and [$A\beta$ peptides] can be expressed in the following formula [3, 43]:

$$[A\beta \text{ peptides}] = K_1 / (K_2 + K_3) \times [APP] \quad \dots\dots\dots 2.1$$

In addition, the amount of aggregated $A\beta$ can be expressed as

$$[A\beta \text{ deposition}] = K_4 \times [A\beta \text{ peptides}] \quad \dots\dots\dots 2.2$$

Combining Formula 2.1 and 2.2, it can be deduced that:

$$[A\beta \text{ deposition}] = (K_4 \times K_1) / (K_2 + K_3) \times [APP] \quad \dots\dots\dots 2.3$$

From Formula 2.3, it is logical to conclude that increases in the rate constant for production (K_1) and aggregation (K_4), or decreases in the rate constants for degradation (K_2) and out-of-brain clearance (K_3) can lead to an elevated $A\beta$ deposition.

2.2. Intracellular Amyloid

$A\beta$ was initially identified as the component of extracellular amyloid plaques. However, the presence of $A\beta$ is not limited to the extracellular matrix. Intracellular $A\beta$ peptides were first discovered in the late 1980s by Grundke-Iqbal et al. [51] Their study also suggested that the occurrence of intracellular $A\beta$ is an age-independent event since intracellular $A\beta$ peptides were found in participants in different ages, from 38 to 83 years old. After this first reported study, a considerable amount of researches have been carried out on intracellular $A\beta$ in order to reveal their connections with AD. With the help of C-terminal-specific antibodies, it is now clear that the major component of intracellular is $A\beta_{42}$ instead of $A\beta_{40}$ [52]. Animal studies on transgenic mouse

models suggest that the build-up of intracellular A β may cause the onset of AD pathogenesis [41]. Similarly, in patients with Down syndrome, the accumulation of intracellular A β has been found to take place before the deposition of extracellular A β plaques [53]. All these findings indicate that the build-up of intracellular A β may be an early event during the pathological progression of AD. However, the exact role of the intracellular A β is not fully understood. Electron microscopy on immunogold labeled neuronal cells has shown that A β 42 can accumulate in multivesicular bodies (MVBs) [54]. Further studies show that A β 42 can cause MVB disruption by inhibiting the ubiquitin–proteasome system [55]. This proteasome dysfunction has been associated with the build-up of tau protein. Additionally, the blocking of proteasome leads to elevated A β concentration, suggesting that proteasome is involved in the clearance of A β [56]. In another study on transgenic mice (Tg2576), A β was also observed in mitochondria. The accumulation of mitochondrial A β was associated with the downgraded activity of respiratory chain complexes and decreased consumption of oxygen. This finding provides an explanation for mitochondrial defects observed in many AD animal models [57]. Furthermore, the presence of intracellular A β is also linked with synaptic dysfunction in AD, based on the fact that A β oligomers could induce a deficit in long-term potentiation [58].

The aforementioned studies prove that the existence of intracellular A β is common in AD patients, however, the origin of this intracellular A β is still not fully understood. As mentioned earlier, A β peptides are produced by protease cleavage of their parent protein APP. Although mainly located on the cell membrane, APP can also be found in the membranes of organelles such as Golgi apparatus, endoplasmic reticulum, endosomal, lysosomal and mitochondria [56]. Cleavage of APP in organelles is occurring concurrently with the cleavage of APP in cell membranes but in a much smaller scale. This intracellular proteolysis leads to the production of

intracellular A β . Interestingly, while extracellular A β peptides can be produced by cells across the whole body, intracellular production of A β peptides is limited to neuronal cells [59].

Besides intracellular production, there is another possibility that the extracellular A β could be internalized by cells in order to build the intracellular amyloid aggregates. By binding with reporters, A β can be taken up by neuronal cells and even pass through the blood-brain-barrier (BBB) [60, 61]. In animal studies carried out by Clifford et al. [62], mice were first injected with pertussis toxin in order to permeabilize the mice BBB. Next, fluorescein isothiocyanate (FITC)-labeled A β 42 and A β 40 peptides were introduced via tail vein injection. Both types of A β peptides were found accumulated in the brain neuronal cells. This study shows the possible communication between cerebral and peripheral amyloid.

Once internalized by neuronal cells, extracellular A β can act as a “seed” that promotes the intracellular production and aggregation of amyloid. In the work reported by Hu et al. [63], A β peptides and A β fragments were labeled with FITC and then incubated SH-SY5Y neuroblastoma cells. By detecting the fluorescence from the FITC using confocal microscopy, a selective A β uptake by SH-SY5Y cells but not by human embryonic kidney cells (HEK293) was observed. On the other hand, scrambled A β was not internalized by SH-SY5Y cells, indicating that such kind of internalization is a sequence-specified event. Further electrophoresis analysis of the cells’ lysate showed that high molecular weight aggregates are formed inside the cells.

2.3. Intervention Strategies for A β peptides.

With the wide acceptance of ACH, four strategies have been developed to conduct therapeutic interventions for AD, which correspond to the 4 rate constant mentioned in 2.1, they are:

- a) Reducing A β production,
- b) Accelerating A β clearance,

- c) Facilitating A β degradation,
- d) Inhibition of A β aggregation.

It is necessary to point out that there is still a considerable uncertainty about the amount of A β peptides that are deposited in human AD brains and the density of A β varies in different regions of the brain.

Reducing A β production rate: Several successful studies have been reported to reduce the A β production either by decreasing BACE activity or by inhibiting γ -secretase. BACE participate in the initial stage of APP processing and γ -secretase is playing the pivotal role at the final stage of amyloidogenesis which leads to the production of A β 40 and A β 42 peptides. However, these inhibitors are suffering from severe substrate promiscuity. Apart from A β production, both BACE and γ -secretase are responsible for the production of other proteins that are essential cell proliferation, development, differentiation, and cellular communication [64, 65]. Therefore, the major concern when applying these inhibitors is the off-target side effects. One typical example is Semagacestat (LY450139), a γ -secretase inhibitor that decreased A β levels in blood and cerebrospinal fluid (CSF). However, the clinical trial on over 3000 patients generated devastating results. The patients were reported to exhibit worsened cognition and declined ability for daily life. Other side effects include weight loss and increased risk for skin cancer [66]. In order to avoid these side effects, the idea of selective γ -secretase modulators (SGSM) is proposed. As its name suggests, instead of general enzyme inhibition, SGSMs are designed to inhibit only the APP processing reactions, leaving other signaling pathways intact [67]. While a few potential SGSM has been reported, none of them have achieved meaningful success in clinical trial [68].

Accelerating A β clearance: The clearance of A β towards the peripheral circulation is regulated by the following factors:

- a) Low-density lipoprotein receptor-related protein: increases A β outflow from the brain to the blood.
- b) Receptor for advanced glycation end products: enhances the transport of A β across the BBB.
- c) Apolipoproteins: A β can be transported into the brain by binding with APOE.

Currently, therapies based on this mechanism are focused to reduce cerebral amyloid load by enhancing the out-of-brain transportation of A β and by preventing the transportation of peripheral A β toward the cerebral circulation. However, there is a continuous debate on the importance of out-of-brain transport. Studies have shown that A β in the brain and in the CSF or plasma are poorly correlated with each other in AD patients [69].

Facilitating A β degradation: Compared to the out-of-brain transport, the in-brain degradation of amyloid has been considered as a more important event in the build-up of amyloid by some researchers [3]. Brains are rich sources of various peptidases, including neprilysin, plasmin, endothelin converting enzyme, insulin-degrading enzyme, angiotensin-converting enzyme, and metalloproteinases [70]. These peptidases can readily proteolyze A β peptides as long as they are accessible to the A β . Recent studies even suggested that, instead of enhanced A β production, it is the insufficient amyloid degradation that contributes most to the deposition of amyloid plaques [71]. Another study that describes the trafficking between the brain and lymph nodes also emphasizes the importance of lymphatic clearance of A β peptides [72]. However, despite being an attractive strategy for AD drug development, there are still very limited reported candidates because of the difficulty in finding modulators with high selectivity.

Inhibition of A β aggregation: Amyloid plaques are formed by the aggregation of A β peptides. It is very difficult to establish predictive models for the dynamics of human plaque depositions

due to the inaccessibility of amyloid plaques for *in vivo* imaging. *Ex vivo* and animal studies revealed that monomeric A β is deposited into plaques in a stable and almost irreversible manner. The detailed discussion of nanoparticle-based A β aggregation inhibitors will be presented in a later part of this literature review.

As mentioned earlier, 3-APS is the only aggregation inhibitor that reached phase III trial. 3-APS is not directly interfering with the aggregation of A β ; instead, it is designed to affect the interaction between A β peptides and endogenous glycosaminoglycans. Glycosaminoglycans are polysaccharides that are capable to promote the amyloid fibrillization and deposition. Unfortunately, the result of the clinical trial was unsatisfying. Another potential amyloid inhibitor is Colostrinin, a mixed form of proline-rich polypeptides derived from colostrum. It was reported that Colostrinin could inhibit fibrillization and consequently reduce the cytotoxicity of amyloid peptides. But a phase II trial shows that the long-term therapeutic effect is not maintained [73]. Metal ions have been found associated with the fibrils formation of A β peptides. Particularly, Cu²⁺ was reported to accelerate A β fibrillization and enhance the cytotoxicity of A β [74]. Therefore, metallic chelators such as the 8-hydroxyquinoline compounds clioquinol and PBT2 have also been used to retard the fibrillization. Again, these chelators failed in clinical trials due to low efficacy.

2.4. Molecular Probes for Amyloid Detection

With the increased recognition of A β in the pathological progression of AD, the last few decades have witnessed great achievement in the development of molecular probes that are targeting different forms of A β . These probes are designed to work in many different imaging modalities including MRI, PET, SPECT, fluorescence imaging and other optical techniques. The common principle for these probes is that when interacting with A β or A β related species, detectable changes can be generated to reveal the presence and status of A β . Based on the nature

of the probes themselves, they can be classified into two categories: probes that are derived from small molecules and probes that are prepared from functionalized nanoparticles.

2.4.1 Small Molecule Based Amyloid Probes

The search of small organic amyloid probes was inspired by the observation that certain organic dyes show strong affinities toward amyloid plaques at *in vitro* studies. Small molecules also hold a higher potential to penetrate the BBB than larger molecules.

So far, nuclear imaging modalities such as PET and SPECT have achieved the most impressive success in *in vivo* amyloid detection, due to their high sensitivity and practically unlimited penetration depth. From the early 1990s, researchers started to synthesize amyloid probes from Congo red (CR), a sulfonated azo dye, and Thioflavin T (ThT), a benzothiazole dye (Figure 2.3). CR is capable to bind with amyloid in tissue sections and exhibited yellow-green birefringence under cross polarizers. On the other hand, when binding with amyloid, the fluorescence emission of ThT is enhanced and a characteristic redshift can be detected from the emission spectrum. Both of these two dyes are conventionally used for histological staining of amyloid plaques in *postmortem* studies.

Although CR was the first reported dye that exhibits amyloid affinity and therefore the first candidate for the preparation of amyloid molecule probes, the high negative charges of CR makes it very difficult to penetrate the BBB. The charge is mainly contributed by the two sulfonic groups. The relative large molecular weight and low lipophilicity also hinder the BBB penetration. A series of CR derivatives were prepared by substituting the sulfonic groups with lipophilic groups. Unfortunately, while the high amyloid affinity is generally inherited, these derivatives still fail to exhibit stratifying BBB penetration capability [75]. Nevertheless, the studies on CR derivatives enhanced our understanding of the dye-peptides interaction. It was summarized that for dyes of

CR type, the amyloid affinity is determined by the distance between the dianion charges and π - π interaction with the β -sheet of amyloid fibrils [76]. This information is very valuable for the future development of amyloid probes.

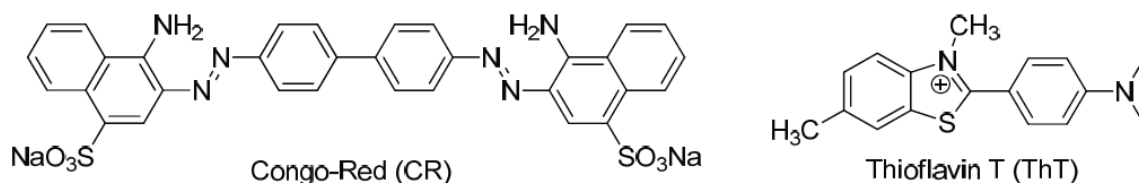


Figure 2.3 Structures of Congo Red and Thioflavin T. Adapted from reference [75]

Compared with CR, ThT is considered as a more promising scaffold for the preparation of amyloid probes due to its lower molecular weight and less charged moieties (only one positively charged nitrogen atom from the benzothiazolium group). The most successful ThT-derived probe is the Pittsburgh compound B (PiB). PiB is one of few charge-free, [^{11}C] labelled ThT derivatives prepared by Klunk et al. [77]. PiB can readily pass the BBB due to its ultra-low lipophilicity and therefore was selected to be used in human trial. Currently, [^{11}C]-PiB is one of the most well studied amyloid PET probes. However, the short half-life of [^{11}C] ($T_{1/2} = 20.4$ min) has limited the wide-spread of [^{11}C]-PiB in clinical applications. An on-site cyclotron and a radiochemistry facility are required to synthesize the [^{11}C]-PiB shortly before the injection to the patient. This also creates a problem in the training of technicians for such complicated operations. To overcome this limit, [^{18}F] isotope is also used to label the PiB analogues due to its longer half-life ($T_{1/2} = 109.7$ min). This half-life enables the supply of [^{18}F] probes from a specialized production center to many hospitals. For example, two [^{18}F] probes, GE-067 (flutemetamol, Vizamyl) and BAY94-9172 were approved for clinical trial from 2012 to 2014 [78, 79]. However, as conventional [^{18}F] labelling is achieved by the addition of short fluoro-alkyl chains, the lipophilicity of these chains may lead to higher non-specific binding. In addition, the direct attachment of fluoro-alkyl chains may also be

detrimental to the resulting compound's amyloid affinity [80]. Kung et al. developed an alternative strategy for [^{18}F] labelling, instead of directly adding [^{18}F] atoms to the ThT scaffold, a short PEG chain is conjugated first, and the [^{18}F] atoms are doped at the end of the PEG chains. This kind of fluoro-PEG makes it possible to manipulate the lipophilicity of probes and at the same time maintain the affinity towards amyloid. On the other hand, the introduction of PEG chains reduces the BBB penetration due to increased molecular weight and polarity [81].

Although radionuclear probes have been attracting most interests in the development of amyloid probes in the last two decades, the high cost of instrumentation, limited availability of radioisotopes and the concern of radiation exposure make it very difficult to apply nuclear imaging techniques in routine health check procedures. Optical probes, therefore, are receiving increasing attentions due to their inexpensive, non-radiative and highly sensitive features. In particular, optical probes that can generate signals in the near infrared ranges (NIR, 650-900 nm) are of special interest for bioimaging applications. As shown in Figure 2.4, light that falls into the NIR ranges has the lowest absorption in tissue and therefore could achieve deeper penetration [82]. This range is also known as the NIR optical window for *in vivo* imaging.

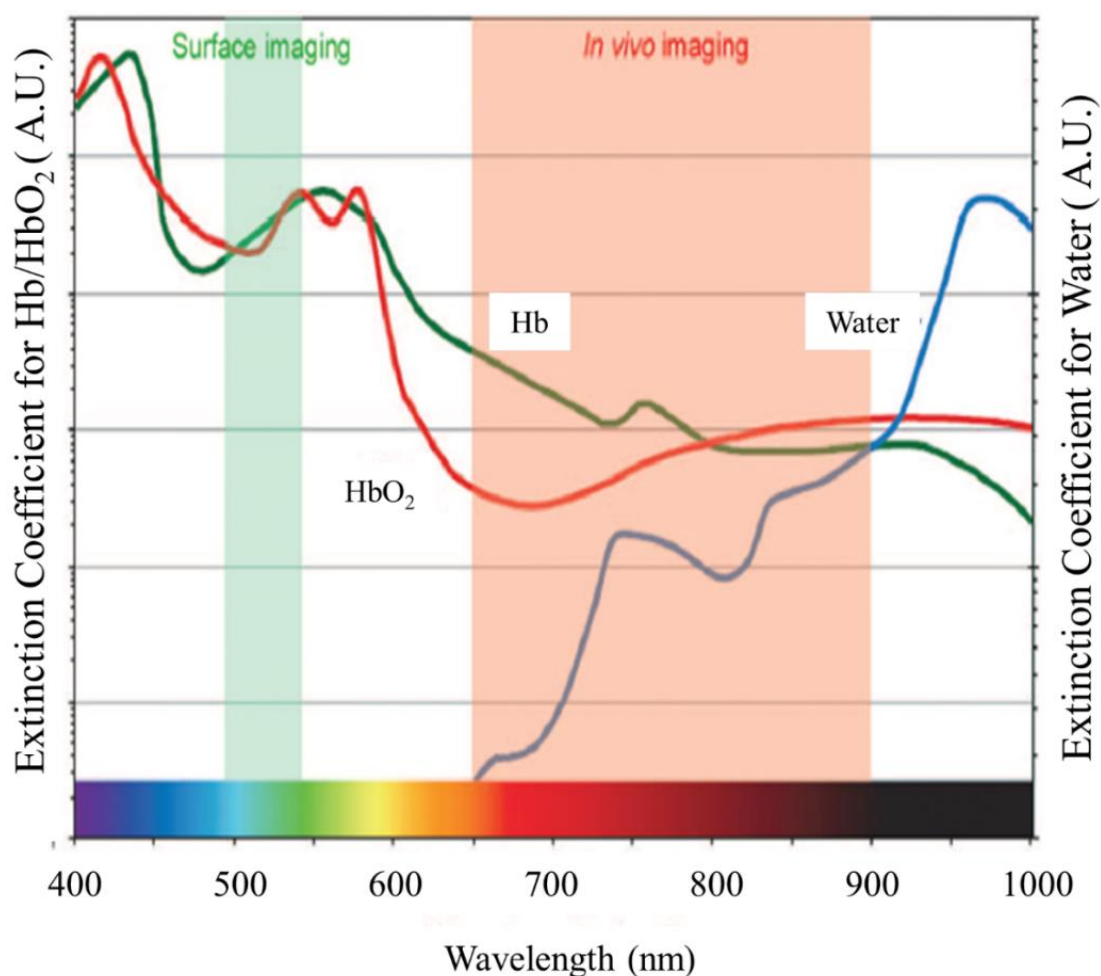


Figure 2.4 The position of NIR optical window in the spectrum. Extinction coefficient values of water and oxy- and deoxyhemoglobin (Hb/HbO₂) are plotted ranging from visible to near-infrared wavelength. Adapted from reference [82].

The general guidelines to select a fluorescent amyloid probe are listed below:

- High affinity and selectivity toward amyloid.
- High quantum yield and detectable changes when interacting with amyloid.
- Suitable emission wavelength, preferably between 650 nm and 900 nm to achieve deeper penetration.
- Capable to penetrate BBB and fast washout from normal brain region.
- High metabolic stability and biocompatibility.

f) Facile and robust synthesis.

As mentioned before, ThT shows a fluorescence enhancement when bound to amyloid fibrils. Naturally, it has become the most widely studied fluorescent amyloid probe both *in vitro* and *in vivo*. This fluorescence enhancement is attributed to the restriction of molecular movements. As shown in Figure 2.3, ThT consists of a benzothiazole ring (acceptor) and a benzylamine ring (donor). At free state, the two components can rotate freely around the shared C-C bond. When incident light photons excite the ThT molecules, the majority of the excitation energy will be released through this free rotation, leading to a relatively low fluorescence emission. However, when bound with the β -sheet of amyloid fibrils, the free rotations of ThT molecules are restricted. Consequently, the excitation energy can only be released as emitted photons, causing an enhanced quantum yield [83]. Although ThT is considered as the ‘gold standard’ for *in vitro* identification of amyloid fibrils, its polarity and short-wavelength emission have hindered its application for *in vivo* imaging. ThT analogs with longer-wavelength emission and higher BBB penetration have also been synthesized. The mechanism of ThT-amyloid interaction provides a model to explain dye-amyloid interaction. Most reported amyloid fluorescent probes shared a common structure similar to that of ThT. They are composed by electron donor and acceptor moieties that are linked by a highly polarizable bond. When bound to amyloid, their fluorescence is enhanced due to the hindrance of molecular motion. Apart from ThT, other widely studied scaffolds include stilbene, curcumin, thiophenes and Boron-dipyrromethene (BODIPY). Figure 2.5 shows some of the derivatives used for amyloid imaging. A typical moieties-linked-by-bridge structure can be found in all of the derivatives.

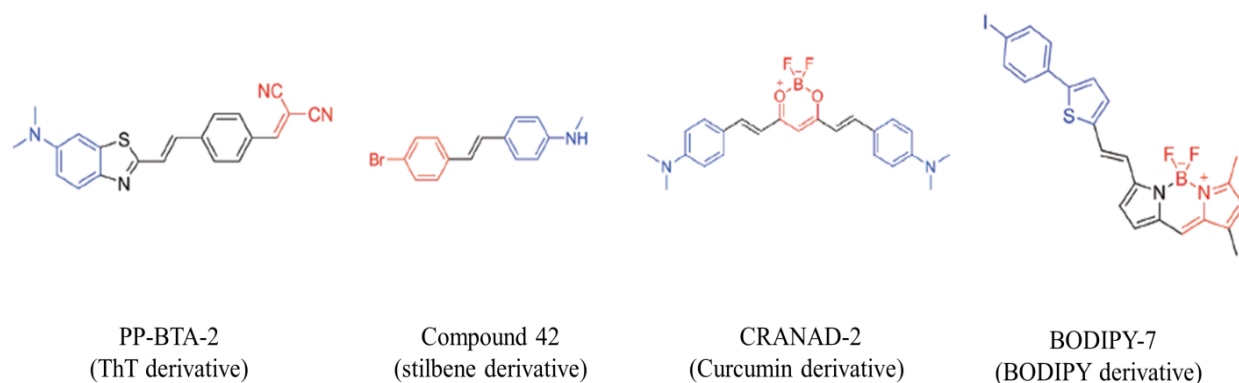


Figure 2.5 Examples of fluorescent amyloid probes. Notice that all of them show a moiety-linked-by-bridge structure. Adapted from reference [7].

2.4.2 Nanoparticle Based Amyloid Probes

Nanoparticle based imaging probes (nanoprobes) have long been used in oncology studies. The success of nanoprobes can be attributed to several comparative advantages over small molecule probes. Some nanoparticles themselves can function as contrast agents. For example, quantum dots (QD) are considered as potential alternatives for organic dyes due to their higher photostability, wide absorption, tunable emission, high quantum yield, large Stokes shift and long fluorescence lifetime [84]. Iron oxide nanoparticles (IONPs) are widely employed as T_2 MRI contrast agents and they are generally less toxic than the gadolinium-based contrast agents [85]. The heavy atomic weight of gold element makes gold nanoparticles (AuNPs) an ideal contrast agent for X-ray CT. The strong electromagnetic enhancement of AuNPs can also be utilized in SERS based imaging and detection [86].

Apart from acting as contrast agents, the large surface area of nanoparticles makes them a versatile platform for probe development. Targeting ligands and contrast agents can be conjugated together with a single nanoparticle to achieve a more precise diagnosis. Since most of the targeting ligands and contrast agents are much smaller than nanoparticles, one nanoparticle can

accommodate multiple moieties. This ‘multivalence’ nature of nanoprobe makes them capable to generate stronger signals and better targeting efficiency [87].

Another important factor that contributes to the wide application of nanoprobe, particularly in tumor diagnosis, is the enhanced permeability and retention (EPR) effect: The leaky neovasculature and low-effective lymphatic drainage of tumor tissue causing a passive accumulation of nanoparticles in the tumor tissues [88]. However, EPR effect is not applicable for amyloid diagnosis. In addition, the large size of nanoprobe makes it very difficult to deliver them into the brain. Therefore, amyloid-targeting nanoprobe didn’t achieve the same level of success as tumor-targeting nanoprobe. During the past years, several methods have been developed to facilitate the delivery of nanoparticles across the BBB. The major component of the BBB is endothelial cells and the passage between these endothelial cells can be open by certain receptor-related proteins and peptides. Nanoprobe can be conjugated with these ligands to enhance their BBB permeability. Nanoprobe can also be encapsulated by polymers such as PEG and PLGA in order to penetrate the BBB [89]. Liu et al. reported the synthesis of B6 peptide (a transferrin substitute) conjugated PEG-PLA nanoparticles (PEG-PLA-NP) for enhanced brain delivery [90]. The PEG-PLA-NP was loaded with the neuroprotective peptide NAPVSIPQ (NAP) and was used as a drug-delivery vehicle. Animal studies using a mouse model show a clearly enhanced brain accumulation of the B6 functionalized nanoparticles (Figure 2.6). By delivering such a large nanoparticle (120 nm diameter) to the mouse brain, this work demonstrates the impressive BBB-penetrating capability induced by polymer encapsulation.

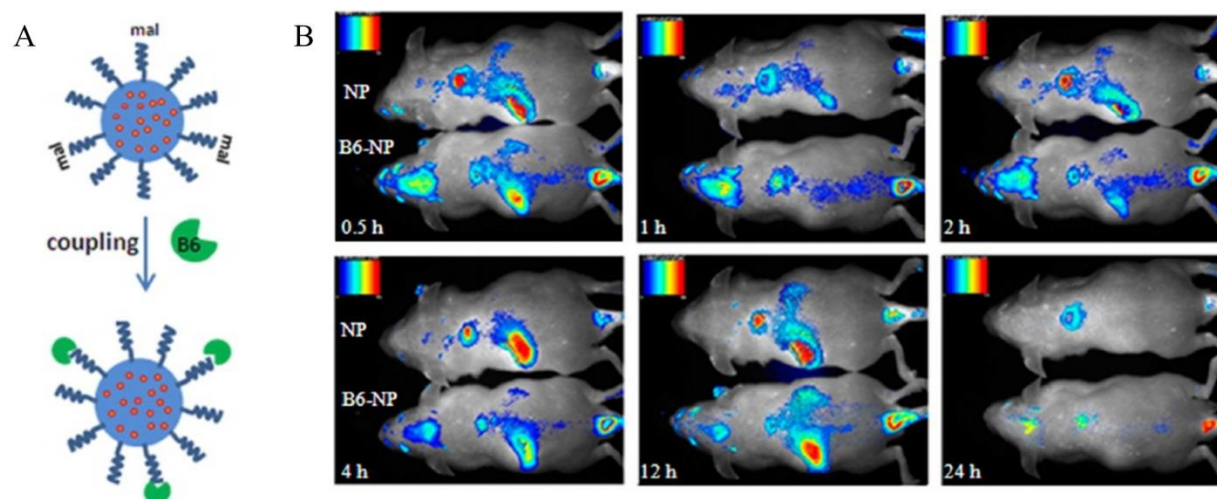


Figure 2.6 B6-conjugated PEG-PLA NP for Enhanced Brain Delivery. (a) The structure of B6-conjugated and unconjugated PEG-PLA-NP. (b) Distribution and retention of B6-PEG-PLA or PEG-PLA NP in nude mice following tail vein intravenous administration. Adapted from reference [90].

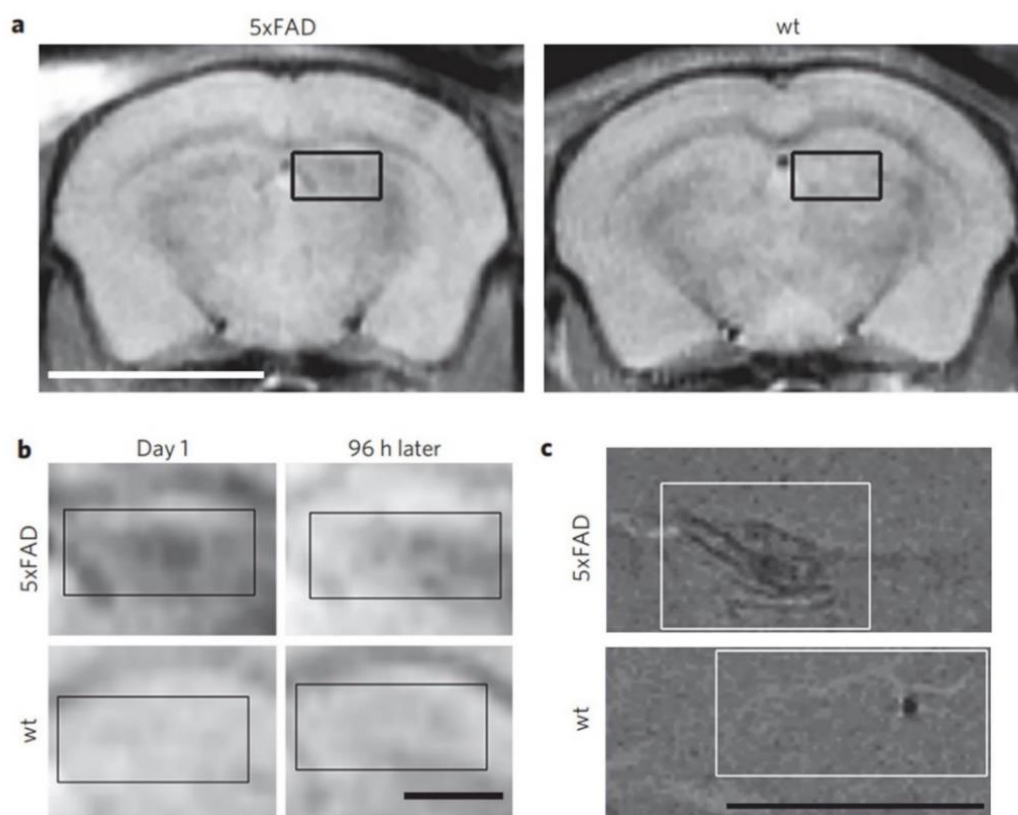


Figure 2.7 NU4MNs labelled Tg mouse brain slices. (a) *In vivo* imaging of probe distribution in live mice 4 h after intranasal inoculation. (b) Higher magnification images of the hippocampal region of the 5xFAD and wild-type mice show probe distribution 4 h after inoculation and the changes in distribution 96 h later. (c) Sagittal sections from 5xFAD and wild-type eight-month-old mice were probed with NU4MNS and layered in agarose for MRI. Adapted from reference [91].

The increased understanding of the BBB passage mechanism and the successful development of transfer ligands have put nanoprobes back to the arena of fighting against neurodegenerative diseases such as AD. Apart from polymeric nanoparticles, IONPs and QDs have also been used for amyloid imaging. These nanoprobes are all conjugated with different types of conjugate amyloid-targeting ligands (including anti-A β monoclonal antibodies [91-93], peptides with affinity to A β [94] and curcumin derivatives [95]). Viola et al. reported an amyloid-targeting MR probe, prepared by conjugating anti-A β antibody (monoclonal antibody NU4) with nitro-dopamine (nDOPA) and PEG stabilized 12–16 nm magnetic nanoparticles (MNs) [91]. Functionalized NU4MNs were injected into transgenic mice (Tg 5xFAD) that are capable to produce human amyloid. *In vivo* MR imaging shows a detectable difference between the transgenic mice brain and wild type (wt) mice brain (Figure 2.7).

While great efforts have been invested to help deliver nanoparticles to the brain, an alternative approach was proposed to bypass the BBB challenge. That is, instead of imaging brain amyloid, nanoprobes can be utilized to target peripheral amyloid that is related to AD. Particularly, skin amyloid has been found related to the pathogenesis of AD. As shown in Figure 2.8, Clos et al. have summarized the connections between the brain and skin amyloid [96]. Neural and epidermal tissues are both ectodermal derivatives that are developed from a common embryological origin. Therefore, it is reasonable to deduce that protein misfolding and aggregation are taking place in a similar mechanism. Cutaneous amyloid could spread to other organs including the brain or vice

versa. The coincidence between dermal manifestations and several neuronal diseases further proves the brain-skin connection [97]. In addition, oral and ophthalmic amyloids have also been detected in AD patients [98, 99]. Considering the accessibility of peripheral tissue, detection of peripheral AD biomarkers is expected to become an important supplementary diagnosis method. This type of peripheral AD biomarkers is particularly desired for the screening of high-AD-risk populations, which would require a low-cost and facile diagnostic approach. For such applications, the usage of nanoprobe is highly promising. A series of amyloid sensing probes has been reported using different kinds of nanoparticles. Most of them are based on optical phenomena such as fluorescence resonance energy transfer (FRET) and Raman spectroscopy.

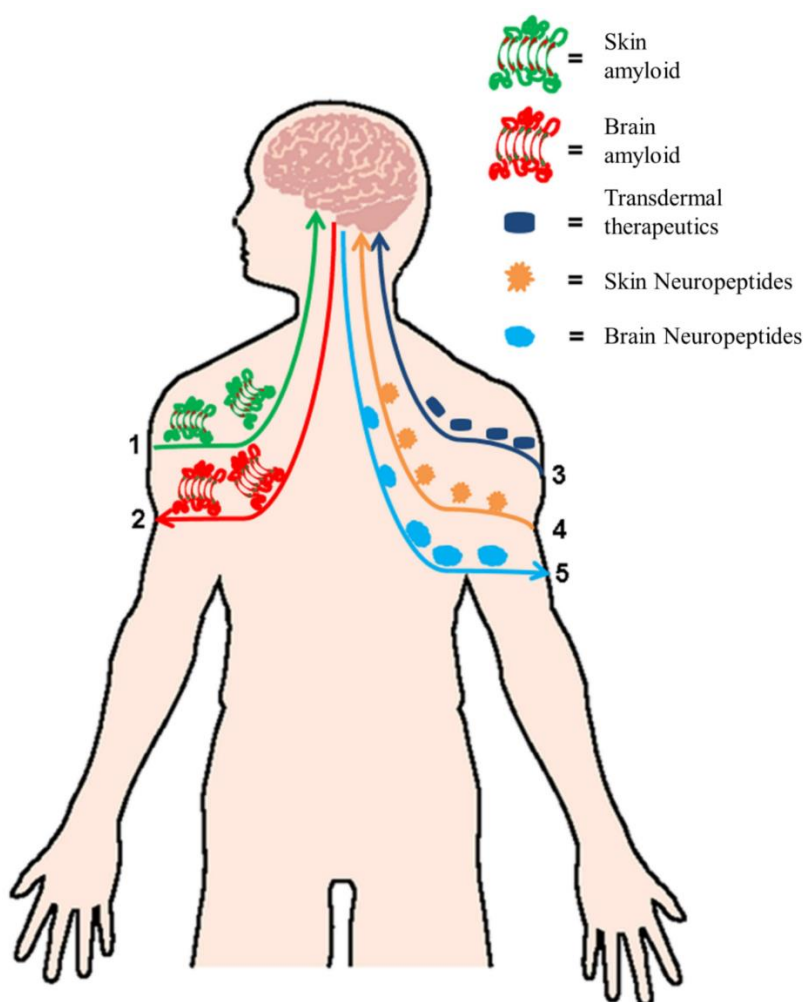


Figure 2.8 Links between brain and skin amyloid. Adapted from reference [96].

Recently, a SERS sensor that can detect soluble amyloid oligomers has been reported by Guerrini et al. [100]. The SERS sensor is prepared by conjugating 4-mercaptopbenzoic acid (MBA) with polystyrene stabilized gold nanoparticles. The thiol groups of MBA forms covalent bonds with AuNPs. And the carboxylic groups on the other end of MBA were used to chelate Al^{3+} ions (Figure 2.9a). The AuNP substrate generates the SERS effect and the chelated Al^{3+} ions provide the adsorption sites for amyloid oligomers. When exposed to soluble oligomers, the Al^{3+} ions promote a sort of “freezing” of the peptide structure in its oligomeric state [101]. At the same time, the adsorbed oligomers also induce a mechanical deformation on the MBA molecules, causing detectable changes in the SERS spectrum (Figure 2.9b). The magnitude of spectral changes can also be quantitatively correlated with the concentrations of amyloid oligomers (Figure 2.9c).

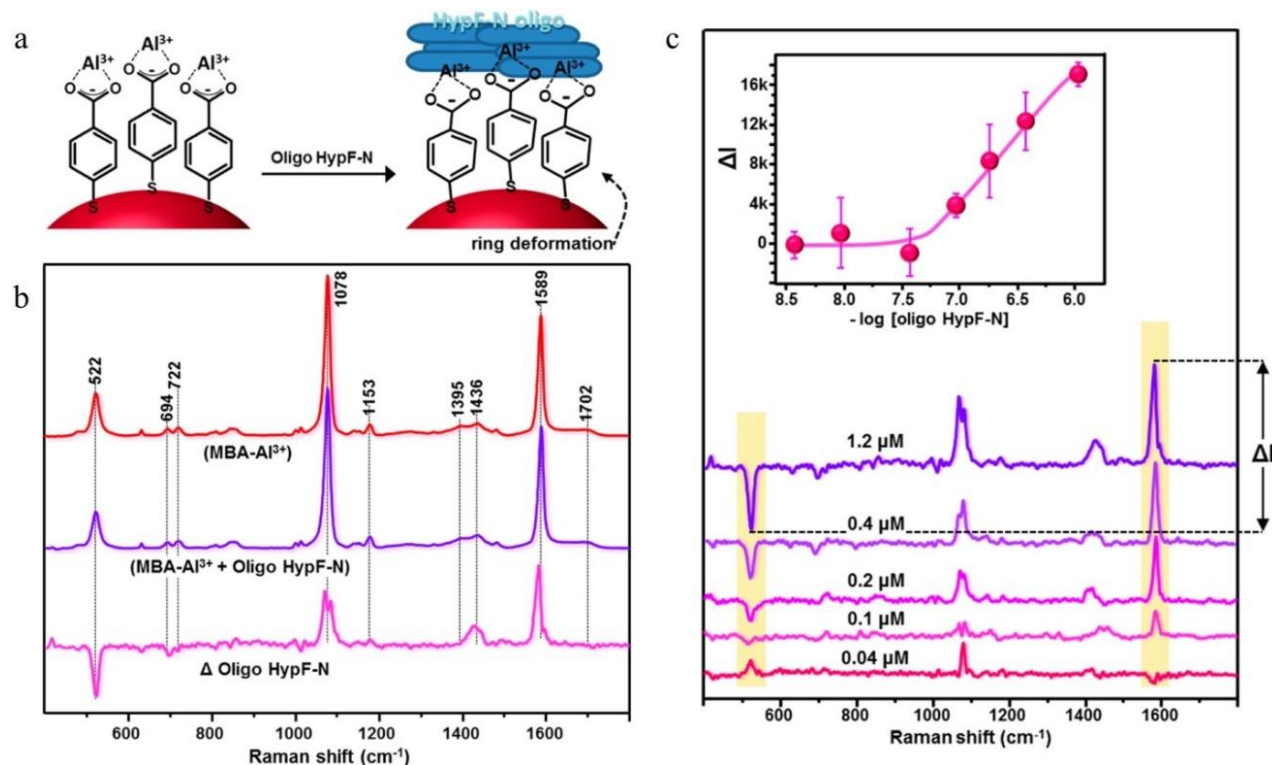


Figure 2.9 AuNP-based SERS sensor for amyloid oligomers (HypF-N). (a). Interaction between amyloid oligomers and AuNP. (b) Changes in SERS spectrum upon binding with amyloid

oligomers. (c) The relationship between the magnitudes of spectral changes and the concentrations of amyloid oligomers. Adapted from reference [100].

2.5. Multifunctional Nanoprobes

So far, a variety of amyloid-targeting molecular probes has been reported and these probes are designed to function in different diagnostic modalities. However, no single modality can provide all the required pathological information due to their inherent limitations. Table 2.1. summarizes the advantages and disadvantages of commonly used molecular imaging techniques. The idea of combining two or more complementary modalities together to obtain synergic effect is widely accepted in the research community [85]. By combining these two modalities, high resolution and excellent sensitivity can be obtained simultaneously. While great efforts have been made in designing hybrid molecular imaging instruments (e.g. PET/CT and PET/MRI system [30]), the requirement of a single probe with multiple signaling capacities has arisen. Compared to individual monomodal contrast agents, a multimodal probe provides better image registration, consistent pharmacokinetics and reduced administration load for the patient. Due to their large surface area and high feasibility for ligands attachment, nanoparticles are widely accepted as the best candidates to prepare multimodal probes. Considering that these nanoprobes can be used not only in different imaging modalities but also in various sensing techniques, the term “multifunctional nanoprobes (MFNPs)”, instead of “multimodal nanoprobes”, is used in this thesis.

Imaging Technique	Contrast Mechanism	Advantages	Disadvantages	Contrast Agent
Fluorescence Imaging [102, 103]	Photon emission	<ul style="list-style-type: none"> •Highly sensitive •High temporal resolution •Non-ionizing 	<ul style="list-style-type: none"> •Low penetration •Relatively low spatial resolution 	<ul style="list-style-type: none"> •Luciferin •Fluorescent dye •Quantum Dots

		<ul style="list-style-type: none"> •Low cost 	<ul style="list-style-type: none"> •Less chances for clinics 	<ul style="list-style-type: none"> •Carbon nanoparticles •Lanthanide particles
MRI [104, 105]	Proton density and relaxation time	<ul style="list-style-type: none"> •Unlimited penetration •High spatial resolution •Non-ionizing •Capable to image soft tissue •Fully translational 	<ul style="list-style-type: none"> •Low sensitivity •Long image acquisition time •High cost 	<ul style="list-style-type: none"> •Gadolinium •Iron Oxide •Manganese
PET [106, 107]	γ -ray emission	<ul style="list-style-type: none"> •Unlimited penetration •Highly sensitive •Capable for quantitative imaging •Fully translational 	<ul style="list-style-type: none"> •Low spatial resolution •Radiation exposure •Cyclotron is needed to produce isotopes •High cost 	<ul style="list-style-type: none"> •Non-metal Isotope: ^{18}F, ^{11}C •Metal Isotope: ^{64}Cu, ^{86}Y, ^{68}Ga
SPECT [108]	γ -ray emission	<ul style="list-style-type: none"> •Unlimited penetration •Can be combined with radiotherapy •Less expensive than PET •Fully translational 	<ul style="list-style-type: none"> •Radiation exposure •Low spatial resolution 	<ul style="list-style-type: none"> •Isotope: $^{99\text{m}}\text{Tc}$, ^{123}I, ^{111}In, ^{177}Lu
CT [109]	X-ray attenuation	<ul style="list-style-type: none"> •Unlimited penetration •High spatial resolution •Anatomical imaging •Fully translational 	<ul style="list-style-type: none"> •Limited molecular imaging application •Radiation exposure 	<ul style="list-style-type: none"> •Iodine •Barium •Gold particles

Photoacoustic Tomography [110]	Photon absorption	<ul style="list-style-type: none"> •Deeper penetration compare to optical imaging •Scalable imaging •Non-ionizing 	<ul style="list-style-type: none"> •Deeper penetration and higher resolution cannot be obtained simultaneously 	<ul style="list-style-type: none"> •Organic dye •Gold nanoparticles •Carbon Nanotube
Optical Coherence Tomography [111]	Light reflection	<ul style="list-style-type: none"> •High spatial resolution •Able to extract phase information •Non-ionizing 	<ul style="list-style-type: none"> •Limited tissue penetration 	<ul style="list-style-type: none"> •Gold nanoparticles •Microsphere •Magnetic particles (Magnetomotive OCT)
Ultrasound Imaging [112]	Acoustic echo	<ul style="list-style-type: none"> •Real-time imaging •Able to detect cyst and blood flow •Non-ionizing •Low cost 	<ul style="list-style-type: none"> •Imaging quality is operator-dependent •Limited contrast agent application 	<ul style="list-style-type: none"> •Gas-filled microbubble •Liposomes •Perfluorocarbon droplets

Table 2.1 Advantages and disadvantages of commonly used molecular imaging modalities.

2.5.1. Design Principles for Multifunctional Nanoprobes

While some of the MFNPs used for molecular imaging have been produced as a by-product or by ‘happy coincidence’ from researches aiming at non-imaging application, most of the reported MFNPs are carefully designed to meet a certain requirement. The following four factors need to be considered during the design of MFNPs.

Modalities to be integrated: The modalities that the MFNP can be used for should be complementary to each other. The aforementioned MRI/Optical integration is one of the most widely studied combinations in MFNPs. Other combinations, including MRI/PET, Optical/PET and Optical/CT, have also been extensively explored. Moreover, MFNPs with triple or more signal-reporting capabilities have been synthesized with carefully designed protocols [113-116].

A major challenge in the design of MFNPs is to balance the sensitivities between different modalities, which may vary up to three orders of magnitude [117]. Luckily, the large surface area of NPs can serve to overcome this problem by controlling the moiety ratio between two contrast agents. It is also important that the integration of multiple agents should not produce detrimental effects to the performance factor of each agent. Different imaging modalities rely on different properties to generate the contrast and hence their performances are evaluated accordingly. For example, MRI contrast agents enhance the contrast by accelerating the relaxation processes of neighboring water protons. There are two types of relaxation process: longitudinal relaxation (T_1) and transverse relaxation (T_2). Contrast agents may affect the relaxation processes and hence MRI agents can be classified into T_1 and T_2 agents. The ability of one agent to affect the relaxation process is defined as r_1 or r_2 relaxivity, corresponding to the two types of relaxations [118]. For optical imaging, the quantum yield and excitation/emission wavelength are very important for the imaging resolution, signal-to-noise ratio and penetration depth [84]. An MRI/Optical bi-modal probe synthesized by integrating an MRI agent and an optical agent should exhibit similar relaxivity and optical properties compared to the stand-alone contrast agent.

Configurations of MFNP. We classify the configuration of MFNPs into the following four categories: conjugation, encapsulation, core/shell and co-doping (Figure 2.10). MFNPs with conjugation or core/shell configuration are normally synthesized through a multi-step reaction that could be more time consuming and complicated. Co-doped MFNPs can be prepared by facile one-step routes and are generally smaller in size. For different MFNPs, a certain configuration may provide the best integration. Appropriate configuration can also help to reduce the interference between contrast agents. However, the actual configuration of MFNPs may be a mixture of two or

more types. An MFNP that has been prepared through encapsulation can be further conjugated with targeting ligands, and a core/shell nanoparticle may also be doped to yield more functions.

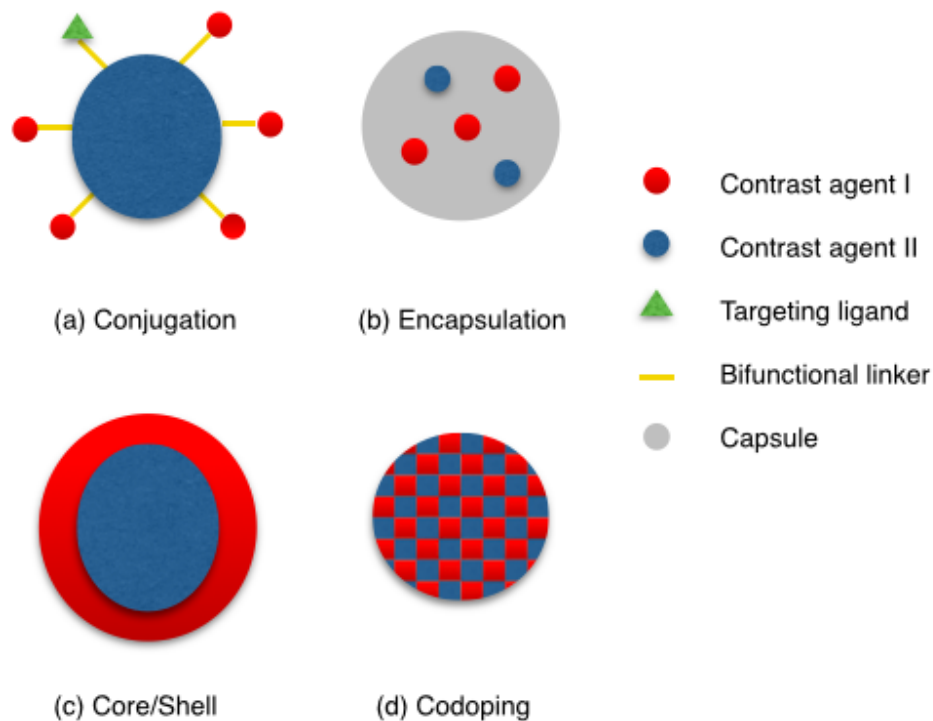


Figure 2.10 Four MFNPs configurations. (a) Conjugation: two imaging moieties are conjugated by a bifunctional chemical linker. (b) Encapsulation: a matrix structure (i.e. micelle or silica particle) is used to entrap nanoparticles. (c) Core/Shell: an outer shell that possesses different function compare to the core particles. (d) Co-doping: different agents are doped into one host particle, the host particle can also act as one imaging agent.

Size: The size of MFNPs plays a major role in determining their bio-distribution, clearance, contrast enhancement and the cells that can be targeted. Small nanoparticles (<5.5 nm) will be quickly cleared out through the renal system, whereas larger nanoparticles are mainly captured by the reticuloendothelial system, resulting in a much longer circulation time and liver accumulation [119]. However, if the nanoparticles are too large, the chance of RES take-up will increase, leading

to a shorter half-life. Longer half-life is generally desired since it gives MFNPs enough time to extravasate out of the vasculature. The size also affects the targeting efficacy of MFNPs. For instance, large NPs (>100 nm) are quickly cleared from plasma to the spleen, liver and bone marrow. Hence those NPs should be designed to target those organs. On the other hand, smaller NPs (<30 nm) should be designed to target tumor tissue, due to their long circulation time and EPR effect [117, 120]. For quantum-dots based MFNPs, the wavelength of fluorescent emission is also affected by its size, which gives the QD based MFNPs an advantage of tunable emission through size control [84]. For Gd^{3+} doped MFNPs, the size of NPs determines the number of surface Gd^{3+} and consequently affects the NPs' relaxivity [121].

Surface treatment: Surface treatment is very important to control the MFNPs' circulation time, biocompatibility and targeting efficiency. Many NPs are coated with hydrophobic molecules. For bioimaging application, those NPs need to be dispersed in an aqueous solution by hydrophilic capping agent. The capping can also provide surface functional groups to conjugate with other functional moieties [122]. One widely used capping material is PEG and its derivatives. A surface PEG layer can shield the nanoparticles from the reticuloendothelial system by minimizing plasma protein binding, and this kind of capped nanoparticles are often referred to as stealth particles. PEGylation is widely used to increase the circulation time of nanoparticles [123-125]. PEGylation has also been used to enhance tumor targeting of nanoparticles due to the high affinity between cancer cells and PEG capping [126, 127]. Other capping agents that behave similarly have also been exploited, including polyacrylic acid [128, 129], polyethyleneimine [130], and polyhedral oligomeric silsesquioxanes [131]. To further enhance the specific targeting and internalization of nanoprobe, bio-recognition ligands, such as antibodies, peptides, and aptamers are often conjugated to the MFNPs surface [132]. Due to different surface treatments, MFNPs with the same

core size may have many different hydrodynamic diameters, which may result in different circulation and clearance behavior.

2.5.2. Nanoparticles for the Preparation of MFNPs

This sub-chapter summarizes some of the well-studied nanoparticles that have been used to prepare MFNP. Although most of these MFNPs are used for oncology studies, their preparation methods provide us with a valuable experience for the synthesis of amyloid-targeting MFNPs.

Quantum Dots. QDs are nano-sized semiconductor crystals. Most reported QDs are synthesized with hydrophobic capping molecules; additional encapsulation by amphiphilic surfactant or ligand exchange is required before applying the QD as molecular probes. Normally, encapsulation will produce much larger QDs as compared to QDs undergoing ligand exchange [133]. The second contrast agent can be doped during QD preparation, incorporated during the encapsulation process or conjugated to the surface of those hydrophilic QDs.

Iron Oxide Nanoparticles. IONPs are being widely employed as T₂ MRI contrast agent. For biomedical applications, IONPs need to be water dispersible and biocompatible; this is normally achieved by coating with hydrophilic organic molecules such as PEG or dextran [134]. Further surface modification enables IONPs to be conjugated with another contrast agent and become multifunctional. Core/Shell configurations are also popular in which IONPs are functionalized with an organic or inorganic shell [135].

Carbon dots. Carbon dots (C-dots) are quantum sized (<10 nm) photoluminescent (PL) carbon particles. Due to their excellent biocompatibility, abundant nature and potential for large-scale green synthesis, they have received significant attention in the bioimaging community as alternatives to heavy-metal-containing QDs [136, 137]. The synthetic methods of C-dots are generally categorized into two types: top-down approach, including arc discharge, laser ablation,

and electrochemical oxidation, where C-dots are “peeled off” from a bulk carbon source; and bottom-up approach, including thermal/acidic oxidation, hydrothermal reaction, and microwave/ultrasonic methods. A clear understanding of their luminescent origin is still missing. However, it is believed that the PL property is strongly related to the surface passivation/oxidation. Sun et al. argued that surface energy traps cause the luminescence. Those energy traps are stabilized by quantum confinement effect and become emissive after surface passivation [138]. This hypothesis is supported by the fact that many reported C-dots require a passivation layer to exhibit PL. However, some C-dots produced from bottom-up methods can exhibit PL properties without any additional passivation agent [139, 140]. It may be argued that since these reported passivation-free C-dots can only exhibit PL in the presence of solvents, the solvent molecules are actually acting as the passivation agents [141]. Some researchers attribute the luminescence to the surface carboxylate group [142, 143]. Since most of the as-synthesized C-dots are made of particles with different size, the emission spectra of C-dots are wideband, characterized by an emission peak in short wavelength and a long “tail” extending into longer wavelength regions. Further separation of C-dots can narrow down the emission spectra and can also increase the quantum yields [144, 145]. On the other hand, the wide emission spectra can be exploited for multi-color imaging. The emission spectra of C-dots are also excitation dependent, and the peak position has a red-shift when excited with longer-wavelength light. One drawback for C-dots as *in vivo* imaging probes is that the emission peaks of currently reported C-dots are limited to the ultraviolet-visible (UV-Vis) region, which will be strongly scattered by biological tissue. Some C-dots exhibit detectable emission at the VIS-IR region and might be suitable for *in vivo* imaging.

Gold Nanoparticles. Nano-scaled (1-100 nm) gold particles (AuNPs) possess many distinct properties compared to bulk gold. Particularly, for bio-imaging applications, the following features

are most important: the absorbance and fluorescence of gold nanostructures are significantly enhanced with respect to bulk gold, and just like QDs, the absorption and emission wavelength can be tuned by manipulating the size and morphology of the nanoparticles [146]. The absorption of AuNPs decreases as the 3rd power of diameter, whereas scattering decreases as the 6th power of diameter. This means that below a certain size, absorption will be the predominant event. Therefore, small Au-NPs are often used for photothermal imaging while larger AuNPs are more suitable for photoacoustic imaging [147]. The laser-induced heat effect is also often used for photothermal therapy. The first scientifically reported synthesis of colloidal gold particles can be traced back to the year of 1857, when Michael Faraday obtained a “ruby fluid” by stabilizing reduced gold chloride with carbon-disulfide [148]. Today, a similar principle is still followed in many nanoparticle preparation methods: gold salts are reduced with the addition of capping agents. The capping agents prevent aggregation of particles and therefore the particles sizes are restricted in the nano range. With the development of nano-synthesis technology, controlled synthesis of AuNPs with various shapes and sizes are possible [149, 150]. For bioimaging applications this means that researchers can choose the optimal Au-NPs which suit the imaging targets.

Before using AuNPs in bio-imaging applications, one essential step is to functionalize the particles' surface. Many capping agents used in the synthesis of AuNPs are not biocompatible. For example, Cetrimonium bromide (CTAB), which is often used for morphology control during the Au-NPs synthesis, is found to be toxic [151]. A variety of functionalization methods, including ligand exchange, PEGylation, silica/polymer coating and biomolecule capping, has been developed in order to enhance the biocompatibility of AuNPs [152]. Additionally, the functionalized Au-NPs can be further conjugated with other imaging probes or therapeutic agents.

2.5.3. Targeting Ligands for MFNPs

Targeting ligands are used to differentiate pathological cells and tissues from healthy ones. Generally, targeting ligands are designed to bind to receptors that are over-expressed in pathological cells or tissues. Through receptor-mediated endocytosis, these additional targeting ligands can enhance the specific cell binding and internalization. Without the targeting ligand NP internalization is mainly determined by non-specific interactions with the cell membrane, which can be relatively slower, especially when the NPs are shielded with a PEG layer. In terms of particle morphology, targeting ligands are normally presented at the outer surface, on top of the capping layer, to achieve maximum receptor binding. According to their molecular constitution, targeting ligands can be classified into five groups: Full antibody, antibody fragment, peptide, aptamer and small molecules. Each group has its own advantages and limitations on targeting efficacy, stability, and ease of preparation [153]. Significant effort has been put on monoclonal antibodies as targeting ligands, and several successful therapies have been reported based on engineered antibodies [154]. Despite those successes, the large molecule size, complex modification process and high batch-to-batch variation of monoclonal antibodies have driven researchers to search for alternative ligands. Full-sized antibodies can be decomposed into different fragments using proteolytic digestion. Some of those fragments retain the receptor binding capability. Compared to the full antibody, antibody fragments are smaller and easier to manipulate. Peptides are another attractive candidates for targeting ligands. Thanks to the development of different peptide libraries and screening technologies, a variety of peptides has been discovered to have high affinities with certain receptors [155]. Other than proteomic ligands, small nucleic acid ligands, referred as aptamers, have also been attracting much interest. Aptamers can bind to a wide range of receptors with an affinity comparable to antibodies. More excitingly,

aptamers can be synthesized with large scale and high batch-to-batch consistency, using an *in vitro* chemical technique known as systematic evolution of ligands by exponential enrichment [156]. Some small molecules have also been found to have targeting capability. One of the promising tumor targeting ligands is folic acid, which is targeting over-expressed folate receptors in cancer cells [157]. The quantity of targeting ligands affects the targeting efficacy. Generally, more targeting ligands lead to a better targeting effect. Nanoparticles which are conjugated with multiple ligands normally possess enhanced affinity, slower disassociation, and better biodistribution, compared to stand-alone targeting ligands. However, for PEGylated nanoparticles, too many surface ligands may be detrimental to the stealth capability. Studies have shown that high density of surface ligands leads to shorter circulation and lower tumor localization compared to nanoparticles conjugated with fewer ligands [158]. In addition, the morphology of the PEG chains also affects the targeting and stealth capability. At moderate concentration, the lateral pressure between PEG chains forces them to extend into a brush conformation. If the PEG density is too high, the PEG chain will tangle itself, forming a random-coil conformation, also known as the mushroom conformation. Brush PEG layer provides better stealth effect than mushroom PEG chains due to its greater protein repulsion. Targeting ligands that are grafted on the extended PEG chains have more chance to interact with receptors [159]. To achieve an optimal combination of specific targeting and stealth effect, the concentrations of targeting and stealth agents should be carefully balanced.

2.6. Amyloid Aggregation Inhibitors

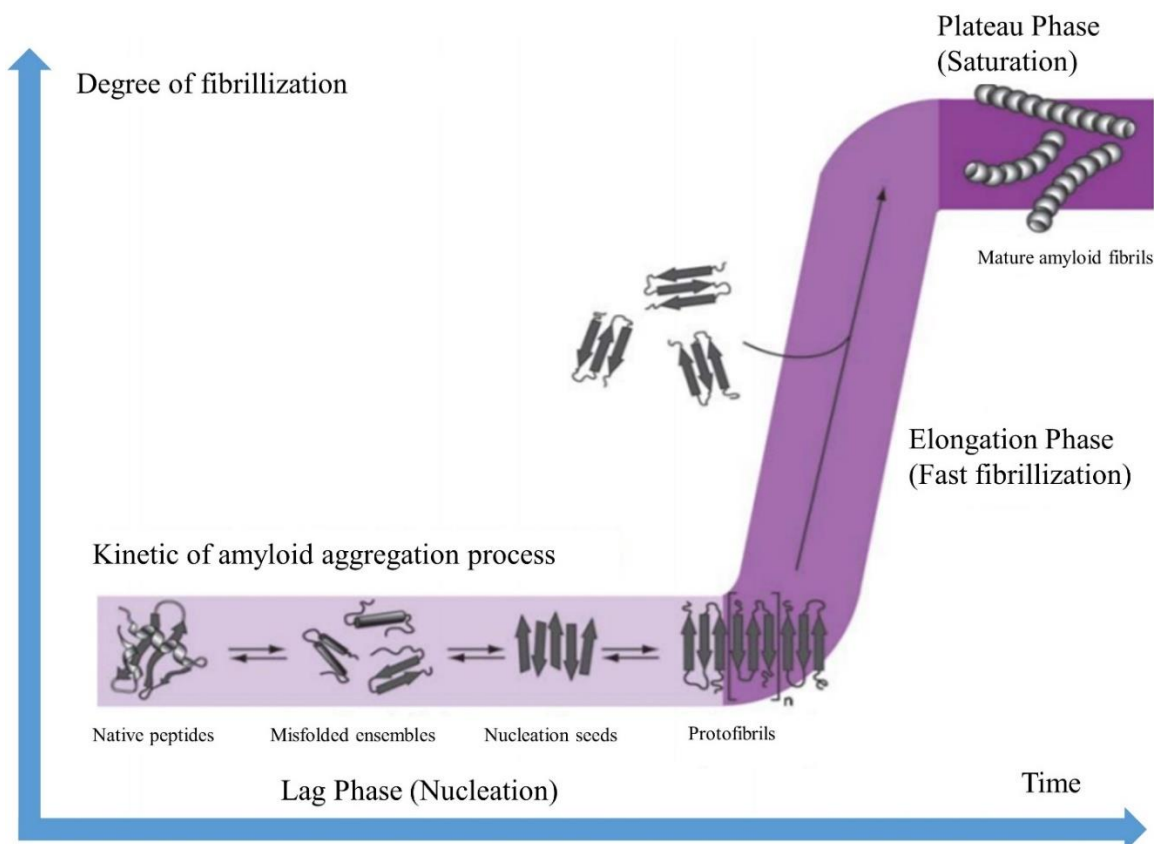


Figure 2.11 Schematic representation of the amyloid aggregation process. In the lag phase, A β monomers combine into soluble oligomers. These oligomers act as nucleation seeds that sequester other A β monomers and oligomers, leading to a fast fibrils growth. The growth stops when the fibril content reaches the maximum, represented as the plateau phase. Adapted from reference [160].

Kinetically, the aggregation process of amyloid can be divided into three phases:

1. Initial lag phase: A β monomers aggregated into small clusters that later act as growth seed.
2. Growth phase: A β seeds absorb free monomers and fast elongate.
3. Plateau phase: the mature fibrils formed.

The overall aggregation process is often illustrated as a sigmoidal curve (Figure 2.11). The lag phase is generally considered as the rate-limiting step. Environmental conditions, such as metal ions, pH, temperature, can affect the aggregation process. Extrinsic inhibitors can also modulate this process by altering intermolecular interactions.

Just like amyloid probes, the search for amyloid aggregation inhibitors is also taking place among both small molecules and nanoparticles. In addition, peptides and protein-based inhibitors have also been extensively investigated. Due to the complexity and wide variety of transient intermediates and oligomers, it is often difficult to conclude a generalized working mechanism for these inhibitors. In addition, the lack of a defined structure of amyloid aggregates also makes it difficult to synthesize an inhibitor from structure-based design. Instead, the screening of potential amyloid inhibitors is generally conducted by trial-and-error experiments. The inhibition efficacy is normally evaluated by dye-binding assays such as ThT assays and high-resolution microscopy such as transmission electron microscopy (TEM) and atomic force microscopy (AFM) [161]. It is also important to emphasize that although these therapeutic agents are classified as aggregation inhibitors, some of them are actually designed to accelerate the aggregation process. Recently, studies have shown that, compared to the mature amyloid fibrils, the oligomeric intermediates and pro-fibrils are more toxic. The accelerated aggregation can reduce the neurons' exposure to these intermediates and therefore achieve the goal of therapy.

2.6.1. Small Molecule Inhibitors

Small molecule inhibitors could affect A β aggregation by either stabilizing native monomer conformations or restrain peptide-peptide association. Based on their origin, they can be further categorized into two groups: synthetic organic molecules and extracted natural molecules.

Organic molecules. The optical changes observed from many amyloid dyes indicate an interaction between the dye molecules and amyloid structures. These reactions can also be utilized to alter the amyloid aggregation. The two commonly used amyloid dye, CR and ThT, have been found capable to inhibit the amyloid aggregation [162]. A series of inhibitors has been selected from organic dyes and their analogs, including CR derivatives, ThT derivatives, quinone derivatives and polyphenol compounds [22, 23, 162]. Some drugs, used in the treatment of other diseases, have also been found to reduce the cytotoxicity of amyloid, examples being clioquinol [163] and ibuprofen [164]. These drugs normally share a similar structure with the amyloid dyes. The exact inhibition mechanism is still not fully understood. For some inhibitors that are highly hydrophobic, a self-aggregation mechanism was proposed to explain the inhibition effect [165]. These small organic molecules have a high tendency to form colloidal micelles in solution conditions and the formed micelles can non-specifically sequester A β peptides and therefore prevent fibril formation. This explanation is supported by the fact that many small molecular inhibitors can also alter the fibrillization process of other peptides that are prone to aggregation [166]. But this mechanism is not applicable to inhibitors that are soluble. Another possible inhibition mechanism is that the inhibitors have stronger affinities to the proto-fibrils so that the binding site in proto-fibrils are occupied, consequently leading to halting the fibril growth. Again, this hypothesized mechanism can only explain the working principle of inhibitors that function in the elongation phase.

Apart from physical intervention, some inhibitors are designed to degrade preformed A β fibrils and plaques. This kind of inhibitor is normally selected from photosensitizers that have been used in photodynamic therapy (PDT). These photosensitizers are capable to bind with amyloid fibrils and once exposed to light excitation, they are capable to produce reactive oxygen species (ROS)

that can degrade the A β fibrils. By precisely controlling the light exposure, a targeted amyloid inhibition could be achieved in the disease region while leaving healthy tissue intact. One photo-induced amyloid inhibitor of this kind is reported by Lee et al. [20]. The inhibitor, Rose Bengal (RB) is a xanthene dye that could interact with A β 42 and exhibit fluorescence enhancement and redshift. On the other hand, RB has also been used for PDT studies for cancer treatment as a photosensitizer. Lee's group mixed RB with A β 42 monomer solutions and exposed the solutions to a green LED illumination. The aggregation process was monitored by circular dichroism spectroscopy and AFM. Circular dichroism spectroscopy is a technique that measures the difference in absorbance of right- and left-circularly polarized light. The aggregation process of amyloid involves significant changes in the fibrils' secondary structures, which can be revealed by circular dichroism spectroscopy, especially in the range between 180 nm to 260 nm [167]. As shown in Figure 2.12, a clear inhibition effect was observed. The cytotoxicity of the RB-treated A β 42 peptides was also remarkably reduced compared with the untreated one. Similar light-induced inhibition was also reported using ruthenium (II) complex [168], porphyrins [21], carbenoxolone [169] and CRANAD-2 derivatives [170]. For *in vivo* studies, light penetration is a challenge in order to achieve the needed light-induced inhibition. The development of laser-coupled optical fibers that can be directly inserted into animal brains is one solution to deliver light into brains. Another method to extend the light accessibility is to use photosensitizers that can be activated by NIR light. The work reported by Ni et al. is therefore of particular interests. By introducing a bromine atom into an amyloid dye, CRANAD-2, they created a photoactivatable oxygenation catalyst that can be turned on under NIR irradiation. The tissue permeability of NIR light makes it possible to function under mouse skin and even inside mouse brains [170].

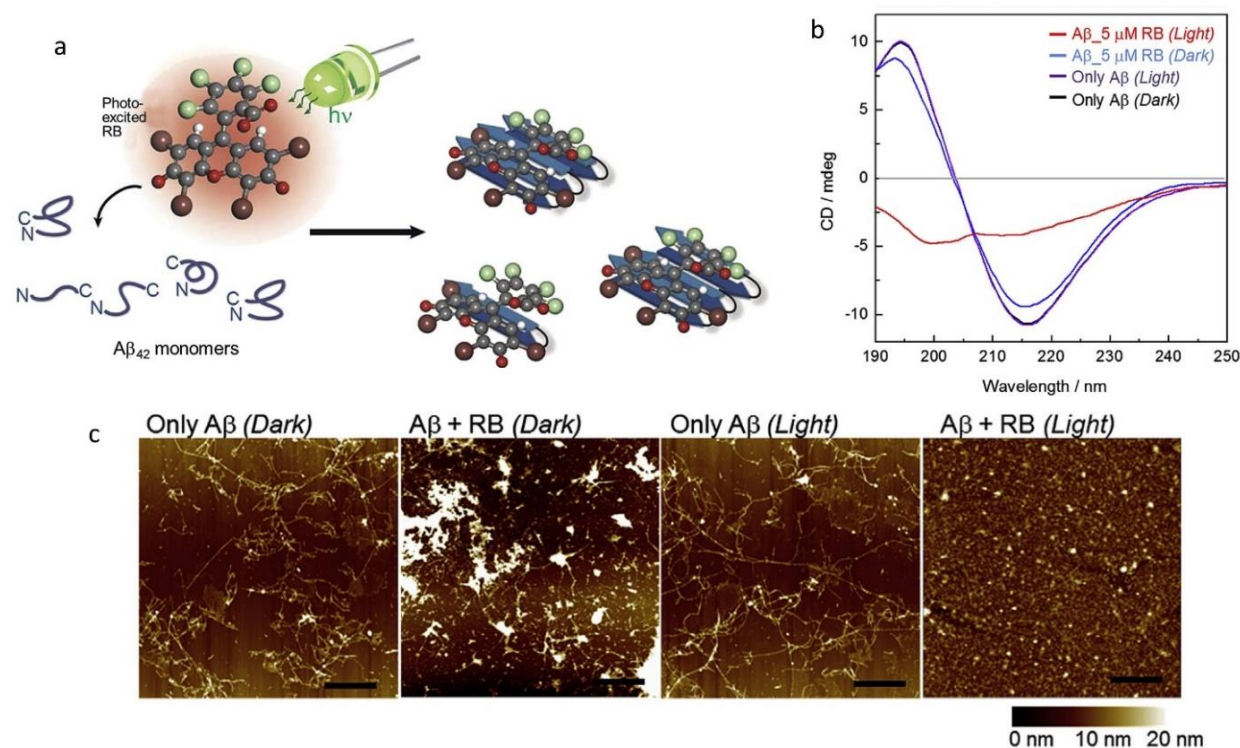


Figure 2.12 Photo-induced inhibition of Aβ₄₂ using RB. (a). Schematic representation of interactions between Aβ₄₂ and photo-activated RB. (b). Circular dichroism spectroscopy and (c) AFM images of Aβ₄₂ in the presence or absence of RB (5 mM) under dark conditions or LED illumination. Adapted from reference [20].

Most inhibitors are designed to prevent amyloid aggregation or even reverse the aggregation process by degrading the preformed amyloid fibrils. The recent discovery of high toxicity of soluble oligomeric amyloid inspired an alternative approach to reducing the overall toxicity of amyloid. That is, instead of slowing down the aggregation, catalytic molecules can be used to accelerate the aggregation in order to transfer the highly-toxic amyloid oligomers into less-toxic or even neutral amyloid conformations. Bieschke et al. developed a membrane-filter retardation assay to quantify large, SDS-stable protein aggregates. Using this assay, their groups selected six compounds that are capable to promote amyloid aggregation. The amyloid aggregation obtained in the presence of these promoters are very stable and non-toxic to neuroblastoma cells [171].

Natural molecules. Apart from synthetic molecules, some natural compounds have also been used for amyloid inhibition. The observation of low AD rate in populations with certain diet leads to the investigation of the relationship between AD and food-origin substances. Most of these compounds are polyphenols such as myricetin, morin, quercetin, which can be extracted from some edible plants including ginkgo biloba, tea bush, grape, and turmeric [172]. Coffee is another potential source of amyloid inhibitors. Coffee contains many natural polyphenols including caffeine, caffeic acid, and chlorogenic acid. Studies have shown that moderate consumption of coffee could help reduce the risk of AD and other dementia, but the exact mechanism is still not fully understood [173]. One of the well-studied amyloid inhibitors found in nature is curcumin. Although currently it can be produced by synthetic methods, curcumin is originally extracted from turmeric. It has long been used as a food additive in Indian cuisine. Curcumin is capable to reduce the cytotoxicity of amyloid in *in vitro* studies. However, the instability and low bioavailability make it difficult to directly apply natural curcumin for AD treatment. To enhance the inhibition efficacy and stability, the curcumin molecules can be modified by adding or replacing certain moieties [174]. Conventionally, the therapeutic effect of curcumin and its derivatives is attributed to the inhibition of amyloid aggregation. However, a recent study published by Thapa et al. provides a new model to explain the curcumin-A β interaction [175]. In their study, they found that the aggregation of A β 40 was not retarded by the addition of curcumin, but the cytotoxicity of A β 40 in the presence of curcumin was reduced. By comparing the structure of the A β 40 fibrils formed with or without curcumin, they concluded that the actual role of curcumin is to provide an alternative pathway in which toxic intermediates are replaced by non-toxic, curcumin bound intermediates (Figure 2.13).

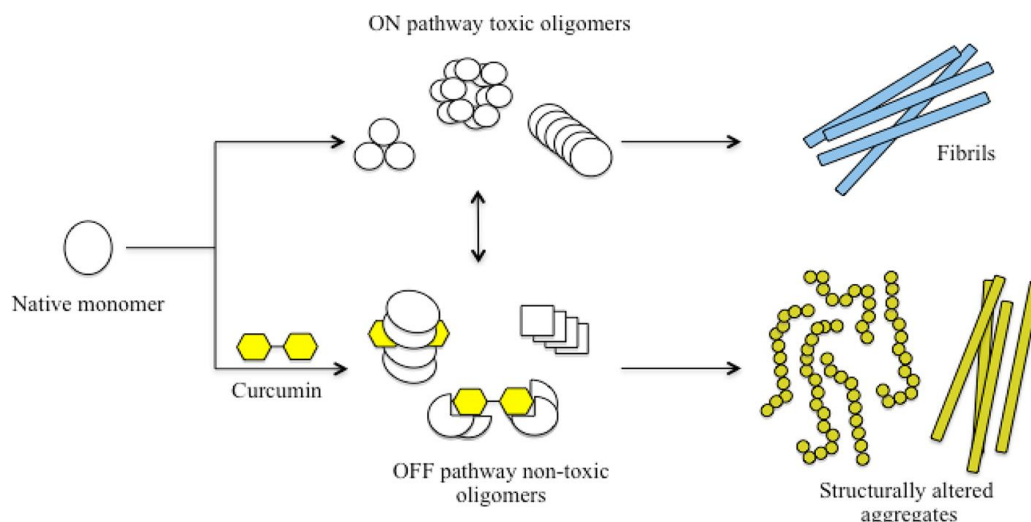


Figure 2.13 Schematic representation of the curcumin-amyloid interaction. Curcumin promotes the formation of nontoxic, off-pathway A β intermediates. Adapted from reference [175].

2.6.2. Peptides Based Inhibitors

Peptides that possess a similar structure with A β peptides could also interact with A β peptides and protofibrils. By doing so, these peptides can regulate the amyloid fibrillization by disrupting the β -sheet formation. Therefore, these peptides are often referred to as β -sheet breakers [176]. To prepare β -sheet breakers, the first thing to do is to identify the key sequence of the A β peptides which is crucial for β -sheet formation. This key sequence is referred to as the self-recognizing motif. Free peptides can bind to the protofibrils through this motif. Once identified, β -sheet breakers can be synthesized by additional chemical modification of the self-recognizing motif. β -sheet breakers are often modified by the following treatment [177]:

- a) Introduction of proline residues – Enhance inhibition effect.
- b) Introduction or substitution of non-natural amino acid – Enhance resistance to enzymatic degradation.
- c) Link with polycationic sequences – Enhance affinity and solubility.
- d) Replace amide bonds with ester bonds – Promote hydrogen bond formation.

It is well-known that the hydrophobic residues in A β peptides play a vital role in the fibrillization process [178]. Naturally, the search for a self-recognizing motif mainly focuses on these hydrophobic regions. The C-terminal residues are more hydrophobic than the N-terminals and therefore they more likely form β -sheet structures [179]. Particularly, the high rigidity of A β 42 peptides is attributed to the interactions involving the C-terminal residues I41–A42 [180]. Based on these observations, Fradinger et al. proposed a hypothesis that C-terminal fragments (CTFs) from A β 42 should have high affinity towards A β protofibrils and they are expected to act as β -sheet breakers. Their groups produced a series of CTFs tested them on A β 42 fibrillization. Two of the CTFs, A β (31–42) and A β (39–42) show significant inhibitory effect. Simulation data suggested that CTFs promote the formation of nontoxic hetero-oligomers which in turn reduce the toxicity of A β 42 peptides [180].

Another hydrophobic region of the A β peptides is located at the central hydrophobic core (CHC) of Leu17-Ala21 (LVFFA). Disruption of the CHC could lead to dramatically change the A β fibrillization rate and binding ability to other A β peptides [181]. Logically, this CHC is often used as a template to design new β -sheet breakers. A series of peptide inhibitors was reported as analogs to CHC, including KLVFF and its N-methylated derivatives, LPFFD, DPFFL and A β (15-25) [162]. The CHC itself can also be functionalized with hydrophobic or hydrophilic moieties, in order to function as an inhibitor.

Generally, inhibitors derived from A β peptides and A β fragments are highly hydrophobic and can easily aggregate in aqueous solution. Addition of charged or hydrophilic residues is often required to enhance the solubility of these inhibitors. Other peptides, such as cyclic peptide [182] and hIAPP peptide [183] have also been used as amyloid inhibitors.

2.6.3. Nanoparticle Based Inhibitors

The interaction between nanoparticles and peptides/proteins has long been an attractive topic in the research community. But the potential of nanoparticles to function as amyloid inhibitors has not been recognized widely until the recent breakthrough in the development of BBB-permeable nanoparticles. By adjusting the size, surface charge and surface functional groups of nanoparticles, they can be used to modulate the folding, fibrillization and degradation of A β peptides. For some nanoparticles, the inhibition effect is due to the interaction between A β peptides and the particles themselves. A β peptides are first absorbed to the surface of these nanoinhibitors and then based on the different surface property, the A β aggregation is retarded, accelerated, or altered. On the other hand, some nanoparticles which do not interact with A β peptides can still be used for amyloid aggregation inhibition by integrating with other inhibitory ligands. In this case, the nanoparticles function as vehicles to deliver the amyloid inhibitors.

Nanoinhibitors. The most important property which dominated the nanoparticle-A β concept is the surface charge which can be manipulated by surface functionalization. Previous studies have shown that electrostatic interactions are major contributing forces in the elongation phase and charged particles could inhibit the fibrillization process by affecting these electrostatic interactions [184-186]. In addition, the highly charged N-terminal residues can also be affected by the particle's surface charge. However, controversial results have been reported on how the polarity of surface charges affects the amyloid aggregation. In the work reported by Liao et al. [186], AuNPs (30 nm) with opposite surface charges are prepared by carboxylic and amine functionalization (amine conjugated AuNPs – positively charged; carboxylic conjugated AuNPs – negatively charged). The two types of surface functionalized AuNPs and bare AuNPs are mixed with A β 40 peptides. The amyloid fibrillization process was monitored by ThT assay and the final morphology of the

amyloid fibrils was characterized by TEM. The results suggested that both carboxyl-AuNPs and bare AuNPs could inhibit the A β 40 fibrillization, but the inhibition effect from amine-AuNPs is negligible. In addition, the negatively charged AuNPs could even promote the fragmentation of preformed amyloid fibrils. Liao et al. attribute the difference in inhibition efficiency to the difference in surface charge. They proposed that the presence of negatively charged particles leads to the formation of short and fragmented fibrils which are unable to participate in further elongation (Figure 2.14). Liao's hypothesis is supported by some other studies on QDs and polymeric nanoparticles [187, 188], which also emphasize the importance of negative surface charge. However, other studies have shown that the positively charged nanoparticles have a greater inhibition effect. This could be explained by the tight binding between the positively charged particles and the A β peptides that carry a net negative charge [185, 189, 190]. These contradictory results are attributed to the synergy effect of several factors including the particle's polarity, size, hydrophobicity and particle/peptide ratio. Recent studies have also found that instead of polarity, the surface charge density of particles is the defining factor for the inhibition efficiency [187, 191].

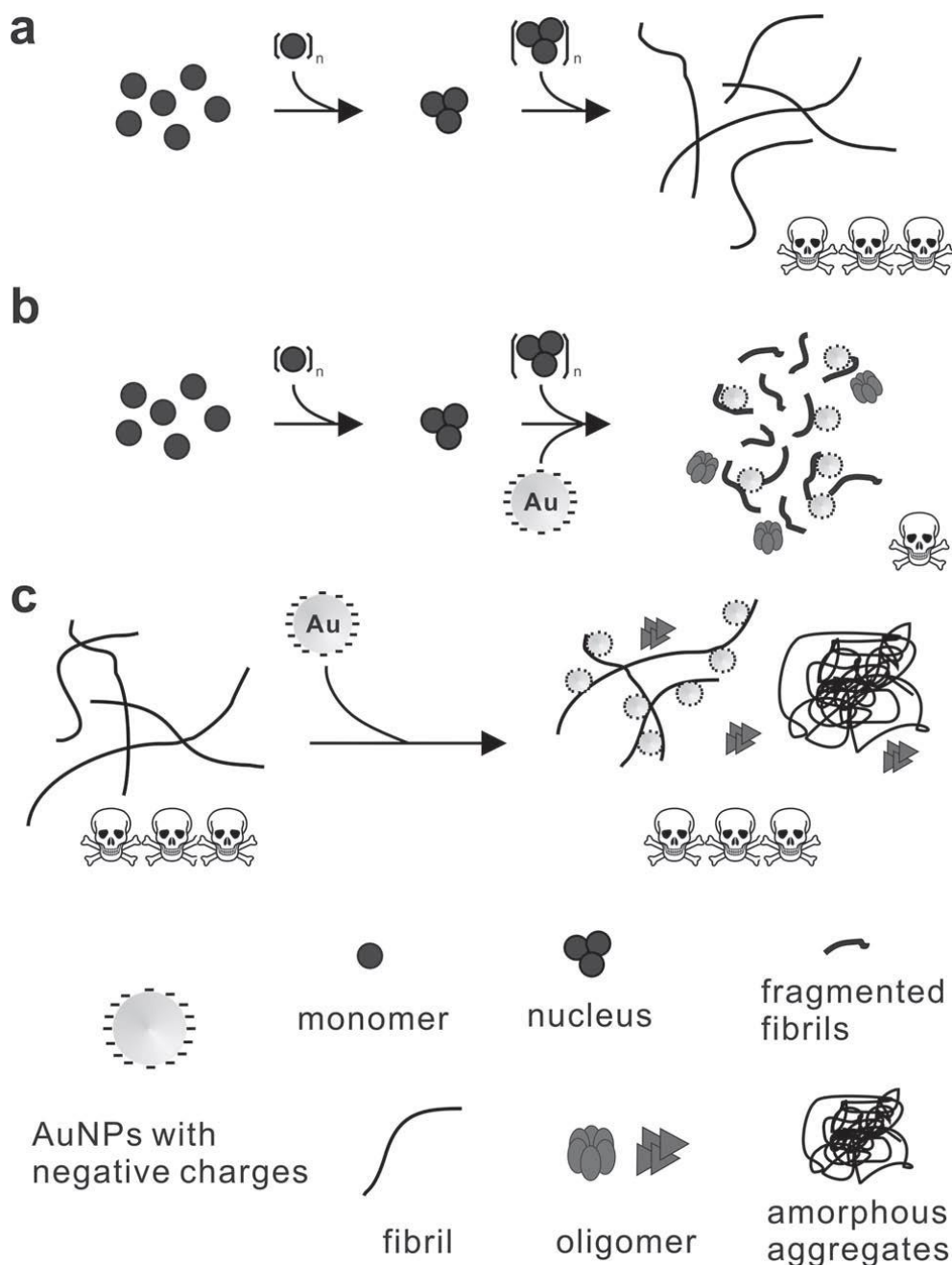


Figure 2.14 Interactions between AuNPs and A β fibrillization. (a) A β peptides aggregate into amyloid fibrils and exert neurotoxicity. (b) In the presence of negatively charged AuNPs, A β peptides form short and fragmented fibrils along with spherical oligomers. The alteration mitigates the toxicity generated from amyloid fibrils. (c) Preformed amyloid fibrils can be degraded by the addition of AuNPs, leading to the production of fragmented fibrils and amorphous aggregates. Adapted from reference [186].

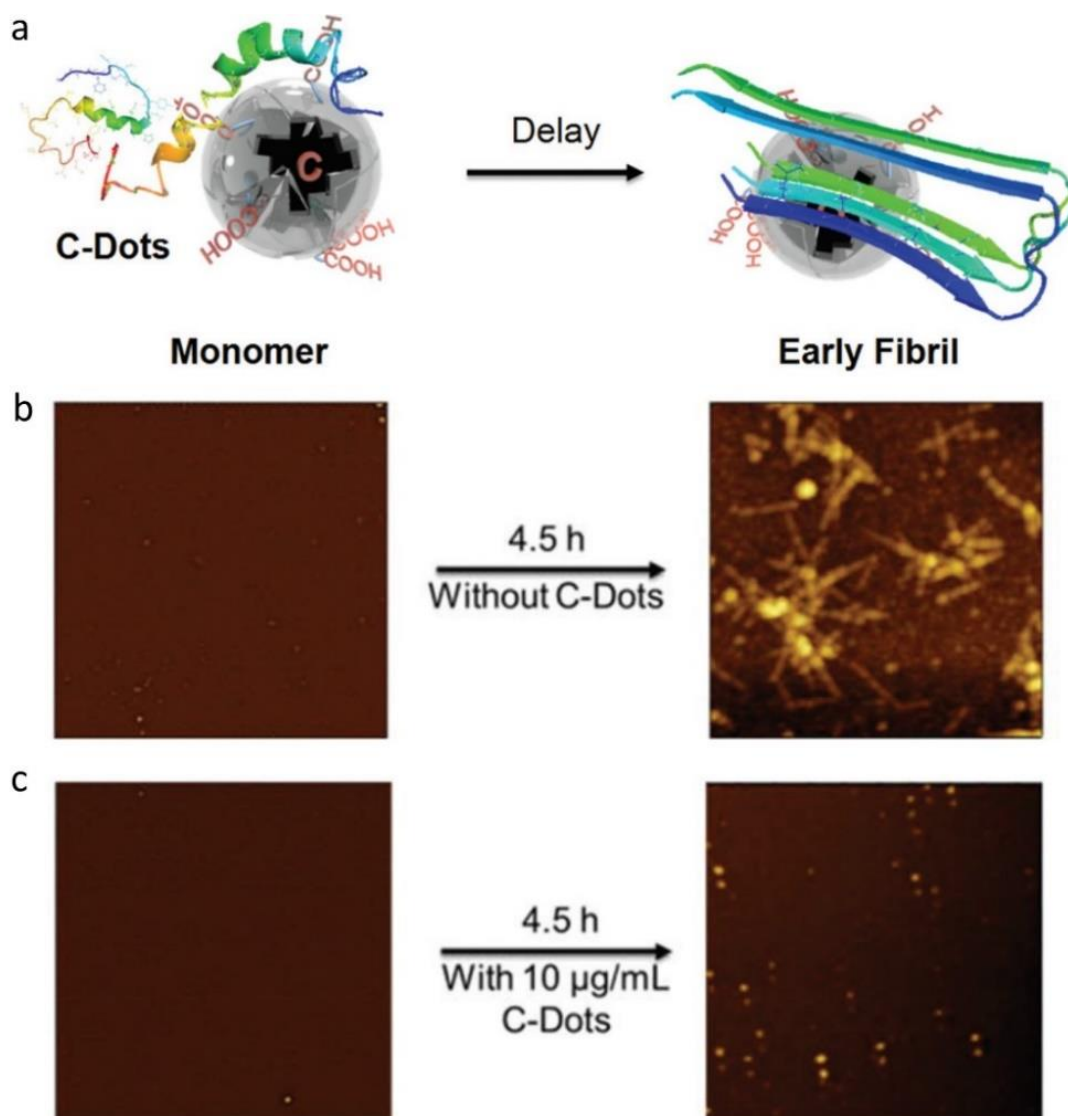


Figure 2.15 Inhibition of Aβ42 fibrillization using C-dots. (a) Schematic representation of C-dots/Aβ42 interactions. AFM images of 10 μM Aβ42 fibrils incubated at 37 °C without C-dots (b) and with 10 μg/ml C-dots (c). Adapted from reference [192].

Among all the categories of nanoparticles, carbon-based nanomaterials have been attracting extraordinary interests in the development of amyloid nanoinhibitors due to their high biocompatibility and biodegradability, ease of synthesis and high feasibility for further functionalization. A variety of carbon nanoparticles, including graphene/graphene oxide, carbon nanotube (CNT), fullerene and C-dots [192-197], has been proved capable to modulate amyloid

aggregation. Due to the ordered structure of CNT and fullerene, the interactions between amyloid peptides and these two types of carbon nanomaterials have been extensively investigated by *in silico* molecular dynamic (MD) studies. The inhibition effect of CNT and fullerene is determined by the surface curvature and numbers of hexagonal rings. Since these two factors affect the balance between hydrophobic interactions, aromatic stacking, and electrostatic interactions. But for C-dots, the amorphous nature of these particles make it difficult to apply similar MD simulations. A very recent study by Han et al. demonstrated the possibility of C-dots as amyloid inhibitors (Figure 2.15) [192]. Although graphene quantum dots have been reported earlier as amyloid inhibitors [198], this study is the first reported case for using such kind of amorphous C-dots for amyloid inhibition. More excitingly, the C-dots were capable to penetrate the BBB in a zebrafish model. However, the C-dots used in their study were produced by acid reflux (110 °C for 15 h) of laser ablated carbon nanopowder. The involvement of high energy laser ablation, long-time reflux and strong acid (sulfuric acid and nitric acid) treatment have compromised the feasibility of production and batch-to-batch stability. In addition, the effect of surface passivation agents of C-dots is still waiting to be investigated.

Just like the small molecular photosensitizer, some nanoinhibitors need to be activated by external excitation before they can interact with amyloids. Yin et al. synthesized PEG-stabilized gold nanostars with ruthenium complexes as additives [199]. To enhance the BBB-permeability of this particle, cell penetrating peptides, penetratins, were conjugated with the nanostars. Once delivered to the brain, the nanostars can absorb NIR light and generate heat. This feature is utilized to conduct photothermal therapy (PTT) for AD. The generated heat can degrade preformed amyloid fibrils.

Nanocarrier. Small molecular inhibitors, peptide inhibitors, antibodies and metal chelators can be conjugated to nanoparticles through covalent bonding or physical absorption. One nanocarrier can host multiple inhibition ligands to generate stronger inhibition effect. Another advantage of using a nanocarrier is to enhance the BBB penetration, particularly for those inhibitors that are hydrophilic. A prototype nanoparticle-chelator conjugate (Nano-N2PY) was synthesized by conjugating the iron chelator CMC with carboxylic functionalized polystyrene nanoparticles (240 nm) [200]. Nano-N2PY was then mixed with A β peptides and incubated with human cortical neuronal cells (HCN1A). The results show that Nano-N2PY is capable to reduce the toxicity of A β peptides. In addition, the co-incubation of Nano-N2PY also prevented the formation of amyloid fibrils, confirmed by Congo red staining. Metallic nanoparticles can also be used as nanocarriers. Skaat et al. conjugated A β fragment Leu-Pro-Phe-Phe-Asp (LPFFD) with IONPs [201]. *In vitro* ThT assays show that the conjugated IONPs could effectively inhibit A β fibrillization. In addition, the magnetic nature of IONPs suggests a potential to use external magnetic-field for the guided particles delivery.

2.7. Outcomes of Literature Review

The application of nanoparticles for the diagnosis and treatment of AD is receiving increasing interests in the biomedical community. Nanoprobes, especially MFNPs, have achieved an impressive success in cancer diagnosis. Compared to small molecular probes, those MFNPs that can be detected by different diagnostic techniques could help us to obtain more comprehensive and more precise pathological information. Targeting ligands that are conjugated with MFNPs enable the specific targeting of biochemical disease biomarkers. Further, MFNPs can be conjugated with therapeutic agents in order to become a theranostic agents, which, in turn, facilitate the optimization of drug efficacy and specificity. However, the advantages of MFNPs

have not been recognized widely in the diagnosis of AD. Although several nanoprobe have been utilized to image and detect amyloid peptides or plaques, these nanoprobe can only be used for a single modality. Moreover, most of the reported nanoprobe are designed to target extracellular amyloid. As discussed in this literature review, the uptake of extracellular amyloid by neuronal cells are playing an important role in the pathogenesis of AD. But this event has in the past been interrogated by small molecule based probe only.

The usage of nanoinhibitor is a promising therapy for AD. These nanoinhibitor are capable to modulate the A β aggregation either by directly interacting with A β peptides or by the delivery of inhibitory ligands to the site of amyloid fibrillization. However, there is a serious concern about the biocompatibility and clearance of these nanoinhibitor. The BBB poses a big challenge to the delivery of nanoparticles to the brain. Once the particles entered the brain, it's also difficult to clear them from the brain. For nanoparticles that are circulating in the peripheral system, most of them will be cleared either through phagocytic uptake in the liver and the spleen, or by renal clearance in the kidneys. The circulation half-life is normally between several hours and a few days [202-204]. During the past decades, the short-term and long-term biocompatibilities of these peripheral-circulating particles have been investigated extensively. On the other hand, there has been very limited research on tracking the long-term fate of nanoparticles that have been delivered to the brain. Disdier et al. tracked the circulation of titanium dioxide (TiO₂) nanoparticles that have been delivered to mice brains. TiO₂ particles can be detected in the brain 28 days after the injection and the overall clearance took more than one year [205]. Although most nanoinhibitor used in AD research are decorated with biocompatible coatings, the long retention of cerebral particles means that there is a high risk for the release of toxic substances after the breakdown of surface coating. The risk is particularly high for QDs since most ODs contain highly toxic heavy metal ions. In

addition, metallic nanoparticles are believed to be neurotoxic due to the particle-induced oxidative stress [40]. Considering the aforementioned concerns, non-metallic nanoparticles such as C-dots might be a more appropriate choice for amyloid inhibitors.

Currently, the interaction between C-dots and A β peptides is poorly investigated. Only one study has been reported to use C-dots as amyloid inhibitors, and the C-dots used in that research were made by top-down synthesis. The other preparation approach, bottom-up synthesis, has not been used to prepare C-dots-based amyloid inhibitor.

In summary, the following three research gaps have been identified:

- a) There are limited multifunctional nanoprobe that have been applied for amyloid diagnosis.
- b) There is a demand to prepare C-dots-based inhibitors from more facile methods. The effect of different passivation agents on the C-dots' inhibitory effect also needs to be investigated.
- c) There is a research need to develop nanoprobe that can specifically target neuronal cells which are involved in the cellular uptake of amyloid peptides.

The next chapter will present a Raman/fluorescent bifunctional nanoprobe that can be used for amyloid detection. The synthesis, characterization, and application of the nanoprobe will also be discussed in detail.

Chapter 3: Bifunctional Nanoprobe for the Detection of Amyloid

This chapter describes the research and development of a Raman/fluorescent bi-functional nanoprobe that can be used for the detection of amyloid. This nanoprobe is prepared by conjugating gold AuNPs with Rose Bengal (RB) dye. RB is chosen due to its unique Raman fingerprints and affinity with A β peptides. The morphology and optical properties of the nanoprobe were studied through comprehensive characterization techniques. Particularly, the SERS effect of the nanoprobe is discussed in detail. The interaction between the nanoprobe and A β 42 was carefully investigated. Upon binding with A β 42 peptides, a spectrum change was detected in the nanoprobe's Raman spectrum, and the magnitude of the spectrum changes can be correlated with the concentration of the target peptides. The peptide/probe interaction also induced a remarkable enhancement in the probes' fluorescence emission. This fluorescence enhancement was further utilized to image amyloid plaques in the brain slices of transgenic mice.

3.1. Introduction

Rose Bengal (RB) is a fluorescein derivative widely used as a tumor-targeting dye for oral cancer diagnosis [206, 207]. Commercially, RB is normally available in the form of disodium salt (see the structure in RB in Figure 3.1). By conjugating with gold nanoparticles, the unique SERS spectrum of RB has been exploited for Raman imaging [208]. Interestingly, RB also shows a strong affinity to A β peptides and therefore it has been used as an inhibitor of A β aggregation [20, 209]. Inspired by these phenomena, we tried to conjugate RB with spherical, amine-functionalized AuNPs to generate an RB-AuNPs complex. The RB-AuNPs exhibited a significant change of SERS spectrum when mixed with A β 42 peptides solutions. In addition, the fluorescence emission of the RB-AuNPs was considerably enhanced by the presence of A β 42 peptides. This behavior is

similar to that of the commonly used amyloid dye, ThT. Therefore, we further tested the feasibility of using RB-AuNPs for fluorescence imaging of amyloid plaques in mouse brain tissue harvested from transgenic mice that can express human amyloid peptides. The results suggest that the conjugated RB-AuNPs can be used as bifunctional probes for amyloid detection and, consequently, as a diagnostic tool for the onset of AD.

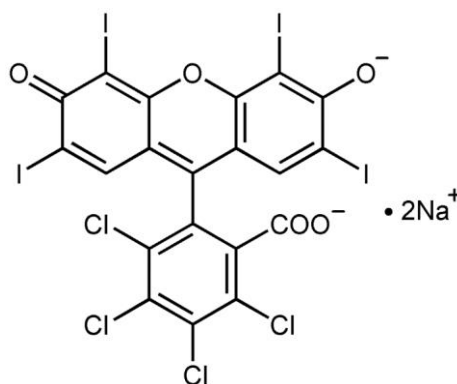


Figure 3.1 Structure of RB. Commercially, RB is available in the form of disodium salt.

3.2. Design and Synthesis of RB-AuNPs

As discussed earlier, RB dye was chosen due to its unique Raman spectrum and affinity towards A β peptides. The choice of spherical AuNPs, however, is a bit more complicated. It is well known that non-spherical AuNPs (nanorods, nano-triangles and nano-stars) may produce a stronger SERS effect than spherical AuNPs, and they also exhibit higher photo-toxicity due to their stronger absorption [210]. RB is capable to function as a photosensitizer for PDT [211]. By conjugating with gold nanorods, the synergy from the photodynamic effect of RB and the photothermal effect of gold nanorods leads to an enhanced, photo-induced cytotoxicity [212]. For therapeutic applications, this enhanced cytotoxicity is a desirable feature that increases the therapeutic efficiency. However, for diagnostic applications the enhanced cytotoxicity is a disadvantage. In addition, at the same volume, the spherical nanoparticles have a higher mitigation rate than shape-

anisotropic nanoparticles, which enables a faster probe delivery in biological systems [213]. Taking the aforementioned two factors into consideration, spherical AuNPs are used instead of non-spherical AuNPs. The overall synthesis is conducted in two steps as illustrated in Figure 3.2. The carboxylic groups in the RB molecules are first activated by EDC (1-ethyl-3-(3-dimethylaminopropyl)carbodiimide hydrochloride) in MES buffer (4-morpholinoethanesulfonic acid, pH =5.0). After the activation, the carboxylic groups were transformed into active O-acylisourea intermediates. These intermediates can easily be substituted by primary amino groups. The substitution leads to the formation of a stable amide bond with the release of EDC as by-products. O-acylisourea intermediates are very unstable in aqueous solution and will quickly return to the unreactive carboxylic groups if they are not able to react with amine groups. In order to maximize the conjugation efficiency, NHS (N-hydroxysuccinimide) is also added to the reaction mixture. NHS can react with the O-acylisourea intermediates to form a more stable NHS ester which can still react with amine groups. The detailed synthesis can be found in the appendix.

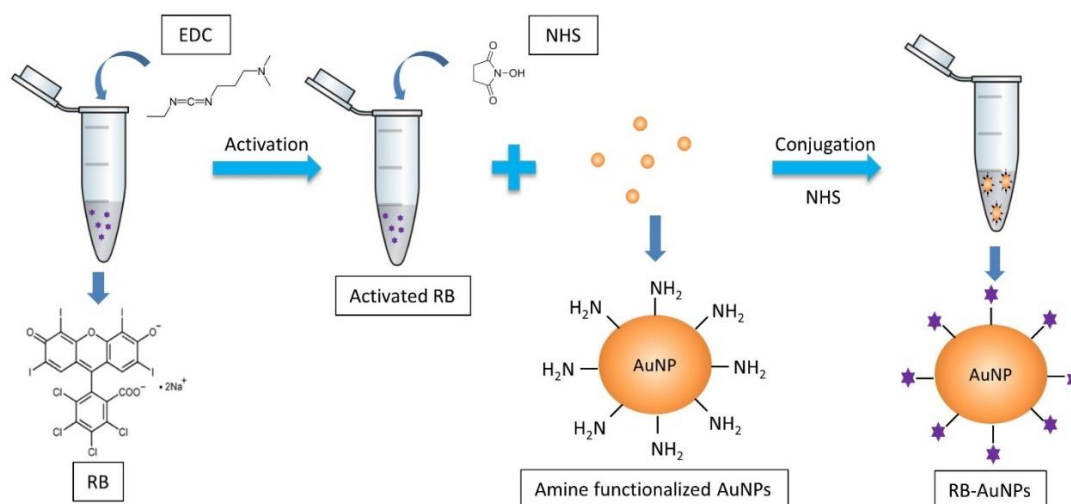


Figure 3.2 Scheme for the EDC/NHS facilitated conjugation. The carboxylic groups in the RB molecules are first activated by EDC and then conjugated with the amine groups on the surface of the AuNPs, in the presence of NHS as the catalyst.

3.3. Characterization of RB-AuNPs

The TEM image of the functionalized RB-AuNPs is demonstrated in Figure 3.3a. It can be measured that the average diameter of the RB-AuNPs is 28 ± 3 nm. Due to the small size of conjugated RB moieties, the TEM images failed to show detectable changes in the core size of the nanoparticles before and after the conjugation. The RB-AuNPs maintained their good dispersity in aqueous solution, suggesting that the original anti-aggregation surface coating of the AuNPs was not deteriorated by the RB conjugation. When particles are suspended in solutions, solvent ions will be absorbed onto the particles' surface to form two parallel layers. The first layer, a compact layer, is formed by ions that are bounded to the particles' surface through strong chemical interactions. Since this layer is very close to the particles' surface, the charges in this layer are also referred as surface charges. The second layer, which is slightly further away from the particles' surface, is composed of ions that are electrostatically attracted by the surface charge. Since the electrostatic attractions are much weaker than the chemical bonds that contribute to the formation of the compact layer, the linkage between the second layer and the particles are loose and unstable. Extrinsic factors such as an external electric field and temperature changes can mobilize the ions in the second layer. Therefore, the second layer is also known as the diffuse layer. The outermost plane of the diffuse layer, which defines the boundary between affected and free solvent, is called the slipping plane since this plane can be moved by tangential forces. The charge on the slipping plane is defined as the zeta potential. Since the surface charge in the inner layer is electrically screened by charges in the outer layer, the zeta potential is normally used to characterize the apparent surface charge of particles in solution. Figures 3.3b and 3.3c show the zeta potential distribution for the AuNPs before and after the RB conjugation. The apparent zeta potential

changed from -8.43 ± 3.68 mV to -17.2 ± 7.32 mV due to the conjugation of negatively charged RB molecules.

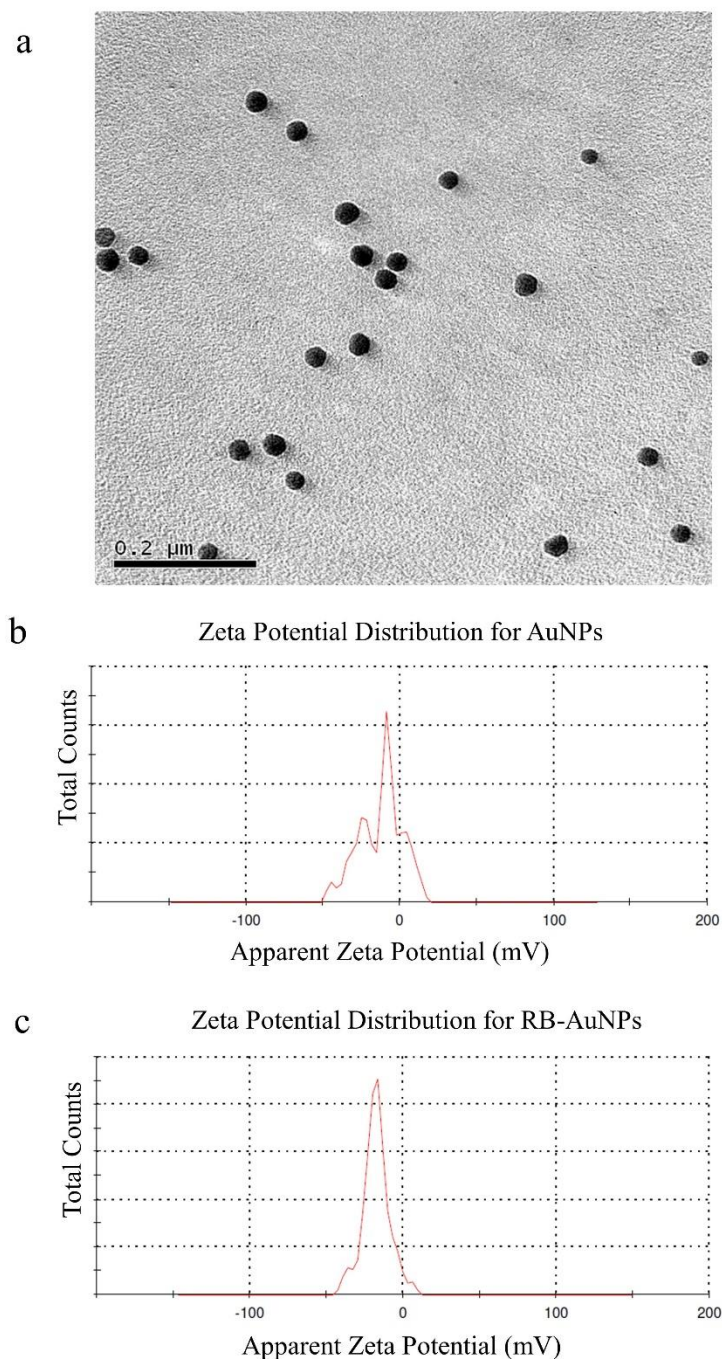
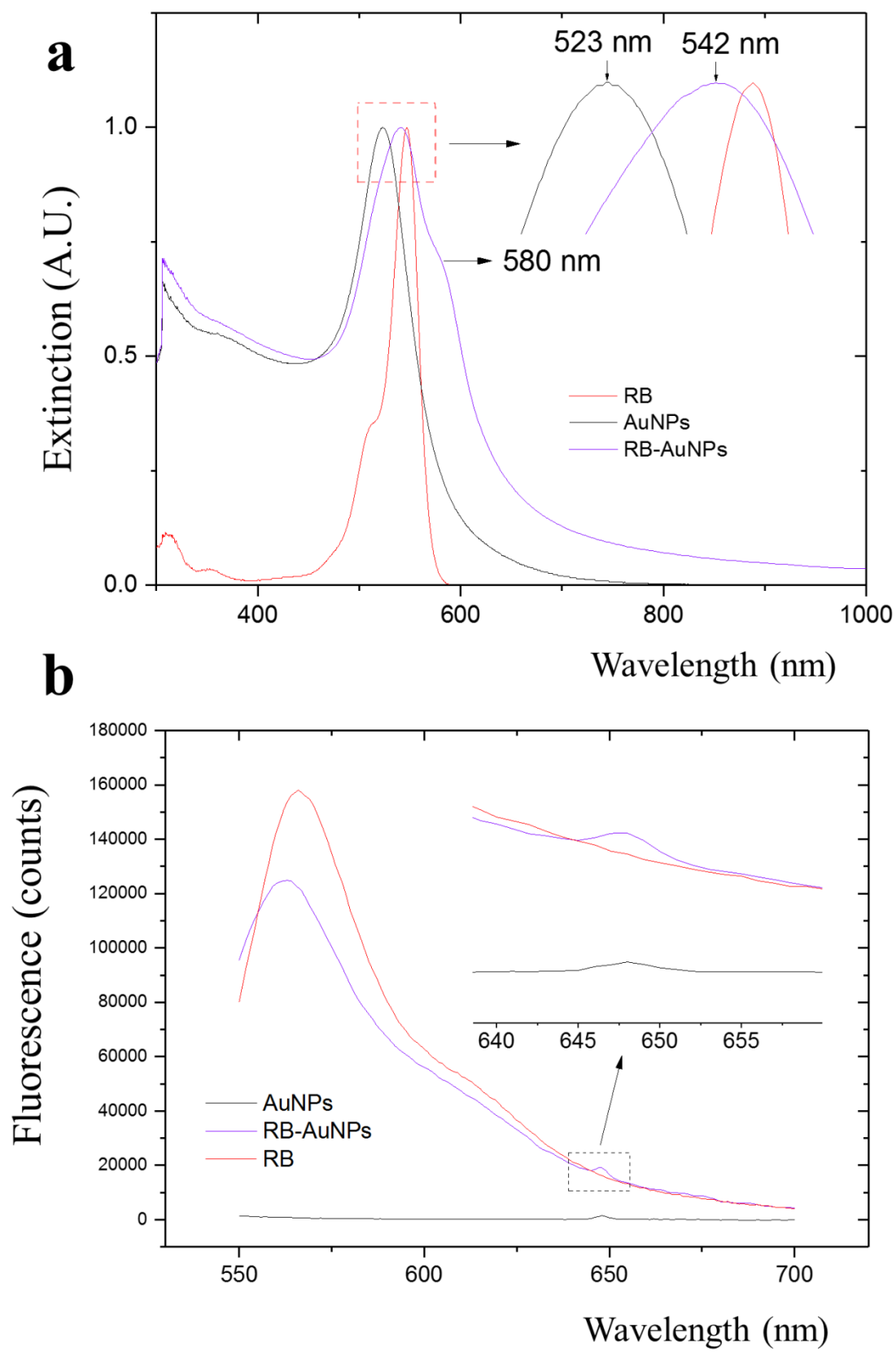


Figure 3.3 Morphology and zeta potential of RB-AuNPs. (a) TEM images of the RB-AuNPs, whose average diameter is 28 ± 3 nm. (b) and (c) Zeta potential distribution for the unfunctionalized AuNPs (upper, -8.43 ± 3.68 mV) and RB-AuNPs (lower, -17.2 ± 7.32 mV).



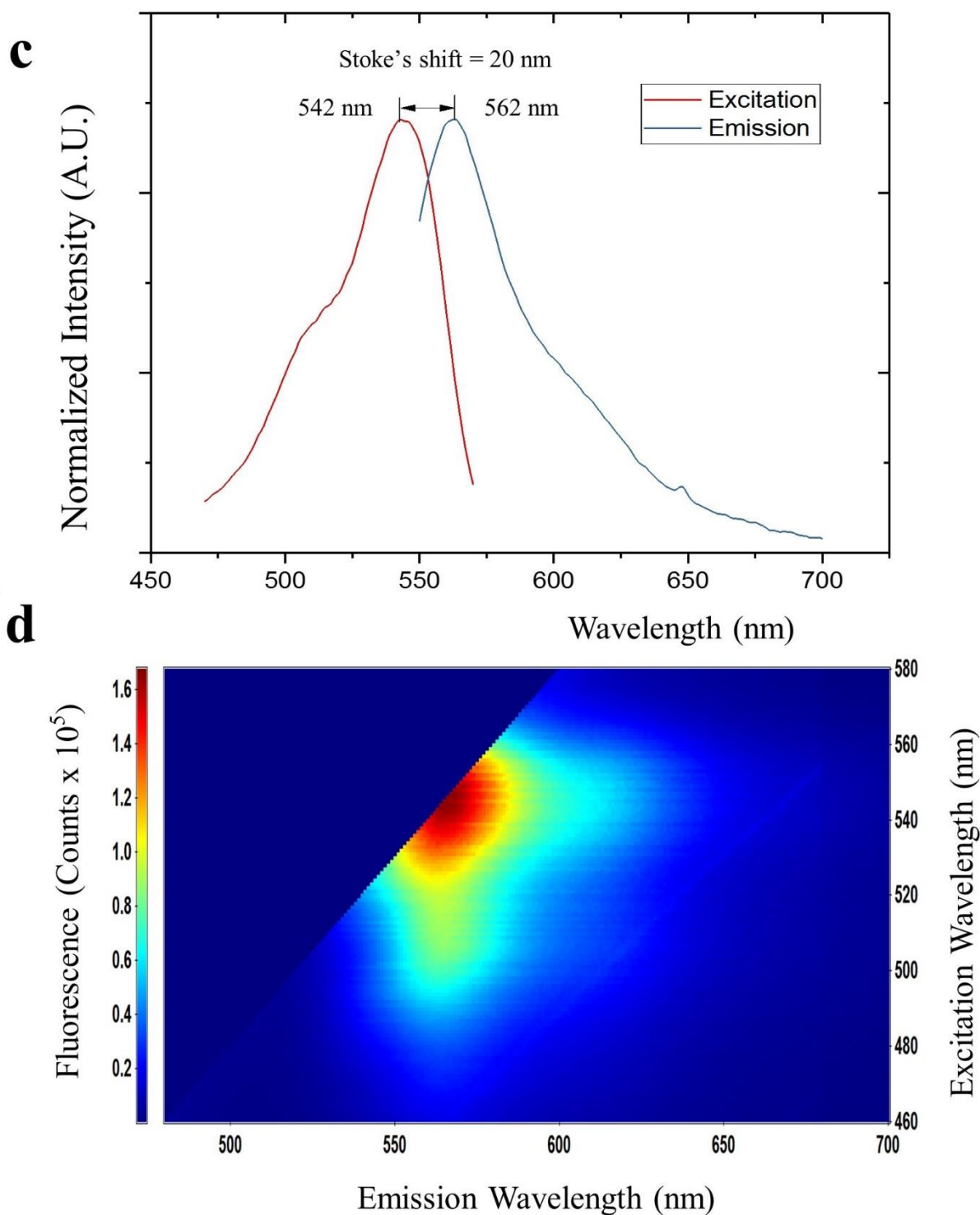


Figure 3.4 Optical properties of RB-AuNPs. (a) Extinction spectra of RB, AuNPs and RB-AuNPs. (b) Emission spectra of RB, AuNPs and RB-AuNPs under 530 nm excitation. (c) Excitation-emission spectra of RB-AuNPs, the excitation spectrum was obtained at a fixed emission of 590 nm. (d) Emission map of RB-AuNPs, plotted by setting the x-axis as emission

wavelength and y-axis as excitation wavelength. The color represents the relative peak intensity of the emission.

The optical properties of RB-AuNPs were characterized by UV-Vis and fluorescence spectrometer. Figure 3.4a shows the extinction spectra of the AuNPs, RB and RB-AuNPs. Compared to the original AuNPs, the extinction peak of the RB-AuNPs shows a red shift of 19 nm (523 to 542 nm) and an additional minor peak at the 580 nm wavelength. These changes could be attributed to the changes of surface environment [214], which are considered as a proof for the successful conjugation between RB and nanoparticles [212, 215]. The emission spectra (Figure 3.4b) of the AuNPs, RB and RB-AuNPs further prove the absorption of RB on the surface of AuNPs. The fluorescence of RB was not quenched by the conjugation, and the weak photoluminescence (PL) of AuNPs at 648 nm was also retained after the conjugation. This PL of AuNPs is caused by the particle plasmon [216]. The excitation-emission spectrum of RB-AuNPs is shown in Figure 3.4c, the Stoke's shift of RB-AuNPs was calculated to be 20 nm. The emission map of RB-AuNPs (Figure 3.4d) indicates that the emission peak is at 562 nm (542 nm excitation).

The cytotoxicity of the RB-AuNPs was measured by incubating different concentrations of RB-AuNPs with human embryonic kidney cells (HEK-293). The viability data was obtained by MTT assay. MTT (3-(4,5-Dimethylthiazol-2-yl)-2,5-Diphenyltetrazolium Bromide) is a tetrazolium dye that can be reduced to purple formazan by NAD(P)H-dependent cellular oxidoreductase enzymes. This reaction can only take place in the mitochondria of live cells. Therefore, the amount of generated formazan is linearly related to the number of live cell in a culture compartment. Formazan is insoluble in aqueous solutions such as culture medium but can be dissolved by organic solvents. In MTT assay, dimethyl sulfoxide (DMSO) is normally used to dissolve the generated formazan. For homogenous formazan solutions, the total amount of formazan can be quantified by

the absorbance in a certain wavelength. For DMSO solution, the sample absorbance (A_x) is measured at 570 nm and background absorbance (A_b) is measure at 630 nm. By comparing the absorbance measured from experimental and control groups, the relative viability of experimental groups can be calculated (Formula 3.1) [217].

$$\text{Relative viability} = (A_{\text{sample}} - A_b) / (A_{\text{control}} - A_b) \times 100\% \quad \dots\dots\dots 3.1$$

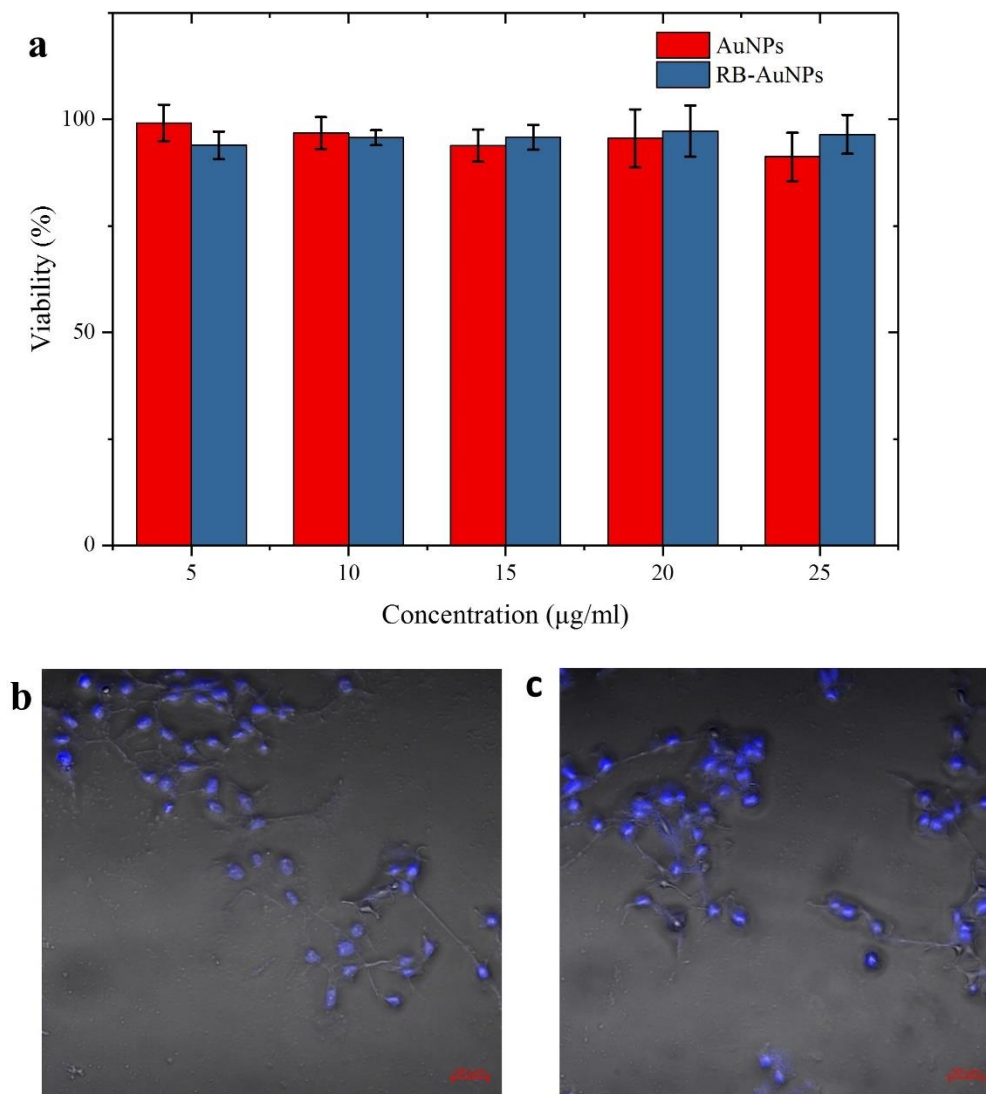


Figure 3.5 Biocompatibility of RB-AuNPs. (a) Cell viability assay of HEK-293 cells incubated for 24 hours with AuNPs and RB-AuNPs. The viability was measured by MTT assay. Three independent experiments were conducted for each concentration. (b) and (c) Confocal images of

HEK-293 cells after 24-hour incubation in the presence or absence of RB-AuNPs: (b) control and (c) incubated with 20 $\mu\text{g/ml}$ of RB-AuNPs. The cells nuclei were stained with DAPI (blue).

The results of the MTT assay are listed in Figure 3.5a. AuNPs are generally considered as biocompatible materials [86]. But RB molecules may produce toxic reactive oxygen species (ROS) under green light excitation, which can cause cell death [215, 218]. From the MTT results, we can see that the functionalized RB-AuNPs are equally biocompatible as compared to the original AuNPs. Even at a relatively high incubation concentration (25 $\mu\text{g/ml}$), the cell viability is still greater than 95%. Apart from the cell proliferation assay, the morphology of the cells is another important indicator of the particles' biocompatibility [219]. Figures 3.5b and 3.5c show the confocal images of HEK-293 cells after 24-hour incubation in the presence or absence of RB-AuNPs, respectively. The treated cells showed no detectable changes in the cell morphology compared with the control cells. The shapes of cell nuclei also remain intact. These observations further prove the excellent biocompatibility of the RB-AuNPs. This high viability could be attributed to the limited light dose during the cell culture.

3.5. SERS Enhancement of RB-AuNPs

In this work, the conjugated RB molecules served as both fluorescence and Raman reporters. Figure 3.6 shows the Raman spectra of RB, AuNPs and RB-AuNPs. The free RB molecules show very weak Raman signals and the peaks are overwhelmed by the background signals. The un-conjugated AuNPs shows certain Raman peaks, these peaks are attributed to the pre-existed polyethylene glycol-amine (PEG-NH₂) coating on the surface of AuNPs and the strong peak at 200 to 400 cm^{-1} is caused by the metal-oxygen linking [220]. The Raman spectrum of RB-AuNPs shows a significant SERS effect, especially for the two major peaks located at 1490 and 1610 cm^{-1} . Based on previously reported studies [221, 222], these two major peaks are attributed to the

symmetric (for 1610 cm^{-1}) and asymmetric (for 1490 cm^{-1}) stretching of C=C bonds in the aromatic rings. It is well known that the SERS effect will preferentially enhance the bands which correspond to the vibrations that cause changes in the polarization perpendicular to the metal surface [222]. Therefore it is reasonable to deduce that the RB molecules are connected with AuNPs through the linking between the carboxylic groups of RB and the surface amine groups of AuNPs.

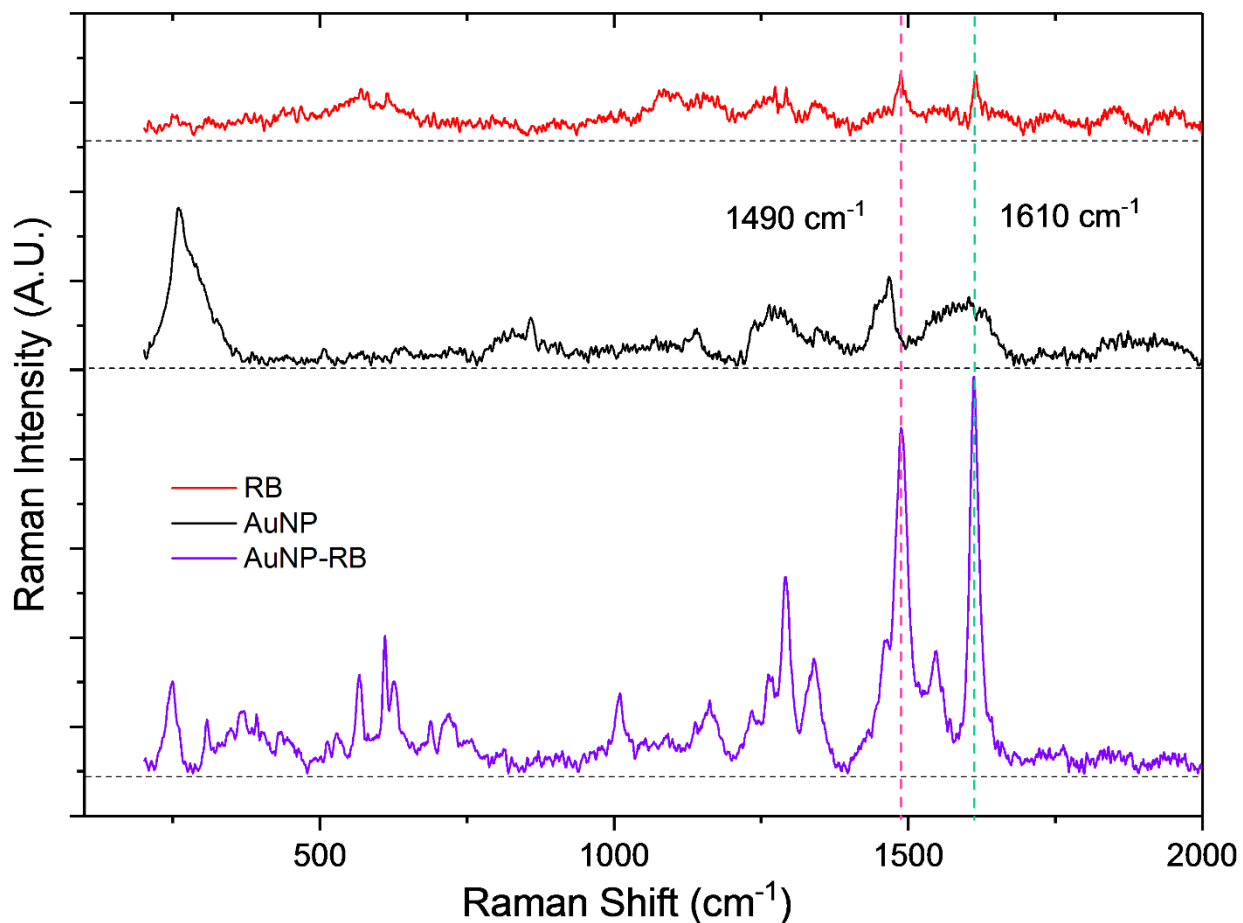


Figure 3.6 Raman spectra of RB, AuNPs and RB-AuNPs. The dashed line represents the baseline for each Raman spectrum. It is clear that the two peaks at 1490 cm^{-1} and 1610 cm^{-1} are most significantly enhanced after the conjugation.

3.6. Interactions between A β 42 and RB-AuNPs

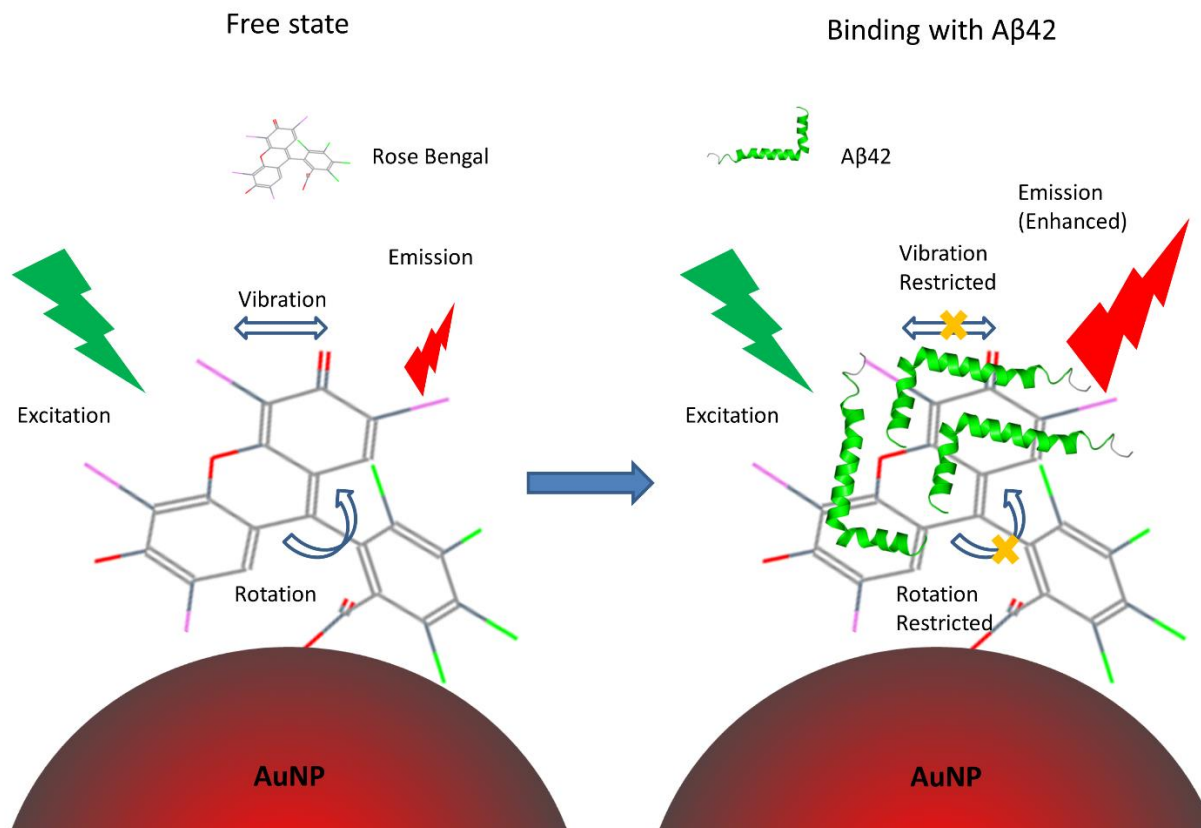


Figure 3.7 Schematic illustration of the interaction between RB-AuNPs and A β 42. Prior to the peptides binding, the energy from the excitation photons can be released by the rotations and the vibrations of RB molecules. The vibrations and rotations are restricted by the peptide binding, leading to an enhanced fluorescence.

Previous studies have reported that the fluorescence of free RB molecules can be significantly enhanced upon mixing with A β 42 peptides [20]. Several other fluorophores have also shown similar fluorescence enhancement when mixed with peptides, and this enhancement phenomenon is considered as a proof of dye-peptide association [223-225]. As shown in Figure 3.1, RB molecules contain two moieties that are linked by a C-C bond. This structure is very similar to that of ThT dye, and hence the RB-A β 42 interaction is believed to be an analogue to the ThT-A β 42

interaction (Figure 3.7). At free state, the majority of the energy from the excitation photons can be released by the rotations and the vibrations of RB molecules, leading to a relatively low fluorescence emission (RB's quantum yield is 0.5% in PBS [226]). Upon binding with A β 42 peptides, the molecular rotations and vibrations are restricted, and therefore more energy has to be released by photon emission, causing an enhanced fluorescence. From Figure 3.8a, it can be found that the fluorescence emission of both stand-alone RB (1 μ M) and RB-AuNPs (1 μ g/ml) were notably enhanced when mixed with A β 42 peptides, and the enhancement increased with the amount of added A β 42. It is interesting to note that the relative fluorescence enhancement of RB-AuNPs is actually slightly higher than that of free RB. This can be explained by the absorption of A β 42 peptides on the surface of RB-AuNPs that leads to a higher interaction possibility between A β 42 peptides and RB molecules. Such peptide localization has been reported when mixing A β peptides with charged nanoparticles [186, 227]. Figure 3.8b further indicates that the ThT and RB-AuNPs share a common binding pathway with A β 42 peptides. The ThT fluorescence was remarkably reduced after the addition of RB-AuNPs.

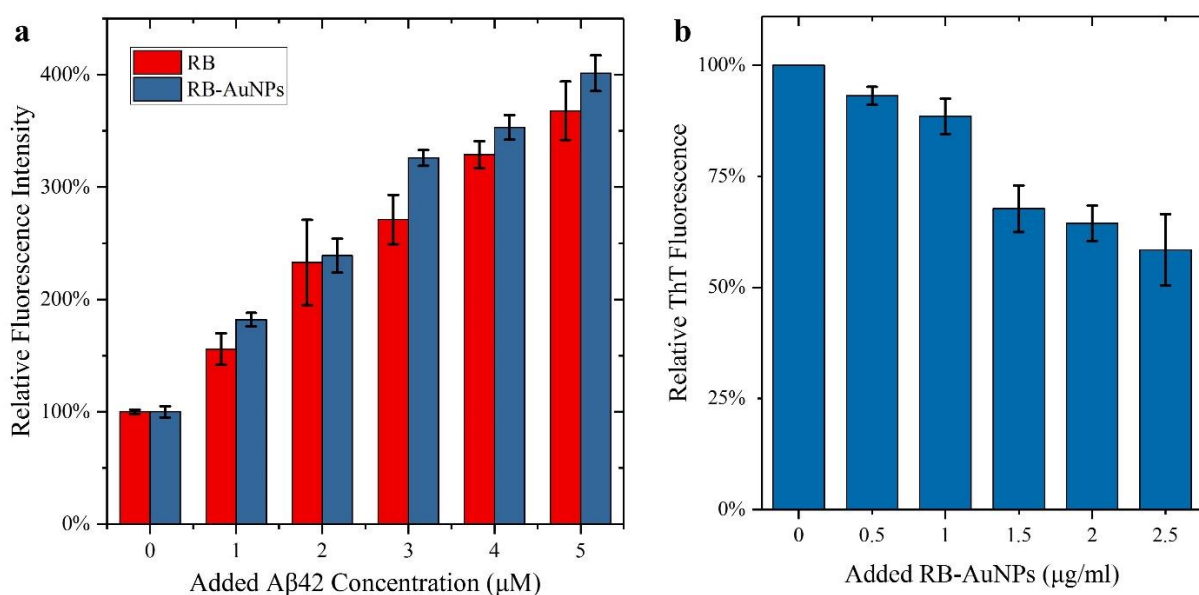


Figure 3.8 Fluorescence enhancement of RB-AuNPs and the effect of RB-AuNPs on ThT fluorescence. (a) Fluorescence enhancement of RB-AuNPs (1 μ g/ml) and free RB (1 μ M). The

relative enhancement is calculated by comparing the fluorescence intensity (560/590 nm ex/em) before and after the addition of A β 42 peptides. (b) The changes of ThT fluorescence (10 μ M, mixed with 10 μ M of A β 42 peptides) after the addition of different concentrations of RB-AuNPs.

The presence of nanoparticles has been found capable to affect the fibrillization process of amyloid peptides, and this phenomenon is considered as a proof of the particles-peptides interaction [186, 228]. The effect of RB-AuNPs on the A β 42 fibrillization was investigated by incubating A β 42 with RB-AuNPs. The resultant amyloid aggregates were characterized by TEM. As shown in Figure 3.9, when incubated with RB-AuNPs, the A β 42 aggregation process was clearly inhibited (Figure 3.9b), compared to the control group (Figure 3.9a). This altered aggregation indicated the strong affinity between RB-AuNPs and A β 42 peptides, which reduced the quantity of available A β 42 oligomer for self-fibrillization.

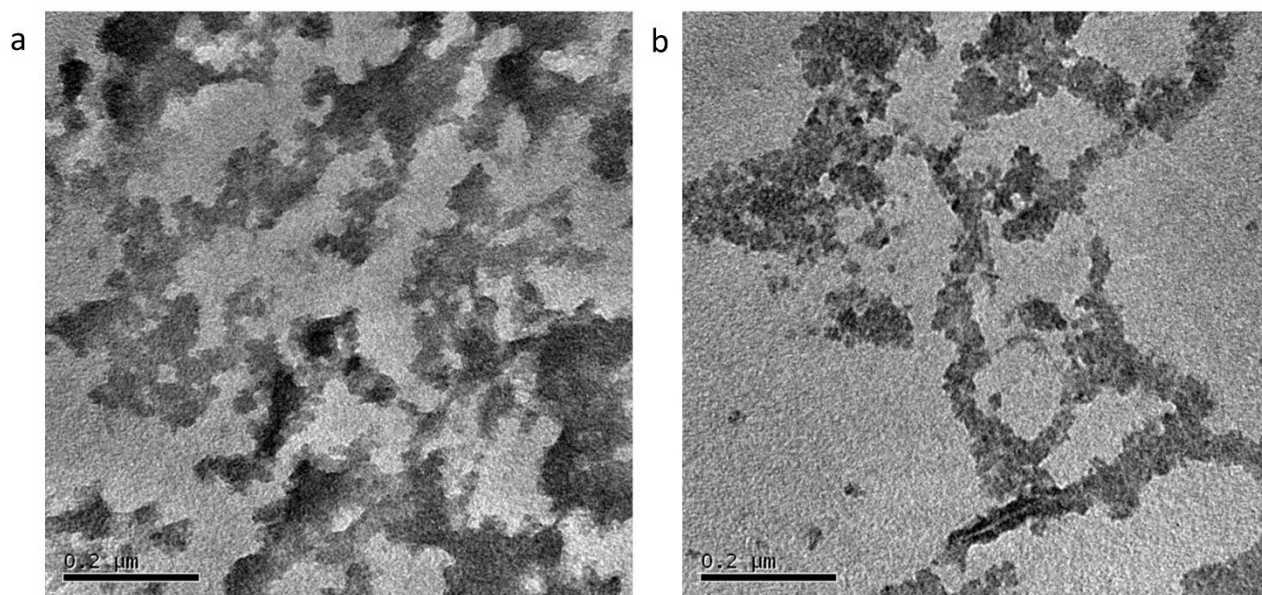


Figure 3.9 The morphology of 10 μ M A β 42 after 6 hours of incubation. (a) Incubated alone and (b) incubated in the presence of 10 μ g/ml RB-AuNPs. Incubation was conducted at 37 $^{\circ}$ C.

3.7. SERS detection of A β 42 peptides

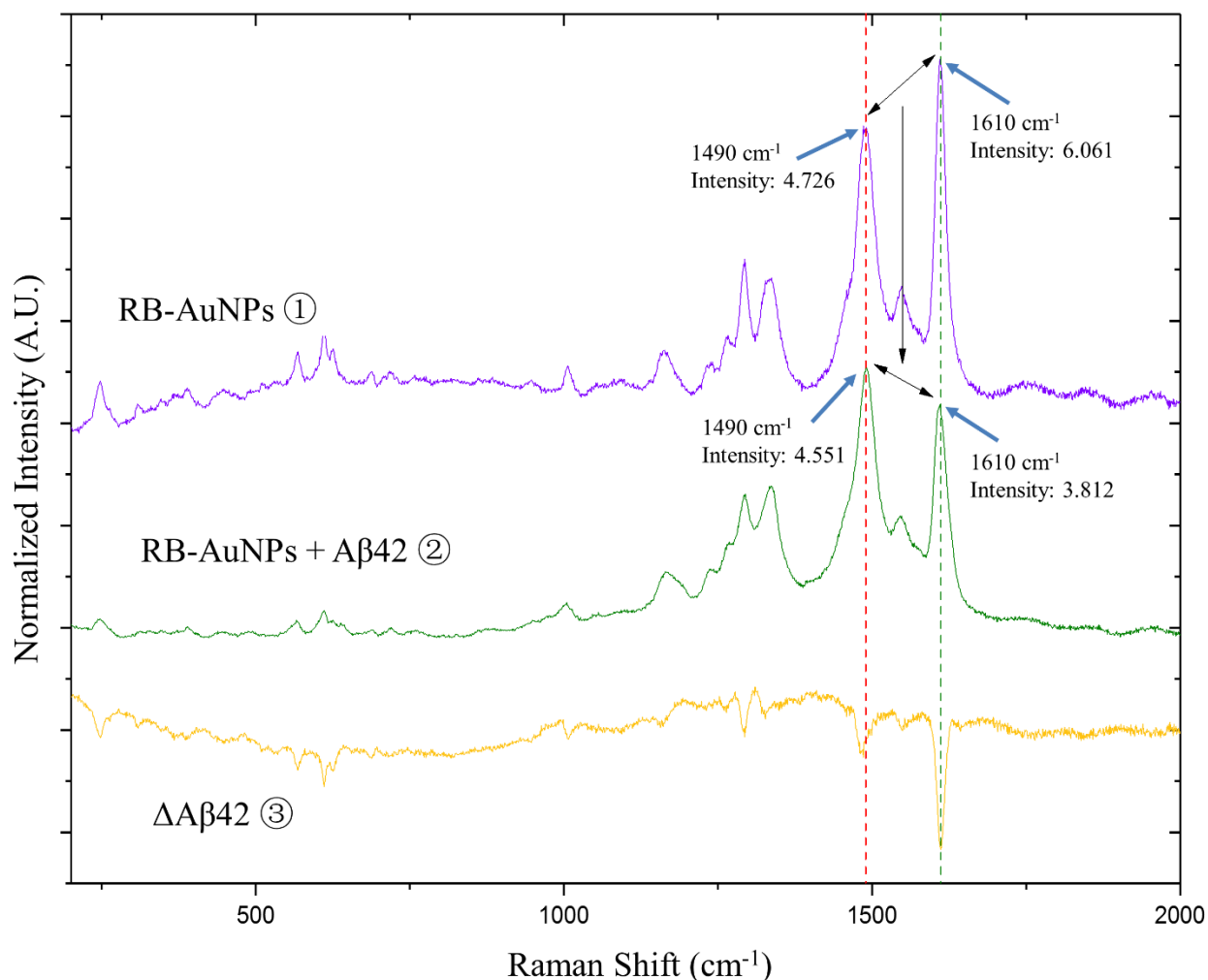


Figure 3.10 A β 42 induced spectral changes of RB-AuNPs. The normalized Raman spectra of the RB-AuNPs before (violet) and after (green) the addition of A β 42 peptides (2 μ M) show a considerable change in the relative magnitude of the signals from the two major peaks. The orange curve is obtained by digital subtraction of the (RB-AuNPs) spectrum from the (RB-AuNPs + A β 42) spectrum ($\textcircled{3} = \textcircled{2} - \textcircled{1}$).

The potential of the RB-AuNPs as SERS probes for amyloid detection was tested by exposing RB-AuNPs at different concentrations of A β 42 peptides. The normalized Raman spectra of RB-AuNPs before and after the addition of 2 μ M of A β 42 peptides are demonstrated in Figure 3.10. The spectrum changes caused by the A β 42 peptides (Δ A β 42) can be fully revealed by digitally

subtracting the original RB-AuNPs spectrum. The resulting $\Delta A\beta 42$ spectrum shows that the most significant changes took place in the two major peaks in 1490 cm^{-1} and 1610 cm^{-1} . These changes are associated with the mechanical deformation of RB aromatic rings sandwiched between the AuNPs and absorbed $A\beta 42$ peptides [100, 229]. The relative signal intensity in 1610 cm^{-1} underwent a much larger decrease compared to the signal in 1490 cm^{-1} . Consequently, the relative peak strength between 1490 cm^{-1} and 1610 cm^{-1} was changed. The highest peak in the original RB-AuNPs spectrum locates at 1610 cm^{-1} and the peak at 1490 cm^{-1} is slightly lower. After exposing to $A\beta 42$ peptides, the peak at 1490 cm^{-1} becomes the highest one. The ratio between the two peaks R_{peak} (intensity at 1490 cm^{-1} /intensity at 1610 cm^{-1}) changed from 0.780 (for RB-AuNPs) to 1.194 (for RB-AuNPs + $A\beta 42$).

To evaluate the quantitative correlation between the concentration of $A\beta 42$ peptides and the spectral changes, Raman spectra were measured for RB-AuNPs mixed with different concentrations of $A\beta 42$ peptides. For each concentration, 100 different spots were measured and the average R_{peak} values were plotted against the concentration of $A\beta 42$ peptides (Figure 3.11). The R_{peak} value and $A\beta 42$ concentration show a clear linear correlation ($r^2 = 0.9739$). The change in the R_{peak} values become significant when the added $A\beta 42$ concentration is greater than $1\text{ }\mu\text{M}$. The significance of the changes in R is determined by Student's t-test (t-test for short) [230]. The t-test is a statistical hypothesis test that can determine if one set of data is significantly different from another. In biomedical research, the result of the t-test is normally represented by p-values. When comparing two sets of experimental data, a null hypothesis can be made claiming that the difference between these two sets of data is purely due to the random errors in the data acquisition process. The possibility of such a null hypothesis to be true is quantified by the p-value. Therefore, the smaller the p-value, the more significant is the difference since this difference is more likely

to be induced by a non-random factor. Generally, the difference is considered as ‘significant’ when the p-value is less than 0.05 and as ‘very significant’ when the p-value is less than 0.01 [231]. The present thesis adopts these criteria for statistic comparison.

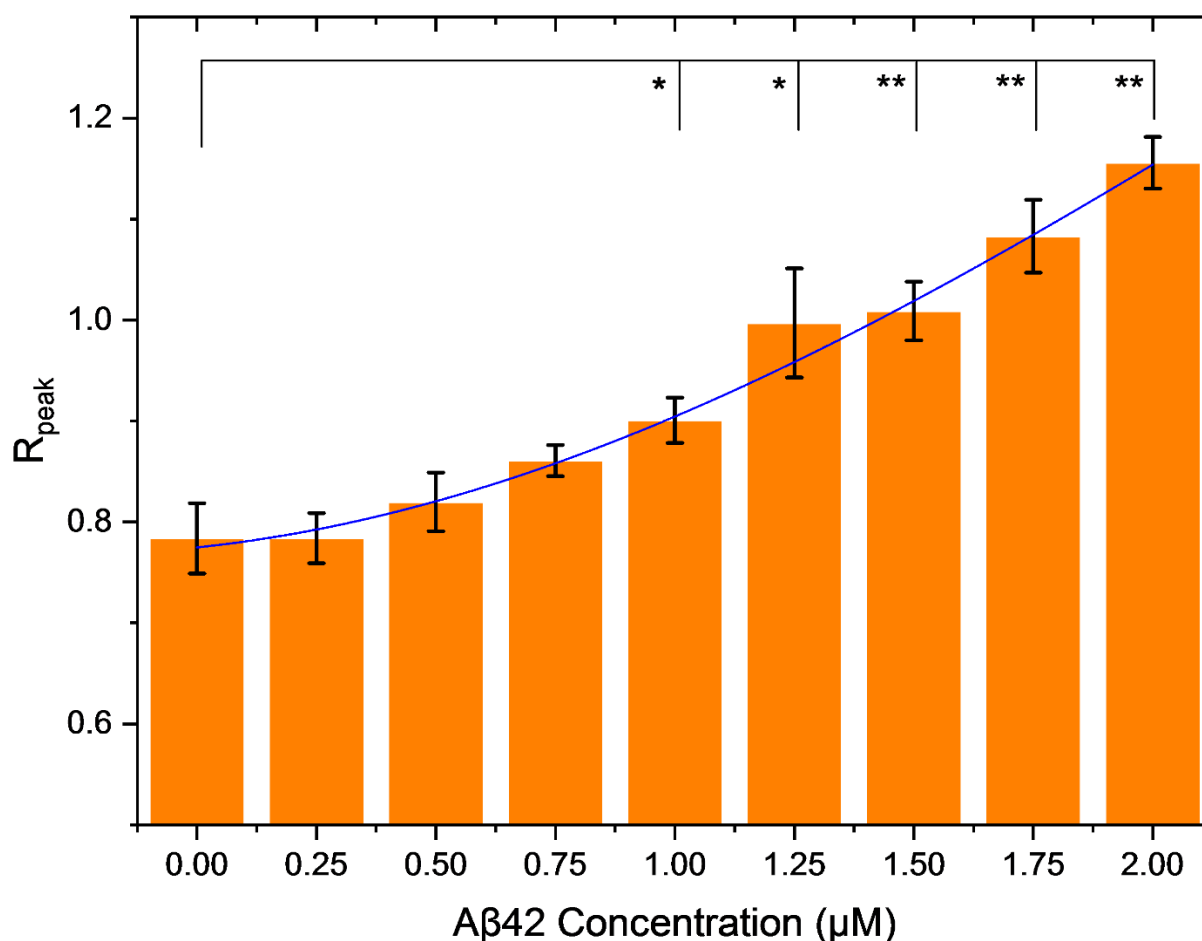


Figure 3.11 The relationship between R_{peak} and $A\beta_{42}$ concentration. The R_{peak} value is plotted against $A\beta_{42}$ concentration (0, 0.25, 0.5, 0.75, 1, 1.25, 1.5, 1.75, 2 μM). The blue curve represents the Gaussian fitting with $R^2 = 0.99532$. Statistical comparisons were carried out based on the Student's t-test. P values < 0.05 (*) or 0.01 (**) were considered significant.

3.8. Amyloid Detection in Transgenic Mice Brain Slices

Apart from soluble amyloid detection, RB-AuNPs were also used for amyloid detection in mice brains slices. The transgenic mouse model used in this study is a generic humanized animal model

for AD research. This model was developed by Oddo et al. in 2003 [58]. The 3xTg mice show age-dependent amyloid progression. Previous studies have detected apparent extracellular amyloid plaques in the mice's frontal cortex after 6 months of age [41, 58]. Figure 3.12a shows the confocal images of mouse brains stained separately with ThT or RB-AuNPs. For both types of stained brain slices, only weak emissions were detected in the control and young-aged (3 and 6 months) brains. At 7 months of age, plaques become visible, and more plaques were detected in 9 months old brains. Figure 3.12b shows the z-stack images of 9 months old brain slices stained with both ThT and RB-AuNPs. The 2D scatter plot of the fluorescence from ThT and RB-AuNPs shows a partially co-localization relationship with a Pearson's correlation coefficient (PCC) equals to 0.6403. The PCC is a coefficient that quantifies the linear correlation between two variables. It is calculated by dividing the covariance of the two variables by the product of their standard deviations. The value of PCC ranges from -1 to +1. Two variables are total positively correlated when PCC is +1 and totally negatively correlated when PCC is -1. It needs to be pointed out that the RB-AuNPs fluorescence has a higher degree of co-occurrence: the Manders coefficient of RB-AuNPs fluorescence $MC_R = 93.62\%$. The Manders coefficient measures the coincidence of signals from one channel with respect to signals from another channel. It is calculated by dividing the total intensities of coincided pixels by the total intensities of all pixels [232]. A Manders coefficient of 93.62 % means that 93.62 % of the RB-AuNPs fluorescence coincided with the ThT fluorescence. On the other hand, a considerable amount of the ThT fluorescence was detected without accompanying RB-AuNPs fluorescence: The Manders coefficient of ThT fluorescence MC_T is 46.56%. The difference in the co-localization degree is due to the non-specific staining of ThT dyes, which leads to a lower signal-to-noise ratio.

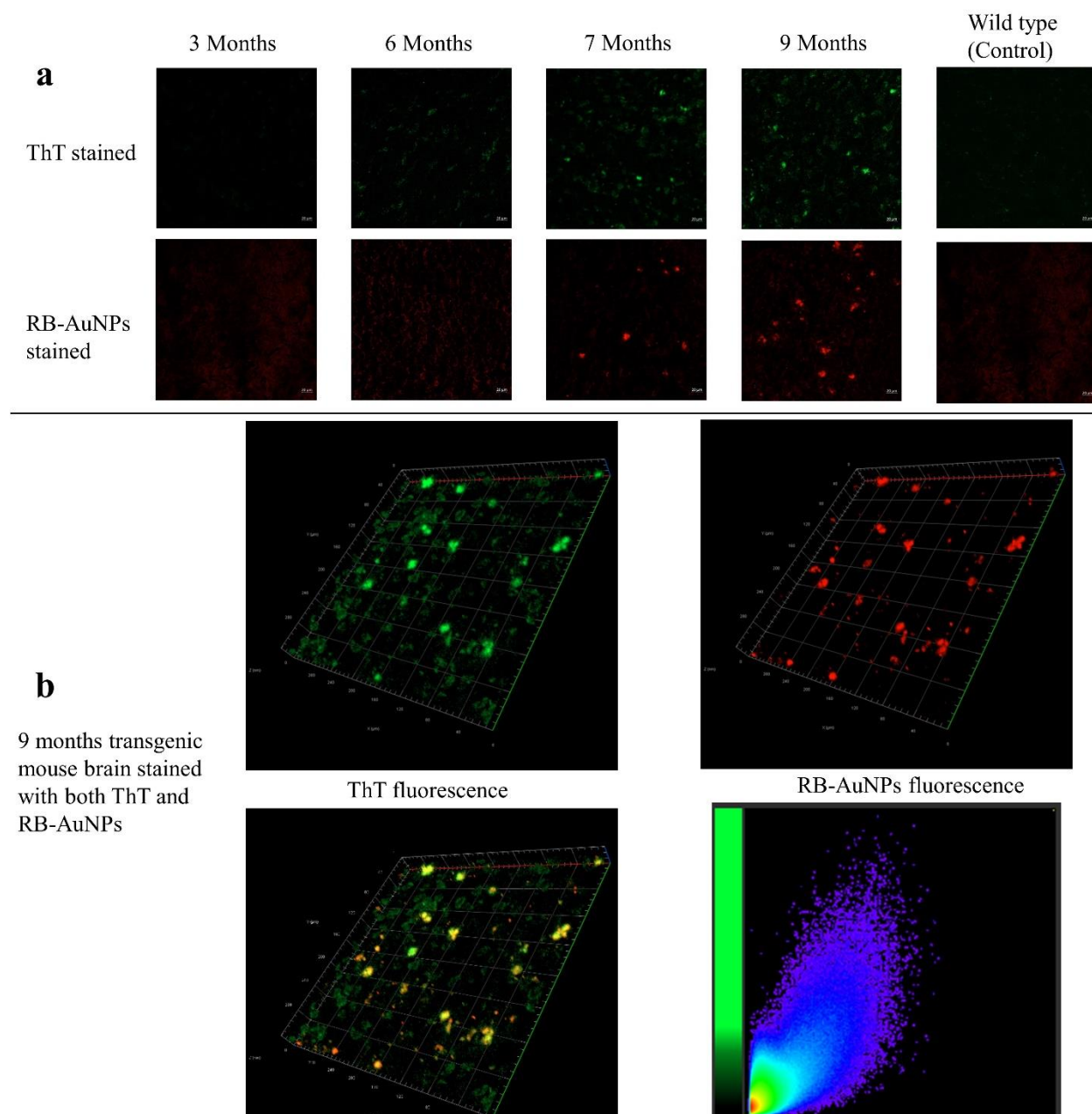


Figure 3.12 Confocal imaging of transgenic mouse brain slices. (a) Confocal images of transgenic mice brain slices in different ages, the brain slices were stained separately using ThT or RB-AuNPs. Brain slices from 9 months old wild type mice were used as control groups. (b) Confocal z-stack images of transgenic mice brain slice stained with both ThT and RB-AuNPs. The 2d scatter histogram was plotted by setting the intensities of RB-AuNPs as X-axis and the intensities of ThT as Y-axis.

Apart from fluorescence imaging, the RB-AuNPs stained mice brain slices were also investigated by Raman spectral imaging (Raman mapping). For each sample, 2700 measurement spots were taken and the size of each spot was $2.5 \times 2.5 \mu\text{m}^2$. After the measurement, the Raman mapping was generated based on a signal-to-baseline algorithm. Two spectral ranges were selected to generate the Raman mapping. The results were plotted at two spectral ranges which covers the two major peaks in the RB-AuNPs' Raman spectrum: 1470 cm^{-1} to 1510 cm^{-1} , covering the peak at 1490 cm^{-1} , and 1590 cm^{-1} to 1630 cm^{-1} , covering the peak at 1610 cm^{-1} . As we can see from Figure 3.13, the Raman images generated from both ranges did not show significant differences between the control (wild type mouse brain) and the experimental (transgenic mouse brain) groups. However, by highlighting the spots in which R_{peak} ($R_{\text{peak}} = \text{intensity at } 1490 \text{ cm}^{-1} \text{ divided by the intensity at } 1610 \text{ cm}^{-1}$) is greater than 1, an obvious difference was observed. The significantly increased density of highlighted spots is associated with the deposited amyloid plaques in the transgenic mouse brains.

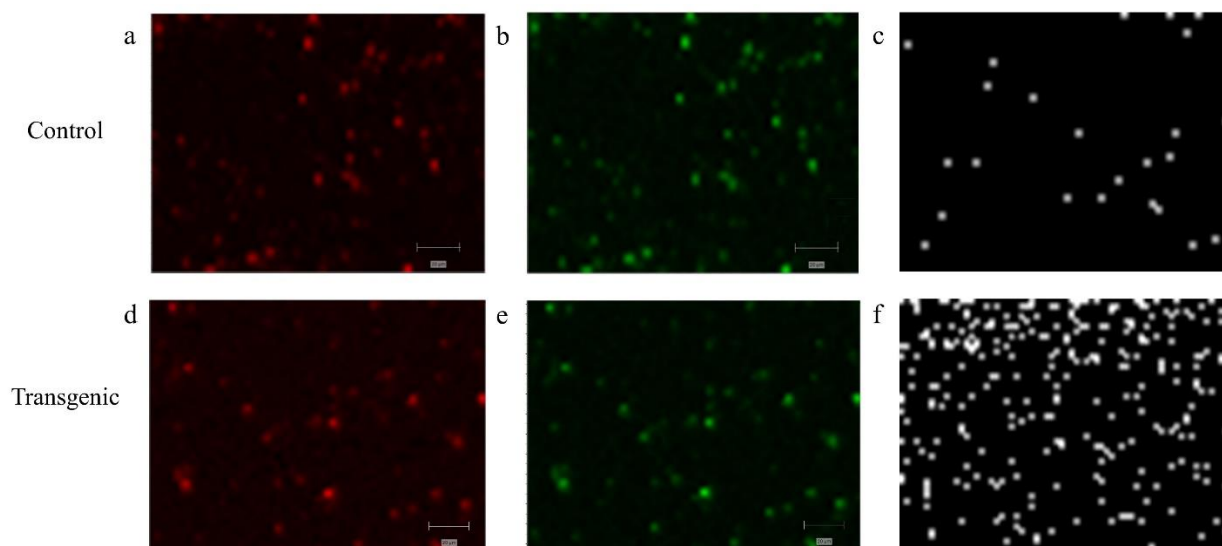


Figure 3.13 Raman mapping of mouse brains stained with RB-AuNPs. (a) and (d) Raman mappings (pseudo-color) plotted by calculating the signal to baseline area at the range of 1470 cm^{-1} to 1510 cm^{-1} for the control group (9-month wild-type mouse) and experimental group (9-month

transgenic mouse). (b) and (e) Mappings plotted by calculating the signal to baseline area at the range of 1590 cm^{-1} to 1630 cm^{-1} (signal to baseline area). (c) and (f) The highlighted spots in which the R_{peak} (intensity at 1490 cm^{-1} divided by the intensity at 1610 cm^{-1}) value is great than 1.

3.8. Summary

This chapter presented the preparation and application of RB conjugated gold nanoparticles as bifunctional nanoprobes for the detection of SERS-based A β 42 peptides and the fluorescence imaging of amyloid plaques. It was demonstrated that the Raman scattering of RB molecules is significantly enhanced when conjugated to AuNPs and the enhanced Raman spectrum found to exhibit detectable changes in the presence of amyloid peptides. In addition, it was also inferred that the interaction between A β 42 peptides and RB-AuNPs generate strongly enhanced fluorescence, which was sufficient for the labeling of amyloid plaques in mouse brain slices.

Fluorescence imaging using the RB-AuNPs revealed an age-dependent amyloid deposition, consistent with reported previous studies. The labelling specificity is also comparable with the commonly used amyloid dyes. Based on the various observations and illustrations made through this chapter, it can be concluded that a proof-of-concept study for the application of multifunctional nanoprobes is successfully carried out for the detection of amyloid. Based on this study, it is further envisaged that RB-AuNPs nanoparticles, which are successfully applied as inhibitors for amyloid aggregation, hold a great potential to be utilized as theranostic agents for amyloidosis in the near future.

The next chapter will discuss the application of C-dots as amyloid inhibitors. The C-dots were synthesized from microwave-assisted hydrothermal pyrolysis of sucrose. The bottom-up synthesis route is more facile than the previously reported top-down approaches. In addition, the usage of natural carbon sources ensures the biocompatibility of the C-dots. After synthesis and

characterization, the inhibition effect of C-dots with different passivation agents was carefully investigated.

Chapter 4: Carbon Dots based Amyloid Inhibitors

This chapter focuses on the application of C-dots as amyloid inhibitors. Two types of C-dots were synthesized through a bottom-up process, in which sucrose is hydrothermally pyrolyzed using microwave irradiation. Two types of passivation agents were added prior to the pyrolysis to generate PEG passivated C-dots (CD-G) and PEI passivated C-dots (CD-I). Inhibition assays where A β 42 peptides were incubated with CD-G or CD-I show that CD-G could promote A β 42 fibrillization while CD-I could inhibit it. Cell viability assays further revealed that both types of C-dots could effectively reduce the cytotoxicity of A β 42 peptides. The observed results suggest that passivation agents used in the synthesis of C-dots play a vital role in the interaction between C-dots and amyloid peptides. In addition, this study also shows that bottom-up synthesis holds a great potential as a facile and low-cost method for the preparation of C-dots-based amyloid inhibitors.

4.1. Introduction

As discussed in the literature review chapter, A β 42 peptides are playing a major role in the pathology of AD due to their faster aggregation rate and higher neurotoxicity. A β 42 contains two highly hydrophobic segments (16–20 amino acids and 30–40 amino acids), and a considerable amount of charged amino acid residues. In aqueous conditions, the hydrophobic and the electrostatic interactions lead to a rapid aggregation [233-235]. The aggregated A β 42 peptides first form soluble oligomers and then develop into mature fibrils and plaques. Owing to different degrees of polymerization, a variety of aggregation products are formed in the aggregation process and exhibit different levels of cytotoxicity. The alteration of amyloid aggregation is believed to be a promising therapy for AD and various nanoparticles have been used as amyloid inhibitors.

Carbon-based nanomaterials have emerged as promising candidates due to their high biocompatibility, ease of synthesis and high feasibility for further functionalization. Recently, Xu et al. reported the inhibition of A β 40 and A β 42 fibrillation using carbon dots (C-dots) [192]. However, the C-dots used in that study were prepared by top-down synthesis: the carbon source is carbon nanopowder that is peeled off from bulk graphite by laser ablation. In addition, the passivation of that C-dots is achieved by long-time reflux in the presence of strong acids. All the aforementioned factors have compromised the feasibility of the production and the batch-to-batch stability for C-dots.

To overcome the limitation of top-down synthesis, this chapter presents a bottom-up synthesis of C-dots using sucrose as the carbon source. For biomedical applications, the bottom-up strategy is considered as a more appropriated method due to its potential to achieve green and large-scale synthesis [236-238]. The C-dots synthesis was completed in a one-pot reaction in which sucrose was hydrothermally pyrolyzed under microwave irradiation. Two different passivation agents, PEG and PEI, were added prior to the pyrolysis to produce two types of C-dots: PEG passivated C-dots (CD-G) and PEI passivated C-dots (CD-I). Both types of C-dots showed excellent biocompatibility and can be readily taken up by neuronal cells. However, the two types of C-dots induced opposite effects on the aggregation process of A β 42. CD-I was capable of inhibiting the fibrillation of A β 42, while CD-G could accelerate the A β 42 aggregation. Interestingly, both types of C-dots can reduce the cytotoxicity of A β 42. These findings suggest that C-dots from a bottom-up synthesis can be used for the intervention of the amyloid aggregation process. Such an intervention holds a great potential in the development of new molecular therapies for AD.

4.2. Synthesis of C-dots

The overall process for the synthesis and purification of C-dots is illustrated in Figure 4.1. First, sucrose and a passivation agent were mixed and dissolved into a clear solution. Then the mixed solution was heated to 150 °C for 5 mins in a microwave hydrothermal reactor. After the pyrolysis reaction, the clear solution was transferred into a dark brown solution. To purify the generated C-dots, the brown solution was centrifuged in order to remove large deposits, followed by dialysis to remove unreacted small molecules. Dialysis is a process that can separate different solutes using a semi-permeable membrane. The dialysis membrane used in this experiment has a molecular weight cut-off (MWCO) equals 12 kDa. That means that small molecules with a molecular weight less than 12 kDa can readily pass the membrane, but larger particles such as the generated C-dots had to stay inside the dialysis tube. The efficacy of purification by a dialysis process is determined by the ratio between the volume of the liquid outside the dialysis tube (V_{out}) and the liquid inside the dialysis tube (V_{in}). Assume that the total concentration of un-reacted ingredients inside the dialysis tube is C_0 . When the mixed solution has completed one round of dialysis (the solution inside and outside the dialysis tube has reached equilibrium), the total concentration of un-reacted ingredients left inside the dialysis tube C_1 can be calculated by:

$$C_1 = C_0 V_{in} / (V_{in} + V_{out}) \quad \dots\dots\dots 4.1$$

Normally $V_{out} \gg V_{in}$, therefore, Formula 4.1 can be simplified as

$$C_1 = C_0 V_{in} / V_{out} \quad \dots\dots\dots 4.2$$

To further enhance the purification efficiency, the dialysis process was repeated for multiple times (n) by replacing the liquid outside the dialysis tube. The final concentration of remaining un-reacted ingredients C_n can be calculated by:

$$C_n = C_0 (V_{in} / V_{out})^n \quad \dots\dots\dots 4.3$$

In particular, the V_{in}/V_{out} in this study was set to be 1/200 (10 ml of the reacted solution against 2000 ml de-ionized water) and the dialysis was repeated for three times. Therefore, after the dialysis, the remaining un-reacted sucrose and passivation agents was reduced to $1.25 \times 10^{-9}\%$. Finally, the purified C-dots were lyophilized to remove the water solvent. Lyophilisation is a technique that can remove solvents at low temperature. The C-dots solutions were first frozen at $-80\text{ }^{\circ}\text{C}$ and then transferred into a lyophilizer inside which an ultra-high vacuum (10^{-7} pascal) was created. The temperature inside the lyophilizer was maintained at a low level ($<0\text{ }^{\circ}\text{C}$), but in such a low pressure, the heat is enough to sublime the solvent water and leave only the purified C-dots.

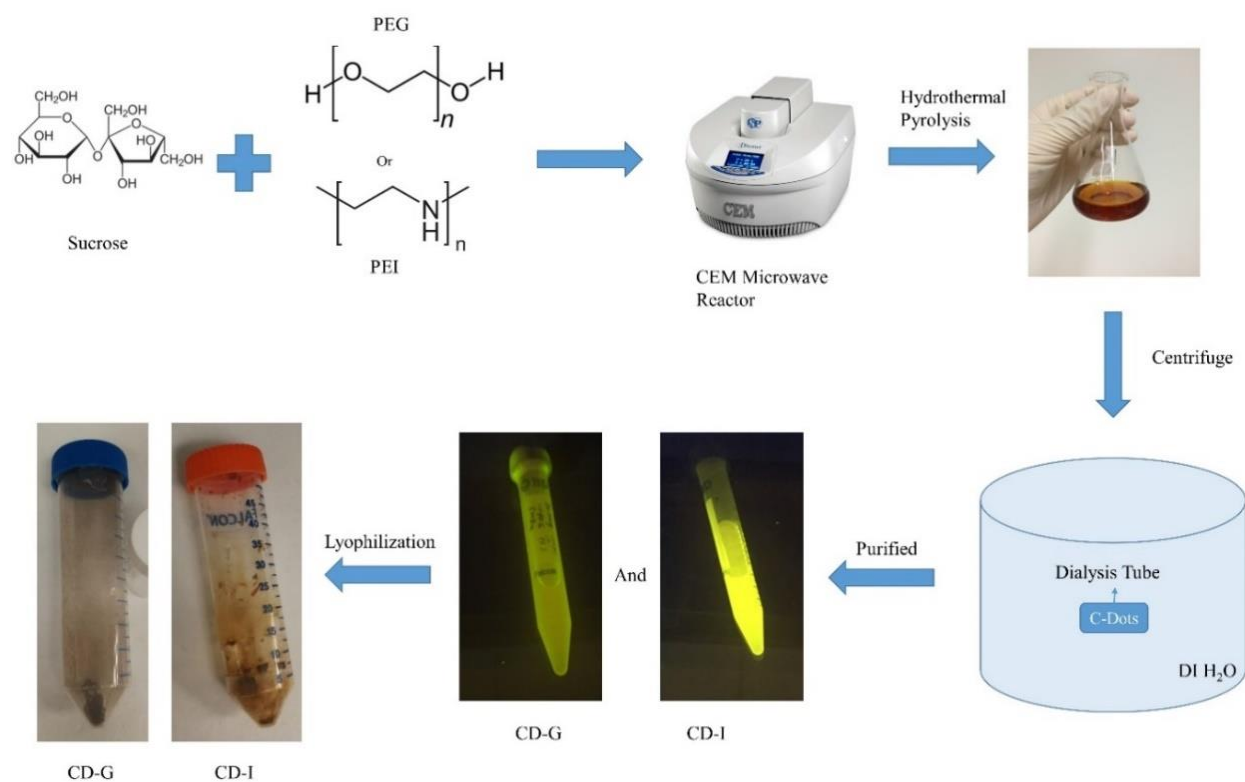


Figure 4.1 Scheme for the synthesis and purification of C-dots.

4.3. Characterization of C-dots

The size and morphology of the CD-G and CD-I were observed by TEM (Figures 4.2a and 4.2c). The size distribution histograms for CD-G and CD-I (Figures 4.2b and 4.2d) were plotted

by randomly measuring 100 particles for each. Both C-dots were well dispersed in aqueous condition. The average size of CD-G was found to be 6.45 ± 1.45 nm, whereas CD-I was slightly smaller with an average diameter of 4.16 ± 0.96 nm.

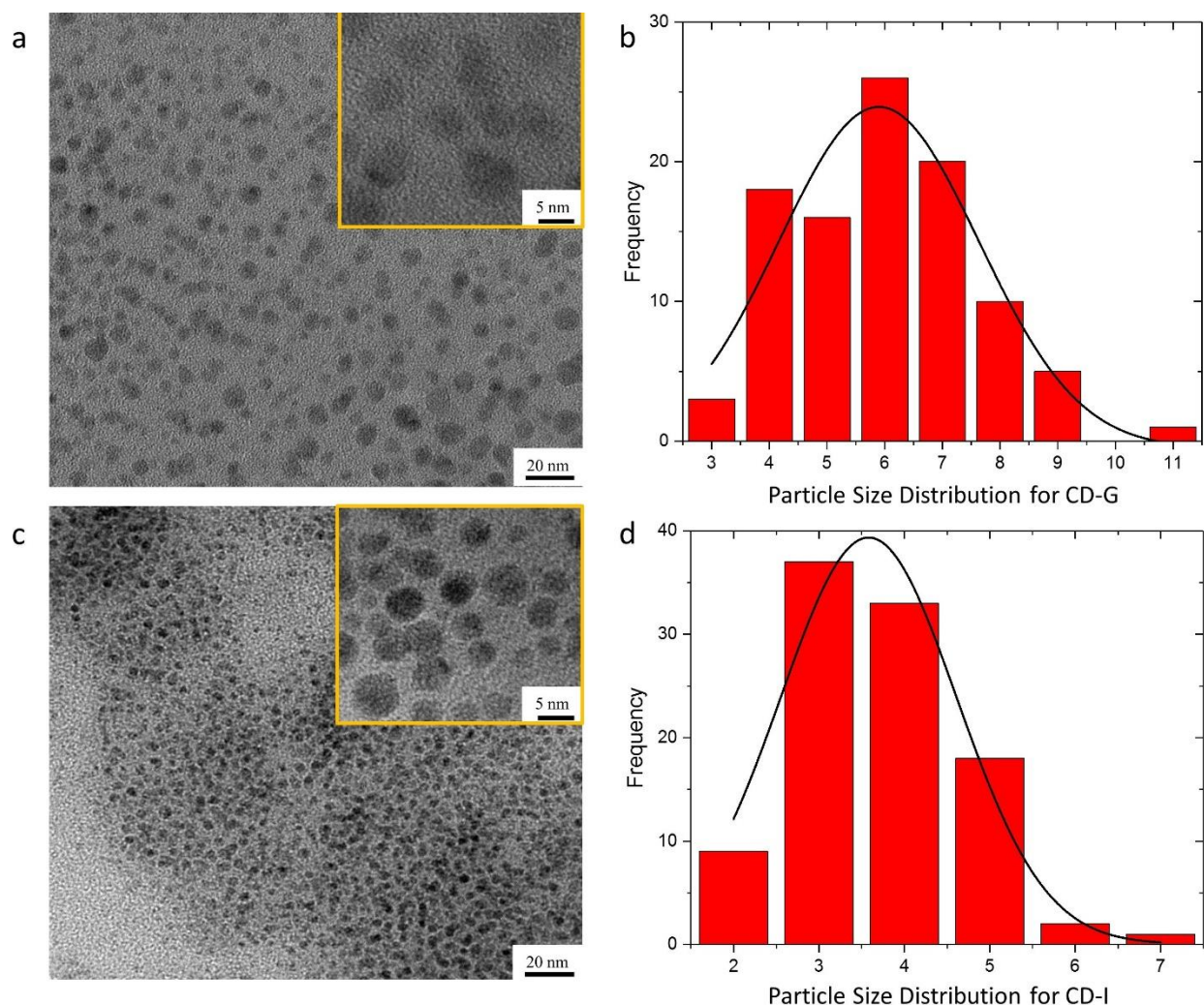


Figure 4.2 TEM images and size distribution of CD-G (a and b) and CD-I (c and d). The average size of CD-G is 6.45 ± 1.45 nm and that of CD-I is 4.16 ± 0.96 nm. The high resolution TEM images for CD-G and CD-I are inserted in a and c, respectively, outlined by the yellow box.

The UV-Vis absorption spectra and zeta potential of CD-I and CD-G are presented in Figure 4.3. Both C-dots exhibited very strong absorption in the short wavelength range. In PBS buffer (pH=7.4), CD-G could be considered as a neutral particle with a zeta potential of +1.02 mV. On

the other hand, due to positively charged nitrogen atoms in PEI molecules [239], CD-I is positively charged with a zeta potential of +22.5 mV.

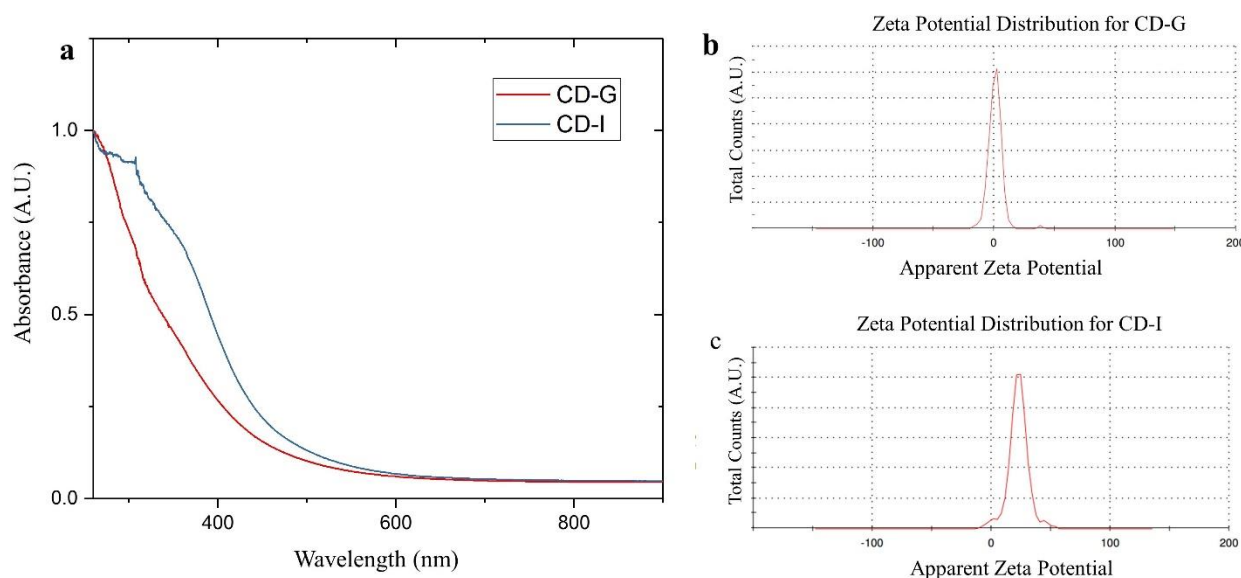


Figure 4.3 (a) UV-Vis spectra of CD-G and CD-I, and the zeta potential of CD-G (b), and CD-I (c).

Figure 4.4 shows the photoluminescence (PL) properties of CD-G and CD-I. A characteristic excitation-dependent emission of both C-dots was observed. From the PL spectra and the emission map of CD-G, maximum emission of CD-G was observed at 400 nm excitation/ 510 nm emission (Figures 4.4a and 4.4c), whereas the emission centre for CD-I was at longer wavelengths of 480 nm excitation/ 590 nm emission (Figures 4.4b and 4.4d). Both C-dots had a large Stoke's shift of 110 nm. For bioimaging applications, large Stoke's shift offers an advantage, since it can reduce self-quenching and errors produced by excitation backscattering [240]. In addition, CD-I showed detectable PL emission at the Vis-IR range, making it a suitable bio-imaging probe since the light absorbance and scattering of biological tissues are much weaker in Vis-IR range than the UV-Vis range [86].

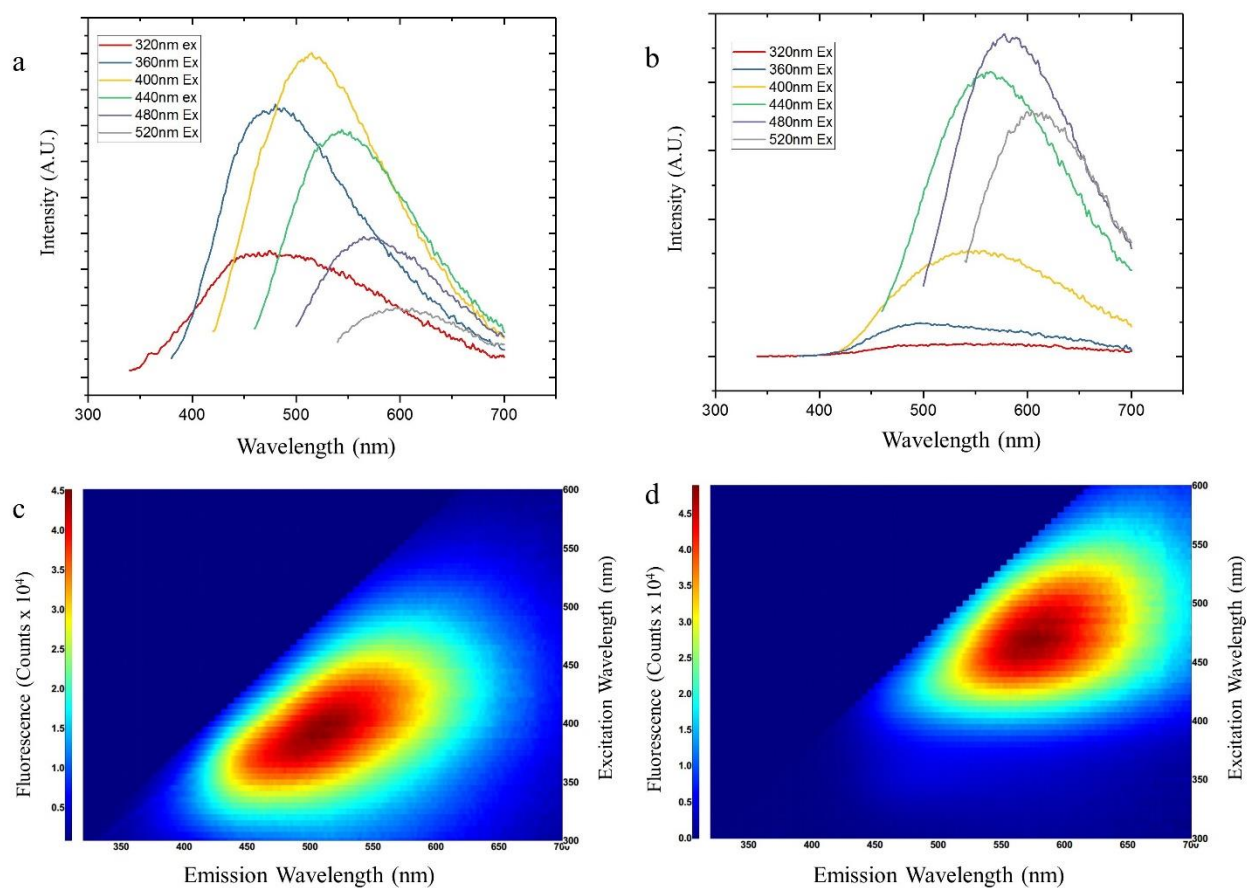


Figure 4.4 Fluorescence spectra and emission map of CD-G (a and c) and CD-I (b and d).

Maximum emission of CD-G was observed at 400 nm excitation / 510 nm emission. Maximum emission of CD-I was observed at 480 nm excitation / 590 nm emission.

4.4. Biocompatibility and Cellular Uptake of C-dots

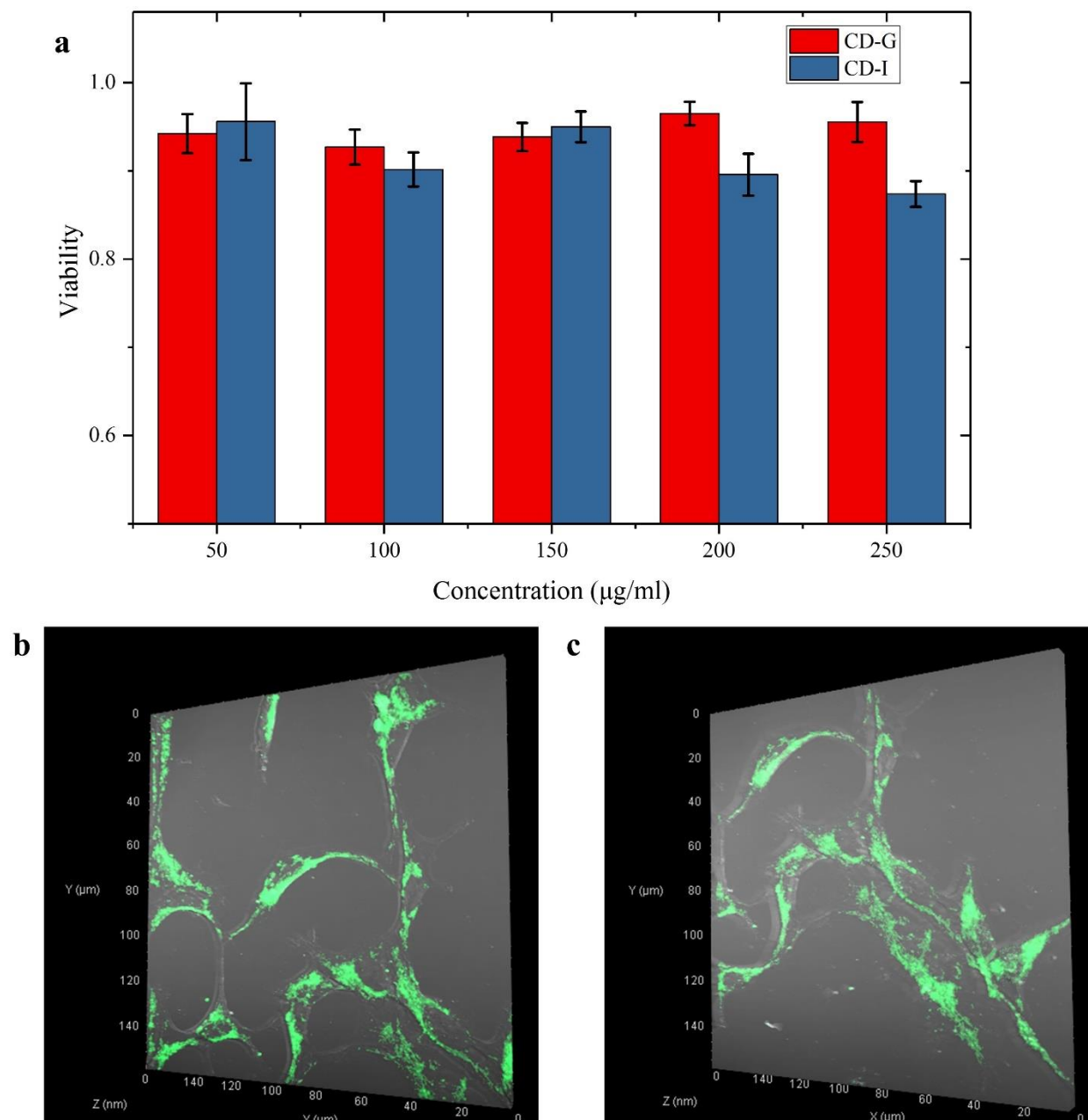


Figure 4.5 Biocompatibility and cellular uptake of C-dots. (a) Cell viability test (MTT) for CD-G and CD-I; and the confocal images (z-stack) of SHSY-5Y cells incubated with CD-G (b) and CD-I (c).

The biocompatibility of CD-G and CD-I was evaluated by MTT assay on SH-SY5Y neuroblastoma cells. SH-SY5Y cells were derived from a metastatic bone tumour and have been

widely used as *in vitro* models of neurodegenerative diseases [241, 242]. The viability measurements of SH-SY5Y cells after 24h incubation with CD-G and CD-I are shown in Figure 4.5a. The results demonstrated that even at very high concentrations of CD-G (250µg/ml), the viability of SH-SY5Y cells was greater than 90%, indicating the excellent biocompatibility of the compound. CD-I, on the other hand, showed a slightly higher cytotoxicity at high concentrations (200-250µg/ml). However, at lower concentrations (50-150µg/ml), the toxicity of CD-I is comparable with CD-G. Considering that for most biomedical applications the reported C-dots concentration used is less than 100 µg/ml, it is reasonable to conclude that both CD-G and CD-I are biocompatible nanoparticles. Confocal images of SH-SY5Y cells incubated with CD-G and CD-I are shown in Figure 4.5b and 4.5c. The cell morphology in both conditions remained intact and both types of C-dots could readily enter the cells. Although amyloid plaques are extracellular deposits, recent studies have found that intracellular amyloid peptides are also contributing to the pathogenesis of AD. Intracellular Aβ42 peptides have been found responsible for inducing neuronal apoptosis, and the build-up of intracellular amyloid is considered as an early event in the progression of AD [56]. Therefore, a good cellular uptake is desirable for nanomedicines which are targeting amyloid.

4.5. Alteration of the Aβ42 fibrillization process

The effect of C-dots on the Aβ42 fibrillization process was investigated by incubating Aβ42 with either CD-I or CD-G at 37°C for 24 hours. The kinetics of fibrillization was monitored by the ThT assay. ThT is a dye that specifically binds to the beta sheets of amyloid fibrils and the binding could enhance the quantum yield of ThT. Therefore, the kinetics of amyloid fibrillization is often monitored by measuring the fluorescence of added ThT [83]. Figure 4.6 shows the ThT assay in the presence or absence of CD-G/CD-I. The control group (Figure 4.6 - red curve), where the Aβ42

was incubated without C-dots, showed a typical three-stage process: the lag phase (from 0h to 4h), the elongation phase (from 4h to 20h) and the steady phase (from 20h onward). In the lag phase, A β 42 monomers aggregated into small clusters. There were a few beta-sheet structures in the small clusters and therefore the ThT fluorescence increased slowly. In the elongation phase, the quantity of A β 42 clusters was enough to serve as nuclei that quickly developed into fibrils by further absorption of monomers and small oligomers. The fast growth of fibrils is represented by the rapid increase of the ThT fluorescence. In the final steady phase, most of the A β 42 peptides were already aggregated, and therefore the fibrillization process ended, represented by a plateau in the ThT fluorescence curve. In the presence C-dots however, the A β 42 showed an altered fibrillization process. When incubated with CD-G, there was no apparent lag phase, the fibrillization started almost immediately after incubation and reached a steady phase earlier than the control group (Figure 4.6 - blue curve). On the other hand, when incubated with CD-I, the lag phase of A β 42 fibrillization was similar to that of the control group, but fibril growth was much slower in the elongation phase (Figure 4.6 - yellow curve).

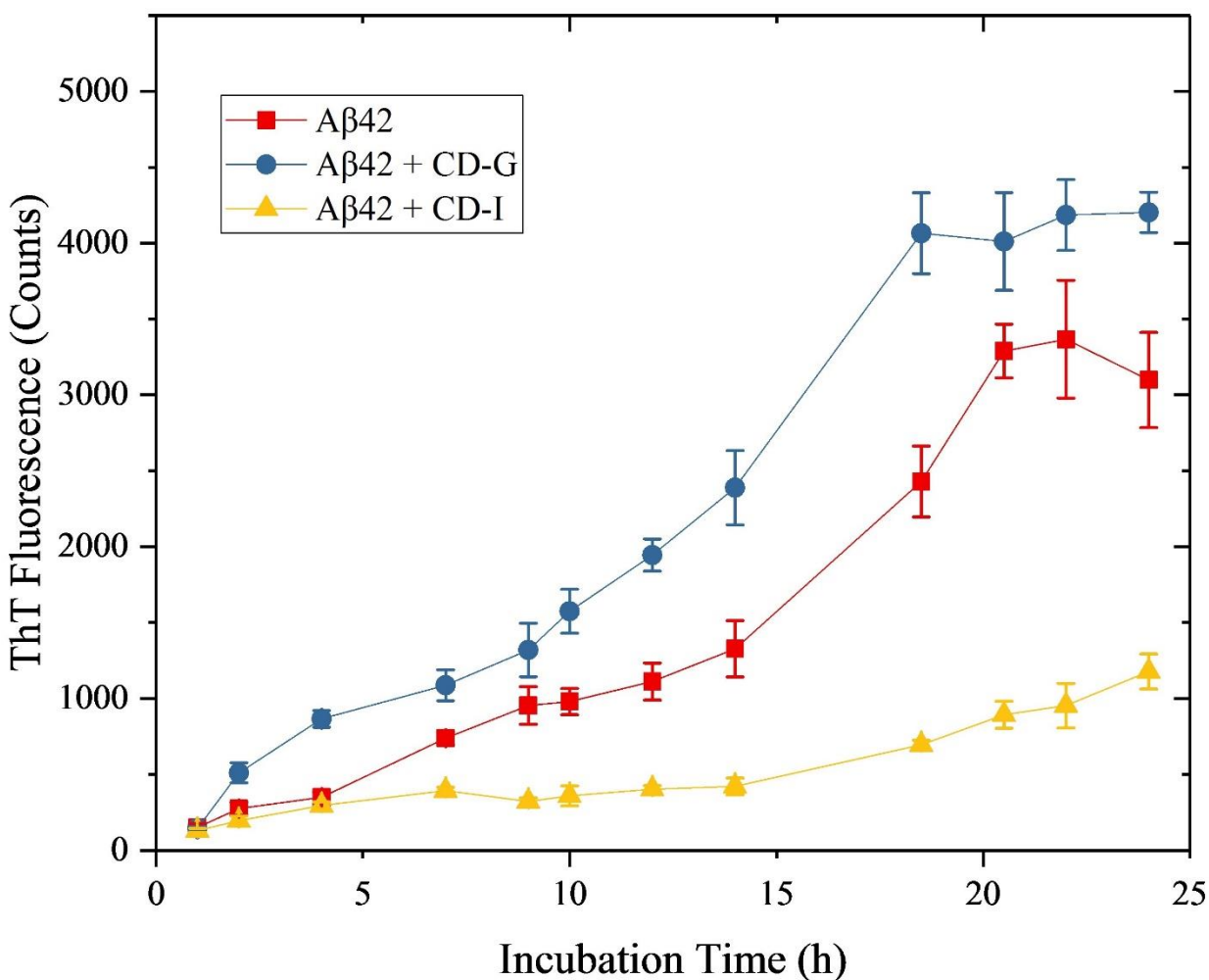


Figure 4.6 ThT assay of 20 μ M A β 42 peptides when incubated with/without C-dots.

TEM images of the amyloid fibrils, generated with different conditions, are consistent with the ThT assay results (Figure 4.7). Figure 4.7a shows the morphology of the amyloid fibrils after 24h incubation of A β 42 peptides alone. Figure 4.7b shows the morphology of A β 42 fibrils when incubated with CD-G. The fibrils are denser and thicker than those of the control groups. Figure 4.7c shows the morphology of A β 42 aggregates when incubated with CD-I. No mature fibrils were observed and, instead, only amorphous clusters were detected.

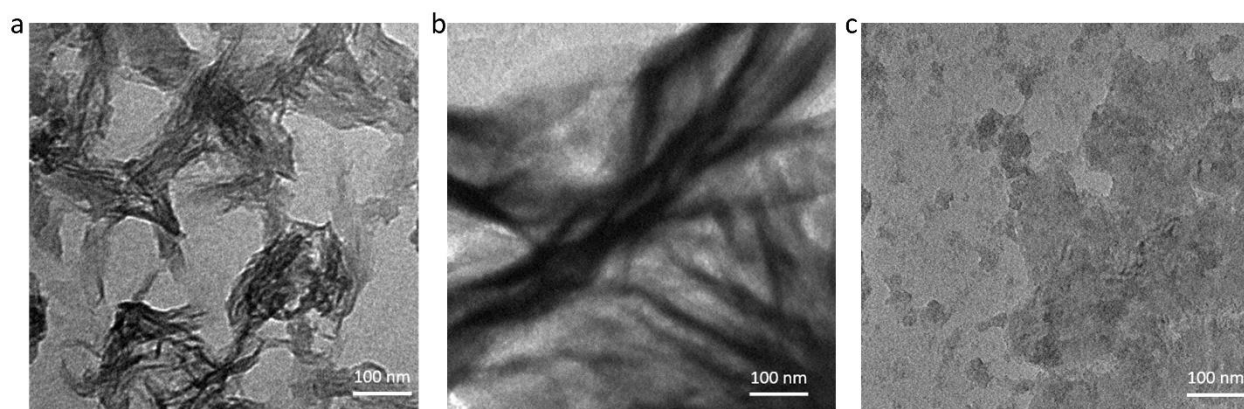


Figure 4.7 TEM images of amyloid fibrils after 24 hours incubation. (a) A β 42 incubated alone; (b) A β 42 incubated with CD-G and (c) A β 42 incubated with CD-I.

The reason for the different fibrillization behaviours of A β 42 in the presence of CD-G or CD-I could be attributed to the surface coating and the surface charge of the two C-dots (Figure 4.8). PEGylated nanoparticles have been found capable of altering amyloid fibrillization. Depending on the particle's size, charge and hydrophobicity, the fibrillization process could either be retarded or accelerated [243-245]. For CD-G, the PEG chains at the surface of the particles acted as sieves that captured the free A β 42 peptide monomers. By doing so, the local concentrations of A β 42 in the vicinity of CD-G dramatically increased which consequently triggered faster aggregation. Since CD-G is non-charged particles, the sieving is achieved by Van der Waals force, which is not strong enough to affect the elongation phase. Meanwhile, for CD-I, the surface charge plays an important role in the intervention of A β 42 fibrillization process. Previous studies have found that electrostatic interactions are a major contributing force in the elongation phase and charged particles could inhibit the fibrillization process by affecting these electrostatic interactions [184-186]. However, there are controversial studies about how the electrical properties affect the amyloid aggregation process. Some studies suggest that positively charged particles exhibit greater inhibition of amyloid fibrillization. This could be explained by the tight binding between the

positively charged particles and the A β peptides that carry a net negative charge [185, 189, 190]. Other studies indicate that negatively charged particles could achieve more efficient inhibition than positively charged ones [186, 188]. One possible explanation for these contradictory observations is that the inhibition effect is a result of synergy from the particle's polarity, size, hydrophobicity and particle/peptide ratio. Therefore, polarity alone doesn't determine whether a particle would accelerate or inhibit the amyloid fibrillization. Recent studies suggest that the surface charge density of particles, instead of particle polarity, is more likely to be the defining factor for the inhibition efficiency [187, 191]. The surface charge density is proportional to the particle's zeta potential and inversely proportional to the size of particles [246]. Therefore, although the zeta potential of CD-I is not very large (+22.5 mV), the small size of CD-I (~4.16 nm) gives a high surface charge density to CD-I, consequently leading to an effective inhibition of A β 42 fibrillization.

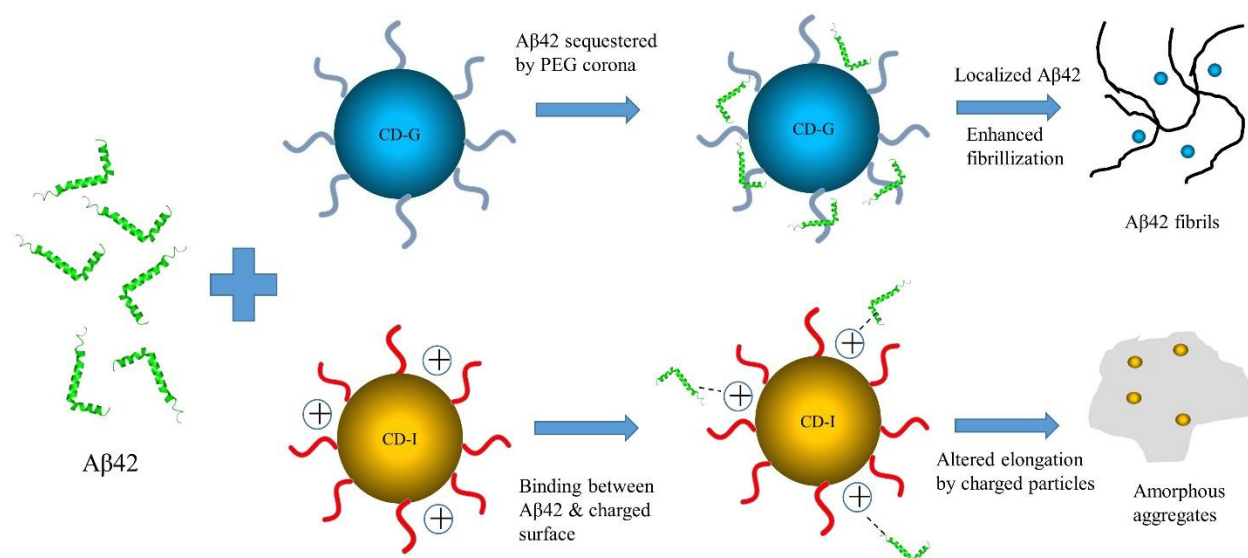


Figure 4.8 Schematic illustration of the interaction between A β 42 and C-dots. In the presence of CD-G, the PEG corona of CD-G could capture the A β 42 monomers, causing locally increased A β 42 concentration, and consequently lead to an enhanced fibrillization. In the presence of CD-I, the charged particles could affect the elongation phase of A β 42 fibrillization, leading to an amorphous aggregate of A β 42.

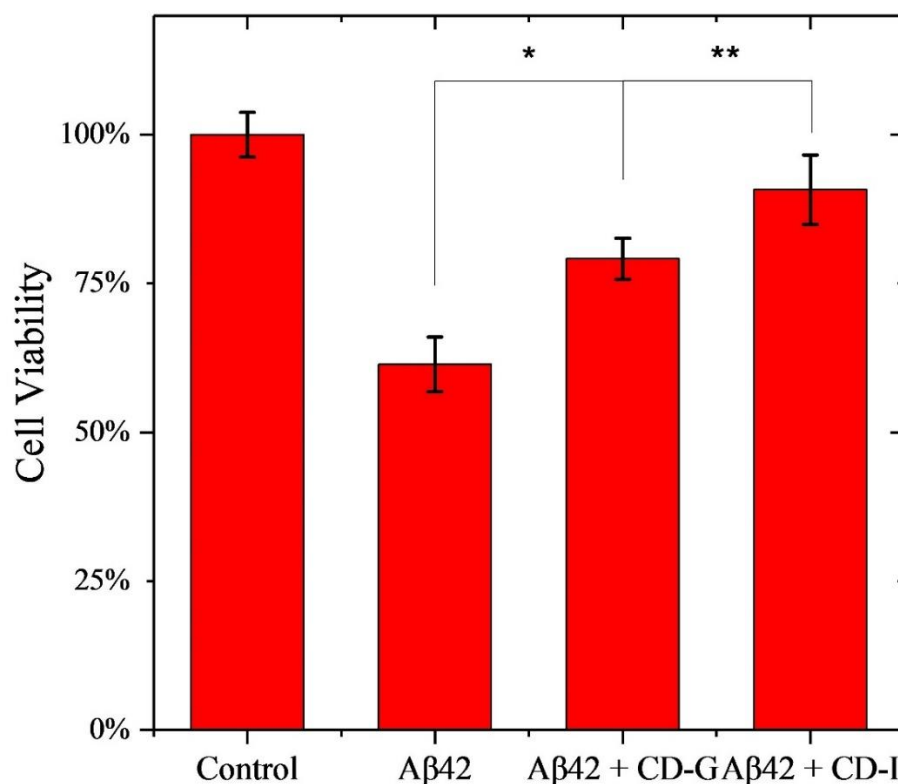


Figure 4.9 Mitigation of A β 42 toxicity. The cell viability of SH-SY5Y cells after 24 hours of incubation with A β 42 was measured. The addition of CD-G and CD-I at the beginning of incubation could reduce the cytotoxicity of A β 42.

To test how CD-G and CD-I affect the cytotoxicity of A β 42, SH-SY5Y cells were incubated together with A β 42 and CD-G/CD-I. The viability of the SH-SY5Y cells was measured by MTT assay and the results are listed in Figure 4.9. A β 42 alone exhibited a significant toxicity on neuroblastoma cells, causing a 40% reduction in cell viability. Interestingly, despite the opposite effect on the amyloid fibrillization, the addition of both CD-G and CD-I at the beginning of the incubation increased the cell viability up to 79.5% for CD-G and up to 91.3% for CD-I. The toxicity mitigation of CD-I is consistent with previous studies where it was shown to prevent the formation of toxic fibrils [39]. For CD-G, the accelerated fibrillization promoted the transformation of oligomers and protofibrils into mature fibrils, thereby reducing the cell's

exposure to A β 42 oligomers and protofibrils which are more toxic than the mature form of amyloid aggregates.

4.6. Summary

In summary, this chapter describes the preparation and utilization of C-dots-based amyloid inhibitors. Two types of C-dots, CD-G and CD-I, were synthesized through microwave-assisted pyrolysis of sucrose using PEG or PEI as passivation agents. The synthesis was completed by a facile, bottom-up method. Both types of C-dots have excellent biocompatibility and can readily enter neuronal cells. The interactions between A β 42 fibrillization and the two types of C-dots were investigated by ThT assay and TEM. CD-G could accelerate the fibrillization process of A β 42 and CD-I could inhibit it. When incubated with cells, both C-dots could successfully mitigate the toxicity effect induced by the A β 42 peptides. The results suggest that passivation agents play a vital role in the interaction between peptides and C-dots. This study also shows that bottom-up synthesis is a promising method to prepare C-dots-based amyloid inhibitors.

The subsequent chapter presents the enhanced targeting of SH-SY5Y cells by IONPs. This is achieved by conjugating dye-labelled A β 42 peptides with IONPs. The enhanced cellular uptake is attributed to the amyloid uptake capability of SH-SY5Y cells. As discussed in the literature review chapter, the cellular uptake of amyloid peptides is an important physiological event that takes place in the early stage of AD pathogenesis. Therefore, the A β 42 peptide-functionalized IONPs can be used as potential diagnostic tools for the early diagnosis of AD.

Chapter 5: Iron Oxide Nanoparticles for Specific Neuronal Cell

Targeting

This chapter describes the utilization of IONPs for the specific targeting of SH-SY5Y cells. The chapter begins with the description of the preparation of A β 42 functionalized IONPs (A β 42-IONPs). The A β 42 peptides were first labelled with Atto 647 dyes and then conjugated with amine-functionalized IONPs. Due to the pre-labeled Atto 647 dyes, the as-prepared A β 42-IONPs are magnetofluorescent. When incubated with SH-SY5Y cells, the cellular uptake of A β 42-IONPs was enhanced, compared to that of bare IONPs. Further, by labelling SH-SY5Y and HCT-116 cells, it was found that the A β 42-IONPs are selectively targeting the neuronal cells. This enhanced and specific neuronal targeting is attributed to the cellular uptake of extracellular amyloid by SH-SY5Y cells. In addition, the MR contrasting capability of the A β 42-IONPs is preserved after the peptides functionalization. The experimental results suggest that the A β 42 functionalized magnetofluorescent IONPs can be used as a bimodal probe to interrogate the cellular uptake of amyloid peptides.

5.1. Introduction

When it was originally reported, the amyloid cascade hypothesis claimed that the extracellular amyloid aggregates are the major pathological hallmarks, and the main toxicity generators in the pathogenesis, of AD. However, as it was soon found that for many AD patients, their disease progression did not correlate well with the aggregation of extracellular A β plaques. Further, many individuals who possess a considerable amount of amyloid deposits did not show cognitive decline [247]. These findings suggest that, apart from extracellular amyloid aggregates, other factors are also playing important roles in the progression of AD. The discovery of intracellular amyloid shed

a new light on the mechanism of AD pathogenesis. Animal studies on transgenic mice models suggest that the presence of intracellular amyloid is an early event in the progress of AD [41]. Intracellular amyloid is also correlated with synaptic dysfunction and cell death [56, 248]. Intracellular amyloid originates from two different sources. It can be produced by the proteolysis of APP in the membrane of intracellular organelles. Alternatively, extracellular amyloid can be taken up by neuronal cells to contribute to the intracellular amyloid pool. In addition, the cellular uptake of extracellular amyloid is linked with the spatiotemporal spreading of neuronal dysfunction. A β oligomers, produced in cells with overexpressed APP, can migrate to cells with lower quantity of APP and induce cell death [249]. The exact mechanism of this amyloid uptake is not fully understood. Most exogenous amyloid taken up by neuronal cells will colocalize with lysosomes and endosomes, suggesting that the endosomal-lysosomal pathway is most likely involved in the cellular uptake of amyloid [249]. The amyloid selectivity towards neuronal cells also suggests that this uptake is regulated by specific receptors [63].

Iron oxide nanoparticles (IONPs) have been widely employed in different biomedical applications including MR imaging [250], drug delivery [251, 252] and magnetic hyperthermia therapy [253]. To enhance the specificity of IONPs, biorecognition targeting ligands, such as antibodies, peptides, and aptamers, can be conjugated to the nanoparticles [132]. Among these ligands, peptides are particularly well investigated due to their low molecular weight, ease to synthesize and generally non-immunogenic nature [254]. Those peptides could be classified into two types:

- a) Cell-penetrating peptides (CPP), such as TAT peptides, that enhance the cellular uptake by activating single or multiple endocytotic mechanisms [255].

- b) Cell-targeting peptides (CTP), such as RGD peptides, that target a certain cell by binding to receptors which are upregulated in the target cells [256].

In the experiments presented in this chapter, A β 42 peptides were utilized as CTPs to facilitate the neuro-targeting of IONPs. By conjugating dye-labeled A β 42 peptides with amine-functionalized IONPs, magneto-fluorescent IONPs were prepared and then used for selective labelling of SH-SY5Y neuroblastoma cells. The results suggest that A β 42 functionalized IONPs can be used as bifunctional nanoprobes for the interrogation of intracellular amyloid accumulation.

5.2. Labelling A β 42 with Atto 647 dye

Although MRI is capable of providing a lot of physiological information, it is still suffering from limitations, such as low sensitivity and long acquisition time [257]. In order to obtain more comprehensive biological information, multimodal IONPs can be prepared by integrating IONPs with additional contrast agents, including fluorescent dyes, Quantum Dots, and positron emitting isotopes [86]. In order to render the IONP into a fluorescent probe, prior to the peptide conjugation, the A β 42 peptides were first labelled with Atto 647 dye. As shown in Figure 5.1, the Atto 647 dye is available in the form of NHS ester. At mild pH condition (PBS buffer, pH=7.4), the NHS ester can rapidly react with the primary amine groups in the A β 42 peptides and form stable amide bonds. After conjugation, the conjugated Atto647-A β 42 was purified using size exclusive chromatography (SEC). SEC is a chromatographic technique that can separate mixed materials based on their size. For Atto647 and A β 42, the size difference is reflected by the distinct molecular weight (843 g/mol for Atto647 and 4514.1 g/mol for A β 42). The SEC column is prepacked with porous gel. The unpurified Atto647-A β 42 was placed on the top of SEC column and then entered the SEC column under gravity effect. When the mixed conjugation products were traveling downward inside the column, the different molecules can enter the pores in the gel and then exit.

Based on their size, molecules spend different time periods inside the pores. Large molecules cannot enter the pores and therefore travel faster. Meanwhile, small molecules that can readily enter the pores stay much longer. By collecting different eluates under the SEC column, the Atto647-conjugated A β 42 can be separated from free Atto647. However, due to the small size difference between conjugated and unconjugated A β 42 peptides, SEC cannot remove the unconjugated A β 42 peptides. The separation is confirmed by measuring the fluorescence of eluates. As shown in Figure 5.2, ten eluates were collected after the SEC purification and each eluate has a volume of 1 ml. The numbering of the eluates represents the sequence of collection (eluate 1 is the first collected eluate and eluate 10 is the last collected eluate). Fluorescence was first detected in eluates 2 and 3, and this is attributed to the dye-labelled A β 42 peptides. Next, during the period in which eluates 4 to 7 were collected, the small Atto647 molecules were still travelling inside the column, and therefore the fluorescence intensities in eluates 4 to 7 are negligible. Finally, the free Atto647 exited from the bottom of SEC column, indicated by the strong fluorescence detected in eluates 8 and 9.

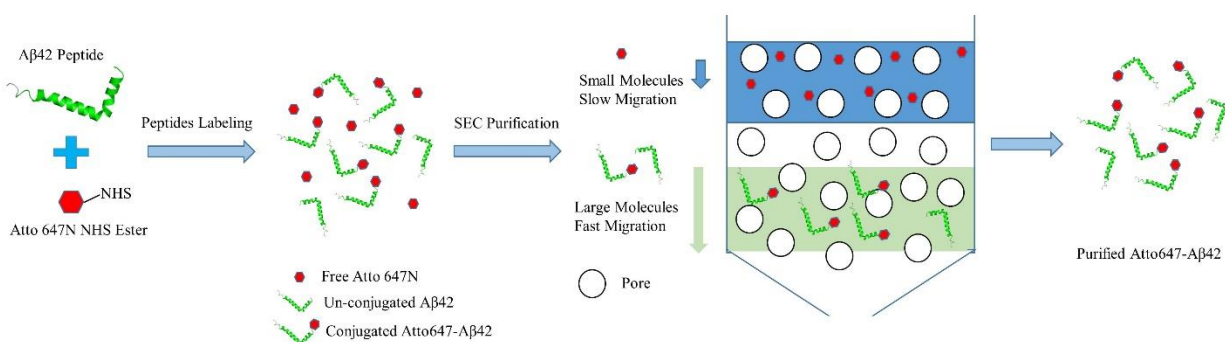


Figure 5.1 Scheme for the labelling and purification of A β 42 peptides.

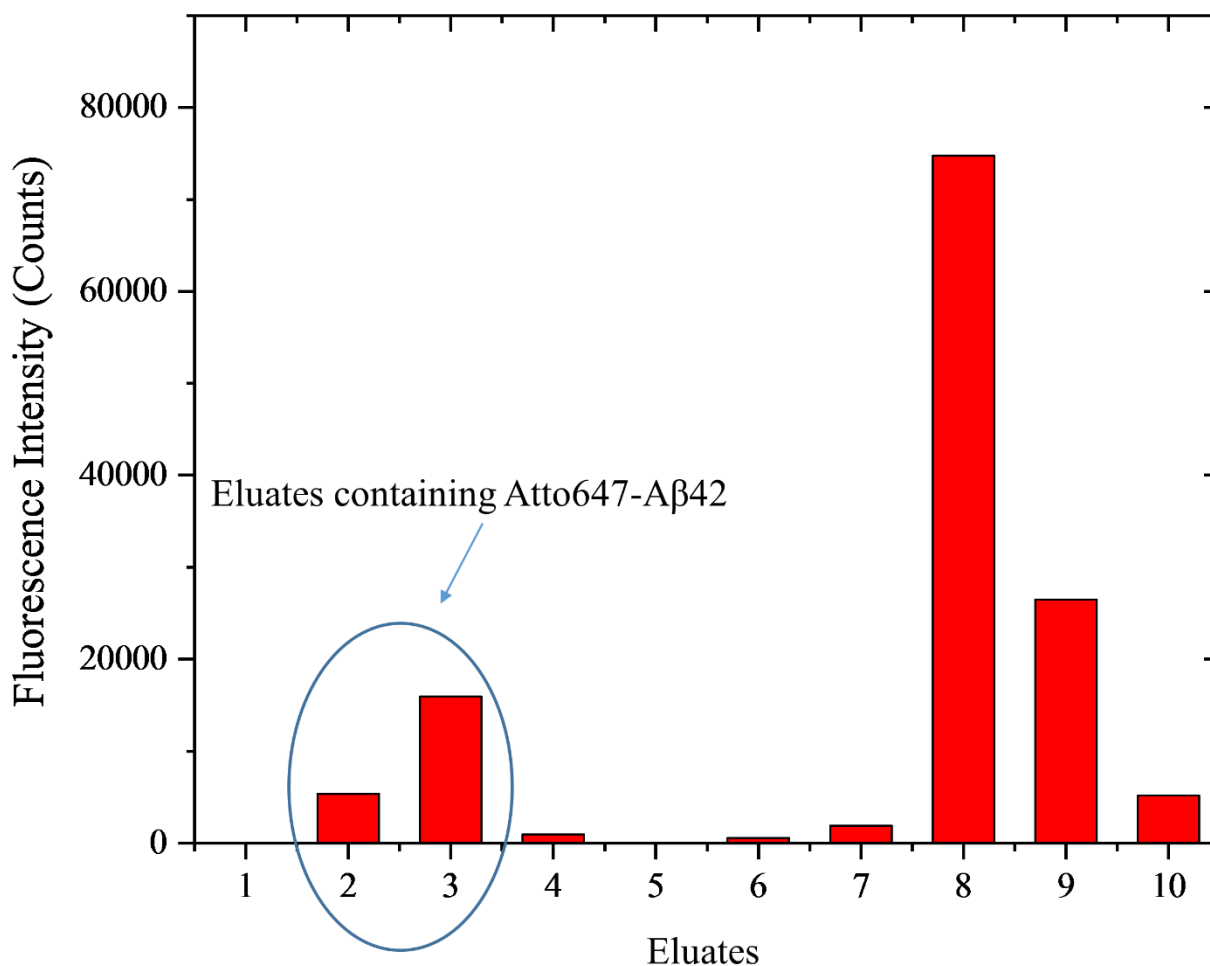


Figure 5.2 Fluorescence intensity for eluates after SEC purification. Fluorescence was first detected in eluates 2 and 3, attributed to the dye-labelled A β 42 peptides, which migrated faster due to their large molecular weight (refer to Figure 5.1). Fluorescence intensities in eluates 4 to 7 are very weak because Atto647 molecules were still travelling inside the column. The strong fluorescence in eluates 8 and 9 are caused by the free Atto647 that finally exited from the SEC column.

After the SEC purification, eluates 2 and 3, containing most of the Atto647-A β 42, were collected for further studies. The dye/peptide ratio (D/P) was calculated by the following formula:

$$D/P = A_{647} \times \epsilon_{A\beta 42} / [A_{280} - (A_{647} \times 0.05)] \times 150000 \quad \dots\dots\dots 5.1$$

A_{647} = Absorbance at 647 nm

A_{280} = Absorbance at 280 nm

$\epsilon_{A\beta 42} = 1450 \text{ cm}^{-1}\text{M}^{-1}$, the molar extinction coefficient of A β 42 at 280 nm [258].

The calculated D/P is 0.23. This relatively low D/P is due to the presence of un-conjugated A β 42.

5.3. Functionalization and Characterization of IONPs

After the labelling of peptides, the Atto647-A β 42 was then conjugated with amine-functionalized IONP through a one-step EDC/NHS reaction. The carboxylic groups of A β 42 peptides were activated by the EDC crosslinker and then reacted with the amine groups on the surface of IONPs. NHS was also added as a catalyst to enhance the conjugation efficiency. In order to prevent the self-crosslinking between A β 42 peptides, the peptides were mixed well with the IONPs before the addition of EDC/NHS solution. By doing so, most of the amine groups that reacted with the activated carboxylic groups would be those from the surface of IONPs. After the conjugation, the Atto647-A β 42-IONPs were also purified using SEC.

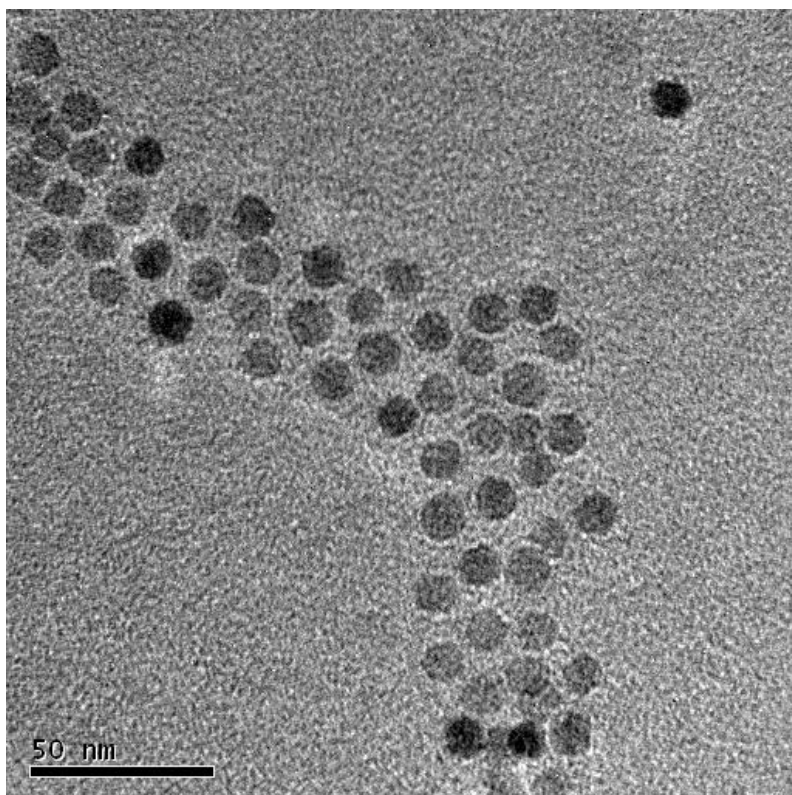


Figure 5.3 TEM image of Atto647-A β 42-IONPs. The average size of the IONPs is 15 nm.

The morphology of the Atto647-A β 42-IONPs was characterized by TEM. As shown in Figure 5.3, the average size of the IONPs is 15 nm and the water dispersity is not affected by the functionalization. Due to the low molecular weight of A β 42 peptides, the conjugated A β 42 peptides cannot be visualized in the TEM image.

The successful conjugation of Atto647-A β 42 was confirmed by changes in the hydrodynamic diameters of IONPs, measured by dynamic light scattering (DLS). As discussed in Chapter 3, those nanoparticles that are dispersed in solutions will be encapsulated by a bi-layer structure formed by the absorbed solvent molecules. The hydrodynamic diameter equals to the core size of nanoparticles plus the thickness of the solvent layer. DLS is an optical technique that can measure the hydrodynamic size of particles or large molecules. To conduct the DLS measurement, a monochromatic laser is used to illuminate the particle suspension. When the light travels across the suspension, the small particles will scatter the light to all directions, and the scattered photons will then be detected by detectors that are positions at either right angle (90°) or back angle (173°). Due to the continuous Brownian motion of particles, the relative distance between particles are constantly changing, leading to varying interference of the scattered light. This varying interference is reflected as fluctuating signals measured by the detector. Taking the advantage of autocorrelation, the hydrodynamic size information can be extracted from the recorded light intensity pattern. As shown in Figure 5.4, the hydrodynamic diameter of unconjugated IONPs is 16.4 nm, slightly larger than the core size. After the conjugation of A β 42, the solvent molecules were absorbed on top of the conjugated peptides, leading to an increased hydrodynamic diameter of 36.8 nm. This observed increase in the hydrodynamic diameters further proves the successful conjugation between A β 42 and IONPs.

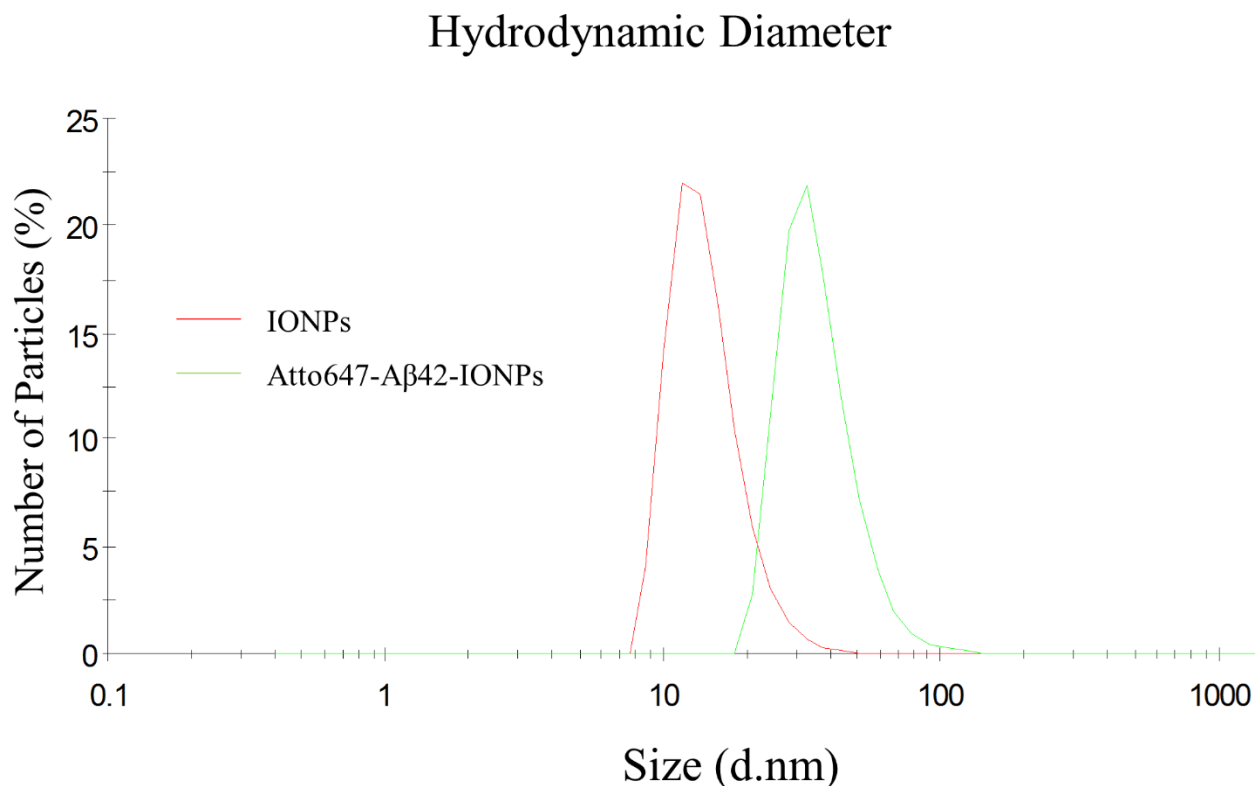


Figure 5.4 DLS measurement of IONPs and Atto647-Aβ42-IONPs. The x-axis is the hydrodynamic diameter and the y-axis is the number of particles (expressed in % of total number) with different hydrodynamic diameters. The hydrodynamic diameter of IONPs increased from 16.4 nm to 36.8 nm before and after the conjugation.

Apart from the hydrodynamic diameters, the appearance of fluorescence emission also proves the successful conjugation of dye-labelled peptides. As shown in Figure 5.5a, the original IONPs are non-fluorescent (blue curve). After conjugation, the fluorescence of Atto647 was not quenched (red curve). The emission map of Atto647-Aβ42-IONPs (Figure 5.5b) suggests that fluorescence emission of Atto647-Aβ42-IONPs becomes detectable when the excitation wavelength is longer than 600 nm and reached maximum under 646 nm excitation.

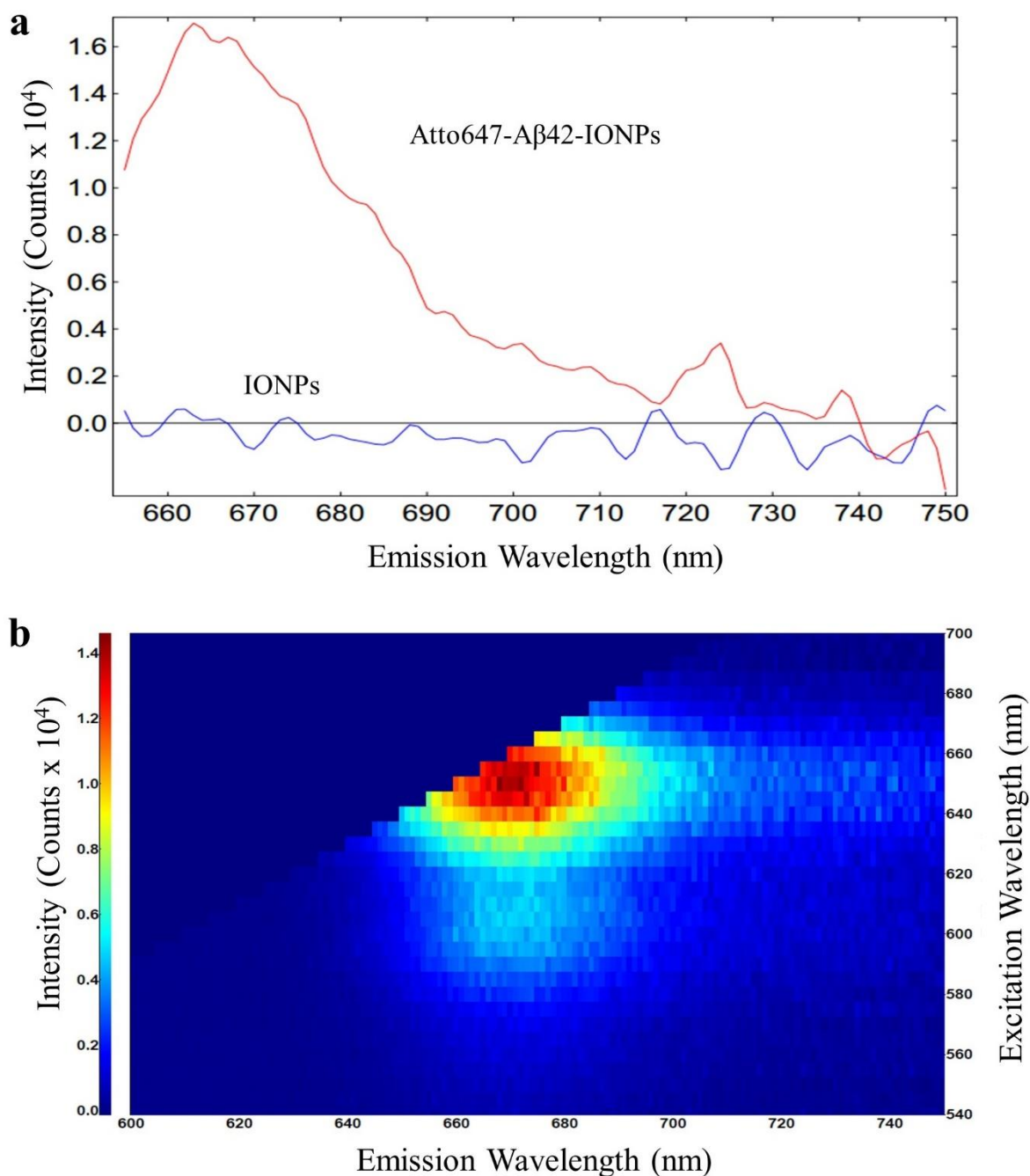


Figure 5.5 Optical characterization of IONPs. (a) Emission spectra of IONPs and Atto647-A β 42-IONPs under 646 nm excitation. (b) Emission map of Atto647-A β 42-IONPs.

The biocompatibility of the Atto647-A β 42-IONPs was tested by incubating the IONPs with SH-SY5Y neuroblastoma and HEK293 embryonic kidney cells. The results were illustrated in Figure 5.6. It was clear that Atto647-A β 42-IONPs exhibit low cytotoxicity towards both SH-SY5Y

and HEK293 cells. It is well known that A β 42 is toxic to neuronal cells such as SH-SY5Y cells [259]. In this study, the A β 42 peptides were conjugated to IONPs through stable covalent bonds, which prevented the generation of toxic species through A β 42 aggregation.

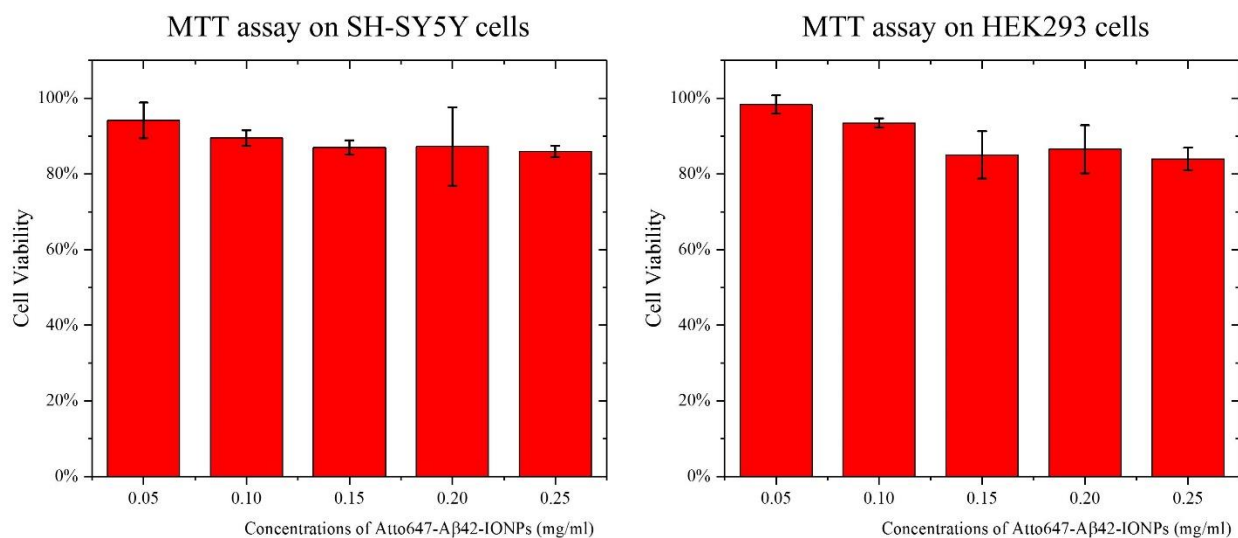


Figure 5.6 Cell viability assays for Atto647-A β 42-IONPs. The functionalized nanoparticles show low toxicity to both cells.

5.4. Specific Targeting to SH-SY5Y Cells

The enhanced uptake of Atto647-A β 42-IONPs by the SH-SY5Y cells was validated by comparing the cells' uptake of the Atto647-A β 42-IONPs with the original IONPs. SH-SY5Y cells were seeded in 6-well plate and then incubated with Atto647-A β 42-IONPs or unconjugated IONPs for 6 hours. After the incubation, the SH-SY5Y cells were stained using Prussian blue (PB) staining. As its name suggests, PB is a blue pigment that is produced from ferrous ferrocyanide salts. For histochemical applications, PB is widely used as a sensitive indicator to detect the presence of iron in cells and tissues. Before the staining, PB solution (4%) was mixed with an equal volume of HCl solution (4%). The HCl was used to break the protein-iron linkages in order to release free Fe ions. These free Fe ions can then combine with potassium ferrocyanide to form

ferric ferrocyanide, a highly insoluble blue pigments. Technically, PB refers to this blue pigments. Therefore the cells were actually stained by potassium ferrocyanide. However, due to historical reason, this staining operation is generally called PB staining. As shown in Figure 5.7, it is clear that the cells incubated with Atto647-A β 42-IONPs (Figure 5.7b) show much more blue pigments than those incubated with unfunctionalized IONPs (Figure 5.7a), suggesting an enhanced uptake of the Atto647-A β 42-IONPs by SH-SY5Y cells.

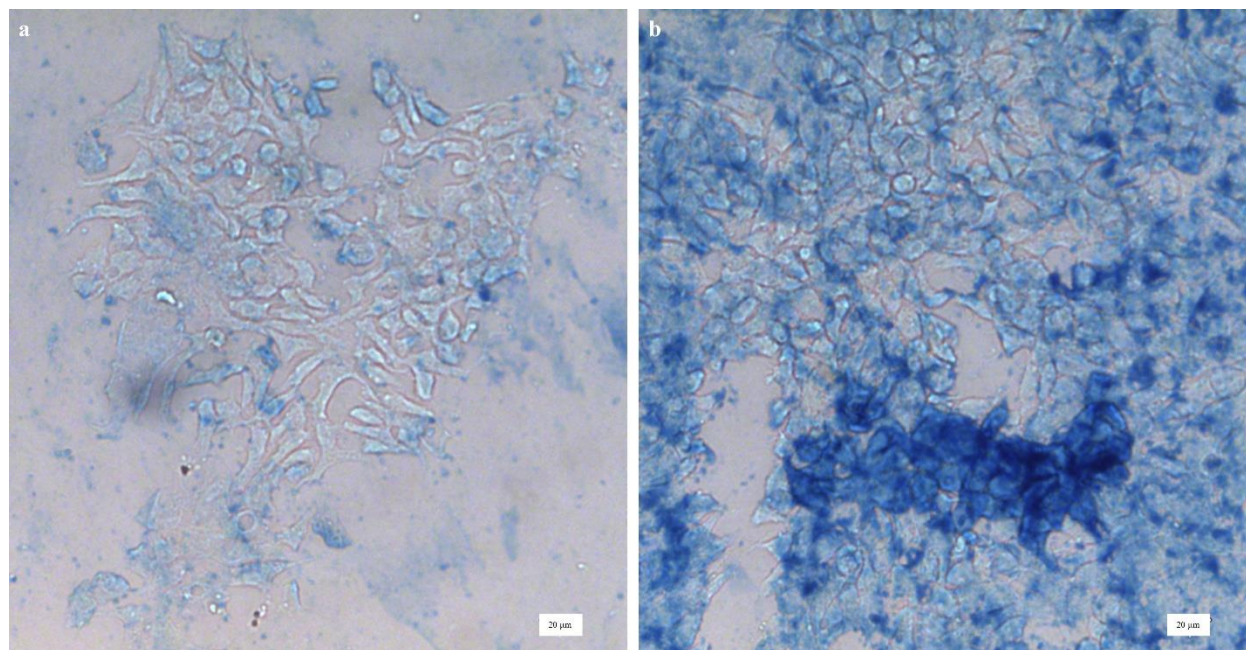


Figure 5.7 Prussian blue staining of SH-SY5Y cells. (a) Cells incubated with unfunctionalized IONPs, (b) cells incubated with Atto647-A β 42-IONPs. Cell images were taken using a Leica DM5500B upright widefield fluorescence and BF microscope, with a 10X objective.

The selectivity of Atto647-A β 42-IONPs towards neuronal cells was validated by concurrently labelling SH-SY5Y and HCT-116 human colon cancer cells using Atto647-A β 42-IONPs. Using a confocal microscope, the dye-labeled peptides on the surface of the IONPs make it possible to detect the nanoparticles uptake. As shown in Figure 5.8, the SH-SY5Y cells which had been previously incubated with Atto647-A β 42-IONPs show a significant uptake of the nanoparticles.

Strong fluorescence was detected in the cytoplasm of the SH-SY5Y cells. Meanwhile, HCT-116 cells that had also been incubated with the same quantity of Atto647-A β 42-IONPs show negligible fluorescence signals. This obvious difference in the cellular uptake of Atto647-A β 42-IONPs suggests that this peptide-functionalized nanoprobe is targeting SH-SY5Y cells specifically.

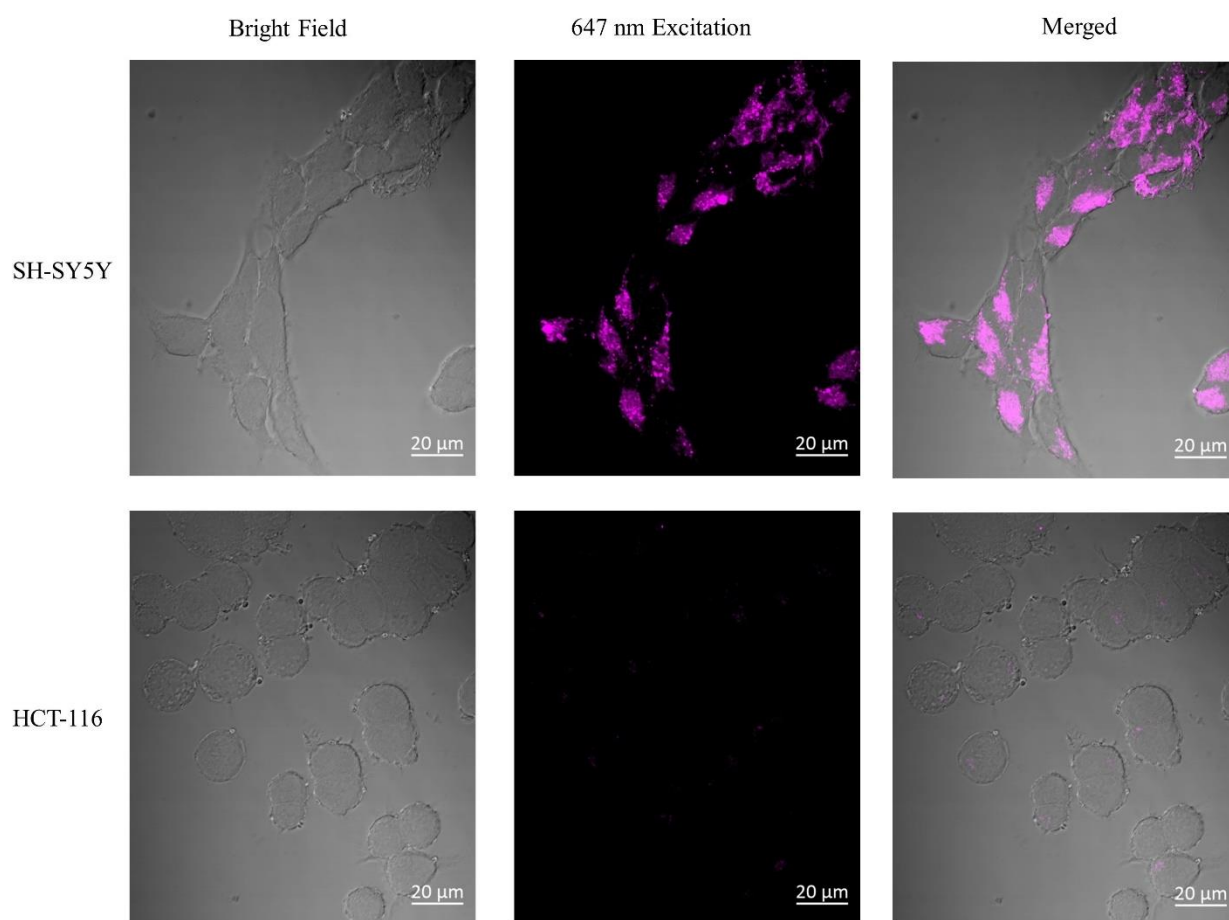


Figure 5.8 Confocal images of SH-SY5Y and HCT-116 cells. Both cells incubated with Atto647-A β 42-IONPs for 6 hours before imaging. Cells images were taken using a Zeiss LSM 800 upright confocal microscope with a 20X objective.

5.5. MR Relaxivity Measurement

The contrasting capability of IONPs can be quantified by their relaxivity. As shown in Formula 5.2, relaxivity describes how the observed proton relaxation time changes as a function of the

magnetic materials' concentration. The relaxivity value of a contrast agent can be affected by temperature, field strength and surrounding medium in which the agents are dispersed [260] [261].

$$1/T_i = 1/T_i^0 + r_i[C], i = 1,2 \quad \dots\dots\dots 5.2$$

$1/T_i$ is the T_1 or T_2 relaxation rates.

$1/T_i^0$ is the intrinsic relaxation rate of the examined sample.

$r_i = T_1$ or T_2 relaxivities

$[C]$ = Concentration of magnetic materials.

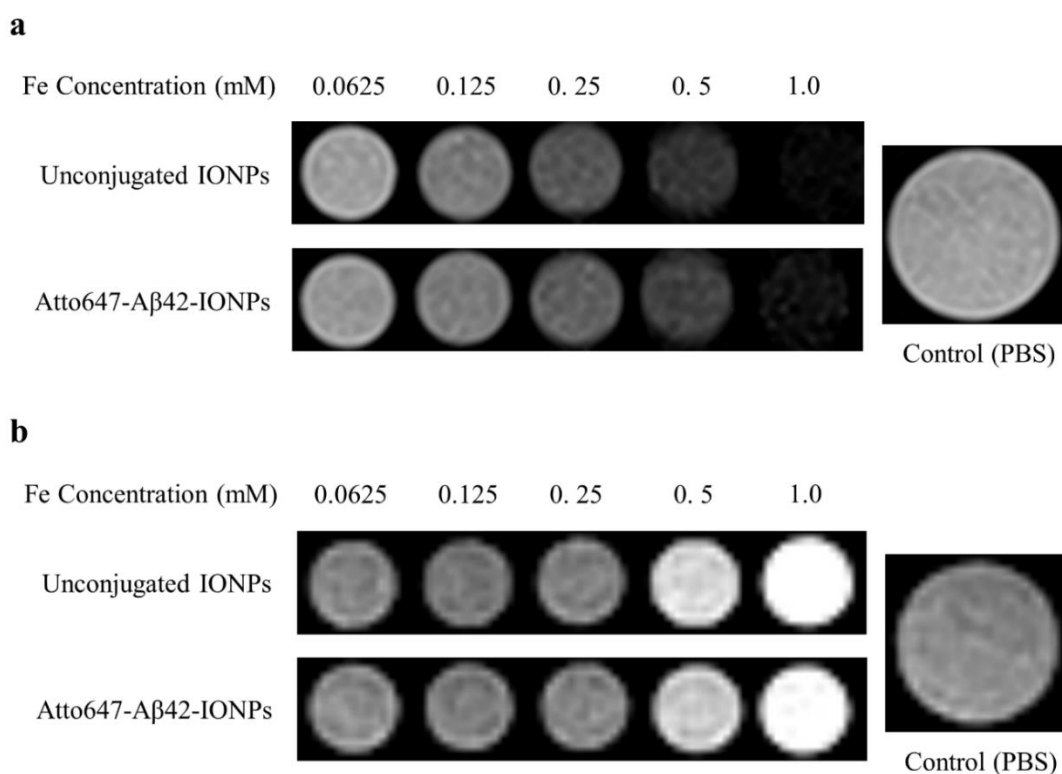


Figure 5.9 MR images of Atto647-Aβ42-IONPs and unconjugated IONPs. (a) T_2 weighted MR images and (b) T_1 weighted MR images.

Figure 5.9 shows the MR images for the two types of IONPs in different concentrations. Compared to the control images, it was obvious that both conjugated and unconjugated IONPs could enhance the MR contrast in T_1 and T_2 weighted MR images.

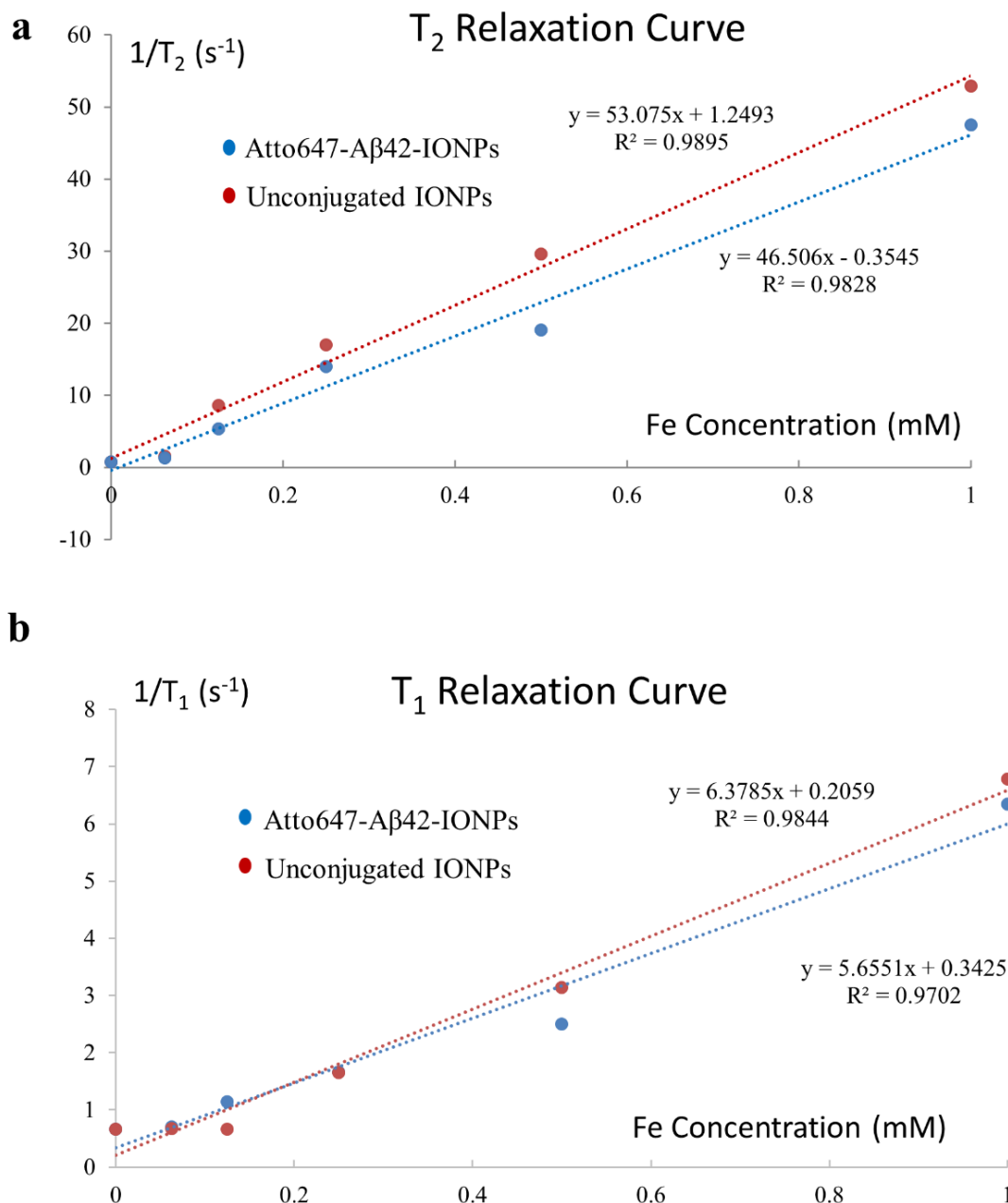


Figure 5.10 T_2 (a) and T_1 (b) relaxation curves of Atto647-A β 42-IONPs and unconjugated IONPs. The r_1 relaxivity of Atto647-A β 42-IONPs is $5.6551 \text{ s}^{-1} \text{ mM}^{-1}$ and r_2 is $46.506 \text{ s}^{-1} \text{ mM}^{-1}$. r_1 of the original IONPs is $6.3785 \text{ s}^{-1} \text{ mM}^{-1}$ and r_2 is $53.075 \text{ s}^{-1} \text{ mM}^{-1}$.

Figure 5.10 shows the relaxation curves for Atto647-A β 42-IONPs and unconjugated IONPs. The relaxivities of two types of IONPs are calculated from the linear slope of fitted curves. For Atto647-A β 42-IONPs, the r_1 value is $5.6551 \text{ s}^{-1} \text{ mM}^{-1}$ and r_2 value is $46.506 \text{ s}^{-1} \text{ mM}^{-1}$. The

original IONPs have slightly higher relaxivities ($r_1 = 6.3785 \text{ s}^{-1} \text{ mM}^{-1}$, $r_2 = 53.075 \text{ s}^{-1} \text{ mM}^{-1}$). The reduced relaxivities are attributed to the conjugation of A β 42 peptides, which increased the hydrodynamic size of the particles. Since the contrasting capability of IONPs depends on the interactions between the surface Fe atom and the water protons nearby, a conjugated A β 42 peptide layer could affect the water's accessibility to the magnetic particles and, consequently, led to a reduced relaxivity [262]. However, as this relaxivity reduction is not significant, the Atto647-A β 42-IONPs can still serve as T_2 contrast agents.

5.5. Summary

This chapter demonstrated the preparation of A β 42 peptides functionalized magnetofluorescent IONPs that can be used for specific targeting of SH-SY5Y neuroblastoma cells. The specificity is due to the selective uptake of A β 42 peptides by the SH-SY5Y cells under *in vitro* conditions. This cellular uptake of amyloid is an important pathological event at the early progression of AD. The specific targeting was confirmed by PB staining and confocal microscopy. In addition, the MR contrasting capability of IONPs was well preserved after the peptide conjugation, suggesting that the functionalized IONPs can be used as bi-functional nanoprobe for both fluorescence and MR imaging. In summary, by specifically targeting neuronal cells that are involved in the cellular uptake of amyloid peptides, A β 42 functionalized IONPs hold a promising potential as multifunctional imaging probes to explore the physiology of AD.

The next chapter is the conclusion chapter. The major contributions of this thesis work to the field will be summarized. The direction for future research will also be discussed.

Chapter 6: Conclusions and Suggestions for Future Research

This chapter begins with conclusions for the whole thesis. The major contributions, accomplished through the various experiments, are highlighted. The chapter ends with suggestions for future research.

6.1. Conclusions

Thanks to the development of medical science and technology, global life expectancy has dramatically improved during the last century. However, this increased life expectancy also entails changes regarding the leading causes of disease and death. One of the most severe diseases threatening the ageing population is AD. The risk of AD increases with age and the progression is irreversible. A body of evidence indicates that the aggregation of extracellular amyloid and the uptake of amyloid peptides by neuronal cells are the major molecular events in the pathogenesis of AD. The detection and intervention of these AD-related amyloids are therefore considered as promising methods for the diagnosis and treatment of AD, respectively. In this thesis, three different nanoparticles were designed and synthesized to detect the presence of amyloid, to modulate the amyloid aggregation, and to target amyloid-related neuronal cells.

The first nanoparticle discussed in this thesis is a Raman/fluorescent bi-functional nanoprobe that can be used for amyloid detection. This nanoprobe was prepared by conjugating RB dyes with amine-functionalized AuNPs. RB is chosen due to its unique Raman fingerprints and affinity with A β peptides. The conjugated RB-AuNPs were utilized for SERS-based A β 42 peptides detection and fluorescence imaging of amyloid plaques. It was demonstrated that the Raman scattering of RB molecules is significantly enhanced when conjugated to the AuNPs and the enhanced Raman spectrum was found to exhibit detectable changes in the presence of amyloid peptides. In addition,

it was also inferred that the interaction between A β 42 peptides and RB-AuNPs generate significantly enhanced fluorescence, which was sufficient for the labeling of amyloid plaques in mouse brain slices. Fluorescence imaging using the RB-AuNPs revealed an age-dependent amyloid deposition. The labelling specificity is also comparable with the commonly used amyloid dye. This proof-of-concept study shows the feasibility of multifunctional nanoprobe for the detection of amyloid. This amyloid detection can contribute to the early diagnosis of AD.

In addition to diagnosis, nanoparticles can also be used as therapeutic agents for AD treatment. During the fibrillization of amyloid peptides, a series of toxic intermediates are produced and consequently lead to cell death. To modulate this fibrillization process and to mitigate the toxicity of amyloid peptides, two types of biocompatible C-dots were synthesized through a facile bottom-up method. Both types of C-dots have excellent biocompatibility and can readily enter neuronal cells. The interactions between A β 42 fibrillization and the two types of C-dots were investigated by ThT assay and TEM. CD-G could accelerate the fibrillization process of A β 42 and CD-I could inhibit it. When incubated with cells, both C-dots could successfully mitigate the toxicity effect induced by the A β 42 peptides. The results suggest that passivation agents play a vital role in the interaction between peptides and C-dots. This study also shows that bottom-up synthesis is a promising method to prepare C-dots-based amyloid inhibitors.

Instead of targeting the extracellular amyloid at molecular level, the last nanoparticles reported in this thesis are magnetofluorescent IONPs which were designed to selectively target the AD-related neuronal cells. The specific targeting is based on the selective uptake of extracellular amyloid by certain neuronal cells. A β 42 peptides were first labelled with Atto 647 dyes and then conjugated with amine-functionalized IONPs. Due to the pre-labeled Atto 647 dyes, the as-prepared A β 42-IONPs are magnetofluorescent. When incubated with SH-SY5Y cells, the cellular

uptake of A β 42-IONPs was enhanced, compared to bare IONPs. Further, by labelling SH-SY5Y and HCT-116 cells, it was found that the A β 42-IONPs are selectively targeting the neuronal cells. This specific neuronal cell targeting is attributed to the cellular uptake of extracellular amyloid by SH-SY5Y cells. In addition, the MR contrasting capability of the A β 42-IONPs is preserved after the functionalization of the peptides. The experimental results suggest that the A β 42 functionalized magnetofluorescent IONPs can be used as bimodal probes to interrogate the cellular uptake of amyloid.

In conclusion, the major results of this thesis can be summarized as follow:

- a) Bi-functional RB-AuNPs were prepared and characterized. The Raman scattering of RB molecules is significantly enhanced when RB is conjugated with AuNPs. In addition, the conjugated RB-AuNPs exhibit detectable changes in their SERS spectrum and fluorescence enhancement when exposed to A β 42 peptides.
- b) RB-AuNPs were applied for the SERS-based detection of A β 42 peptides and the fluorescence imaging of amyloid plaques. With the utilization of RB-AuNPs, age-dependent amyloid depositions were demonstrated in the brains of ageing mice of a transgenic AD mouse model.
- c) Two types of C-dots, CD-G and CD-I, were synthesized through microwave-assisted pyrolysis of sucrose using PEG or PEI as passivation agents. The morphology and optical properties of the C-dots were characterized and the cellular uptake of both C-dots was validated.
- d) The synthesized C-dots were used to modulate the A β 42 fibrillization. The interactions between C-dots and A β 42 were investigated by ThT assay and TEM. It was found that CD-G could accelerate the fibrillization process of A β 42 and CD-I could inhibit it. When

incubated with cells, both C-dots could successfully mitigate the toxicity effect induced by the A β 42 peptides. The results suggest that passivation agents play a vital role in the interaction between peptides and C-dots. This study has also shown that the bottom-up synthesis is a promising method to prepare C-dots-based nanoinhibitors for AD treatment.

- e) Magnetofluorescent IONPs were prepared by conjugating dye-labelled A β 42 peptides with amine-functionalized IONPs. The conjugated A β 42 peptides enabled specific targeting of SH-SY5Y cells by the IONPs, demonstrated both by fluorescent imaging and PB staining. In addition, the MR contrasting capability of IONPs was well retained, confirmed by MR phantom imaging.

6.2. Major Contributions

The major contributions described in this thesis are listed below:

- a) A SERS-fluorescent bi-functional nanoprobe is prepared by conjugating RB with amine-functionalized AuNPs. This nanoprobe is successfully applied for Raman spectroscopic detection of soluble amyloid peptides and fluorescent imaging of amyloid plaques in transgenic mice brains. Furthermore, a novel Raman mapping strategy is proposed and validated to distinguish amyloid-containing mice brain slices.
- b) Two types of biocompatible C-dots are synthesized through a bottom-up, microwave-assisted method. The two C-dots are then utilized to modulate the amyloid aggregation and to mitigate the cytotoxic of A β 42 peptides. Compared to previous reported C-dots inhibitors, the reported bottom-up synthesis method is much more facile and can be scaled up easily. The usage of natural carbon source also enhanced the biocompatibility of synthesized C-dots.

- c) IONPs as nanoprobe are synthesized and applied for specific targeting of neuronal cells. This targeting effect is achieved by functionalizing IONPs with A β 42 peptides. This study suggests that A β 42 functionalized IONPs can be used as multifunctional nanoprobe to investigate the selective neuronal uptake of extracellular amyloid, which is an important cellular event in the pathogenesis of AD.

6.3. Suggestions for Future Research Directions

This thesis has proposed, developed and experimentally demonstrated the application of three nanoparticles for the diagnosis and intervention of AD-related amyloid. To further optimize and improve the efficacy and capability of these nanoparticles, the following future research directions are suggested.

- ✧ The application of the RB-AuNPs was demonstrated in *in vitro* and *postmortem* samples. To further confirm the working efficiency of this nanoprobe, it can be tested in small animal disease models such as transgenic mouse models in which the nanoprobe can be administered via intranasal inoculation. The mice should be imaged by fluorescence and Raman microscopy.



Figure 6.1 Scheme for the designed animal model for in vivo test of RB-AuNPs.

- ✧ Both RB and AuNPs can be used as light-activated inhibitors for amyloid aggregation. For RB, the inhibition is achieved by photodynamic effect [20]. For AuNPs, the therapeutic effect

is attributed to the heat generated from plasmonic absorption [199]. As shown in the previous chapter, the optical properties of RB and AuNPs have not been modified significantly after the conjugation. Therefore, it is reasonable to infer that the RB-AuNPs can also be used as light-activated inhibitors of amyloid aggregation.

- ✧ The C-dots reported in this thesis have emission centers located in the visible range. For therapeutic applications, this emission range is acceptable. However, in order to make the C-dots theranostic agents for *in vivo* application, it is desirable to shift the C-dots' emission range to the NIR window. This can be achieved by changing the passivation agents and manipulating the particle size. To enhance the fluorescence emission, nitrogen doping can also be conducted [86]. In addition, C-dots can also be integrated with other contrast agents such as Gd^{3+} chelates to become multifunctional nanoprobe. This kind of integration could further extend the functionality of C-dots.
- ✧ The therapeutic effect of C-dots can be further validated in small animal models. C-dots can be intranasally delivered to the brain of transgenic mouse which can express amyloid peptides. The dendritic spine density, long-term potentiation (LTP) and behavioral changes of the mice should be monitored to quantify the *in vivo* therapeutic effect of the C-dots.
- ✧ The IONPs presented in this thesis are designed to target neuroblastoma cells. Once internalized, the IONPs are localized in the cytoplasm. To further investigate the intracellular fate of IONPs and how these IONPs interact with intracellular amyloid, a double-seeding model is designed (Figure 6.1). The SH-SY5Y cells are first incubated first with Rhodamine B (RhB) labelled $A\beta_{42}$ peptides ($A\beta_{42}$ -RhB). This $A\beta_{42}$ seeding will induce intracellular amyloid aggregation [63]. Next, the SH-SY5Y cells are incubated again with Fluorescein (FITC)- $A\beta_{42}$ -IONPs. FITC and RhB can form an effective fluorescence resonance energy

transfer (FRET) pair [263]. Therefore, by detecting the FRET phenomenon between FITC and RhB through FRET microscopy, the interactions between IONPs and intracellular amyloid can be revealed.

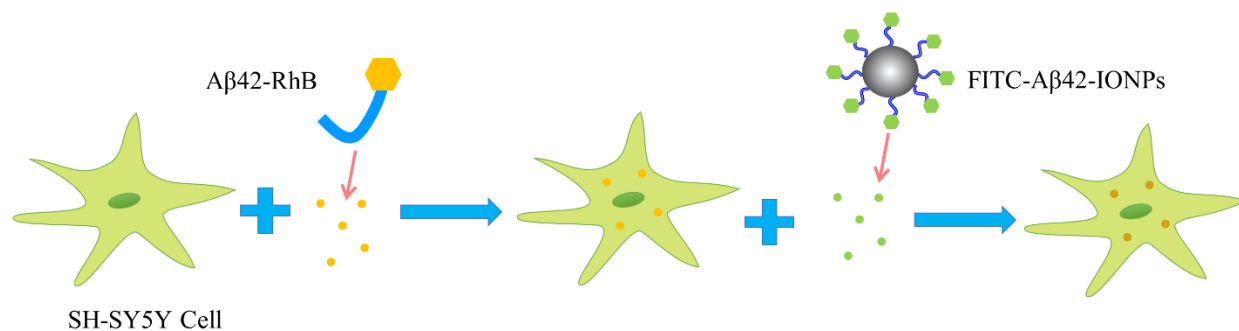


Figure 6.2 Scheme for the designed double-seeding model to investigate the interactions between IONPs and intracellular amyloid.

It is further envisaged that the major results and original contributions presented in this thesis are important to facilitate the application of multifunctional nanoparticles for the detection, imaging, and intervention of amyloid. These research findings are expected to contribute to the development of AD diagnosis and may pave the way for therapeutic interventions to treat AD in near future.

Appendix A.

Methodology for the Synthesis and Application of RB-AuNPs

Materials. A β 42 peptides and supplementary 1% NH₄OH were obtained from Anaspec Inc. (Fremont, USA). Amine-functionalized gold nanoparticles were purchased from Cytodiagnostics Inc. (Ontario, Canada). Rose Bengal disodium salt, 2-(N-morpholino)ethanesulfonic acid (MES), Paraformaldehyde (PFA), Thioflavin T (ThT), 1-ethyl-3-[3-dimethylaminopropyl] carbodiimide hydrochloride (EDC) and N-hydroxysuccinimide (NHS) were purchased from Sigma-Aldrich Co. LLC. FluorSave[®] mounting medium was purchased from EMD Millipore. Disposable PD-10 desalting column was purchased from GE Healthcare (Sweden). MTT Cell Viability Assay Kit was provided by Biotium, Inc (Fremont, USA).

Preparation of RB-AuNP complex. The conjugation of RB to amine-functionalized AuNPs was conducted through a two-step EDC/NHS reaction. First, 10 μ l of RB stock solution (10 mM in water) was diluted with 500 μ l of 0.1 M MES buffer (PH=5.0). Then 4 mg EDC and 6 mg NHS were added to the reaction vial. The mixture was gently stirred at room temperature (RT) for 20 mins, protected from light. After the activation, 200 μ l of AuNPs stock solution (2.46 mg/ml) was mixed with the RB solution. The mixture was stirred for another 3 hours at RT, protected from light. After the conjugation, the sample was centrifuged at 13k RPM for 10 mins and the supernatant was removed. The centrifugation was repeated for two more times using DI water to remove un-conjugated RB. The final RB-AuNP pellet was weighted and re-dispersed in DI water at a mass concentration of 0.3 mg/ml.

Characterization. Transmission electron microscope (TEM) was conducted using a JEM-2010 electron microscope (JEOL Ltd, Japan) under 200 kV voltage. The absorption spectra were

measured using a Shimadzu UV-1800 UV-VIS spectrophotometer. The fluorescent emission was recorded using FS5 Spectrofluorometer (Edinburgh Instruments, UK). The Raman spectrum was measured using inViaTM confocal Raman microscope (Renishaw plc, UK). The zeta potential measurement was conducted using Zeta Nanosizer (Malvern Instruments, UK).

Cytotoxicity assay. 5×10^3 per well of HEK-293 cells were seeded into a 96-well plate with 100 μ l of DMEM/F-12 medium (10% FBS). The 96-well plate was incubated overnight at 37 °C with 5% CO₂. The medium was refreshed with 100 μ l of fresh medium containing PBS or various concentrations of RB-AuNP. The treated cells were incubated for 24 hours and the culturing medium was refreshed again. Next, 10 μ l of MTT solution was added to each well and incubated at 37 °C for another 4 hours. After that, 200 μ l of DMSO was added to each well. The 96-well plate was covered with a tin foil and gently shaken at room temperature for 30 mins to fully dissolve the formazan salt. The absorbance of each well was measured at 570 nm using SynergyTM H1 microplate reader (BioTek, USA). Background absorbance was measured at 630 nm. Each sample was tested in 3 parallel wells.

Preparation of A β 42 peptides solution. The oligomeric A β 42 peptides stock solution was prepared by NaOH treatment, following a previous study with minor modification. Briefly, 1 mg of lyophilized A β 42 peptides were dissolved in 1 ml of ice-cold NaOH solution (0.01 M). The vial was then sonicated for 1 min to fully dissolve the peptides. The actual peptides concentration was measured to be 175 μ M by UV absorbance with an extinction coefficient of 1450 cm⁻¹M⁻¹ at 280 nm. The solution was separated into multiple aliquots of 100 μ l and stored at -20 °C.

Fluorescent detection of the interaction between A β 42 peptides and RB-AuNPs. To confirm the interaction between A β 42 peptides and the as-prepared RB-AuNPs, different concentrations of A β 42 peptides were mixed with 1 μ g/ml of RB-AuNPs. For comparison purpose,

the same concentrations of A β 42 peptides were also mixed with 1 μ M of free RB. The mixtures were transferred to a 96-well plate and the fluorescence emission was recorded (560/590 nm ex/em) using Synergy H1 Multi-Mode plate reader (BioTek Instrument Inc.).

To explore the competing effect between ThT and RB-AuNPs upon A β 42 peptides binding, 5 μ M of A β 42 peptide solutions were mixed with 40 μ M ThT solution. The ThT fluorescence was measured at 440/480 nm ex/em. Then different concentrations of RB-AuNPs were added to the ThT/A β 42 mixture, and then the ThT fluorescence was measured again. To remove the effect of fluorophore crosstalk, mixed ThT/RB-AuNPs solutions without A β 42 peptides were used as blank samples. The viability was then calculated using Origin 9.4.

SERS Detection of A β 42 peptides. Different concentration of A β 42 peptides was mixed with 1 μ g/ml of RB-AuNPs. The concentration of RB-AuNPs is chosen based on the signal intensity (Supplementary Fig. S2). The mixtures were dropped on the surface of pre-cleaned glass slides and left unperturbed for more than 6 hours to dry. The Raman spectra of dried samples were measured using 633 nm laser (30 mW laser power, 10% laser intensity, 3 accumulations, 10 s exposure time) and 1800 grooves/cm grating.

Confocal Imaging of Transgenic Mouse Brain Slices. Mouse brain slices (15 μ m thickness) were harvested from transgenic mice of different ages. Transgenic mice were engineered with three mutations (PP Swedish, MAPT P301L, and PSEN1 M146V) according to a previous study [58]. The brain slices were first incubated with 4% PFA solution for 5 mins in order to fix the brain tissue. After the fixation, the PFA was washed away using PBS. Then the brain slices were stained by dropping 50 μ l of RB-AuNPs solution (10 μ g/ml) or ThT solution (40 μ M) on the surface of the brain slices. After 10 mins incubation, the brain slices were washed twice with PBS to remove excess staining agents. Pre-cleaned coverslips were mounted on top of the brain slices using

FluorSave mounting medium. The confocal images were obtained using a LSM 800 Inverted Confocal Microscope (Zeiss, German). The co-localization analysis was conducted using Imaris 9.1 software (Bitplane, Switzerland).

Appendix B.

Methodology for the Synthesis and Application of C-dots

Materials. A β 42 peptides and supplementary 1% NH₄OH were obtained from Anaspec (Fremont, USA). MTT cell viability assay kit was obtained from Biotium (Fremont, USA). Thioflavin T (ThT), Poly-ethylene imine solution (molecular weight 2000 Da) and Poly-ethylene glycol (molecular weight 1500 Da) were purchased from Sigma-Aldrich. Sucrose (ultra-pure grade) was acquired from Axil Scientific (Singapore).

Synthesis of C-dots. For CD-G, sucrose and PEG1500 were mixed in 4:1 ratio (weight) and then dissolved in deionized water. For CD-I, 4g of sucrose was first dissolved in deionized water and then 1ml of PEI was added to the sucrose solution. Both solutions were sonicated until all the reagents were fully dissolved and dispersed. Next, the two solutions were heated at 150 °C for 5 mins with microwave irradiation using a CEM Discover SP microwave reactor (CEM, USA). After heating, the transparent solutions were transformed into dark brown solutions. To remove large deposits, the brown solutions were centrifuged for 10 mins and the supernatants were collocated. The un-reacted sucrose and passivation agents were purified by dialysis against deionized water (molecular weight cut off = 12 kDa). The purified C-dots were lyophilized into powders and stored for later experiments.

Characterization. The morphology of the C-dots was observed using a JEM-2010 electron microscope (JEOL, Japan) at 200 kV. The fluorescence spectra and the emission maps were obtained using a FS5 spectrofluorometer (Edinburgh Instruments, UK). The UV-Vis spectrum was obtained using a Shimadzu UV-1800 UV-Vis spectrophotometer. The zeta potential was measured using the Zeta Nanosizer (Malvern Instruments, UK).

Cytotoxicity assay and cellular uptake. SH-SY5Y neuroblastoma cells were seeded into a 96-well plate at 8×10^3 cells/well. Each well was filled with 100 μ l of DMEM/F-12 medium (10% FBS) and incubated overnight at 37 °C with 5% CO₂. After the cells were settled, the culturing medium was refreshed with 100 μ l of medium containing various concentrations of C-dots. After 24 hours of incubation, the culturing medium was refreshed again. Next, 10 μ l of MTT solution was added to each well and incubated at 37 °C for another 4 hours, followed by addition of 200 μ l of DMSO in each well. The 96-well plate was covered with a tin foil and gently shaken at room temperature for 30 mins to fully dissolve the formazan salt. The absorbance of each well was measured at 570 nm using Synergy™ H1 microplate reader (BioTek, USA). Background absorbance was measured at 630 nm. Each sample was tested in triplicates.

To confirm the cellular uptake of C-dots, SH-SY5Y cells were seeded in a 6-well plate at a density of 1×10^6 cells/well. Prior to the seeding, a poly-L-lysine coated coverslip was placed in each well. The cells were incubated for 48 hours and then refreshed with 2 ml of fresh medium containing C-dots for 4 hours followed by two PBS washes. After removing the free C-dots, cells were fixed using 4% paraformaldehyde and the coverslips were mounted to glass slides using FluorSave™ mounting medium. The morphology of treated cells was examined using an LSM800 Confocal Microscope (Zeiss, Germany).

Alteration of A β 42 fibrillization by C-dots. To initiate the fibrillation of A β 42 peptides, stock A β 42 solutions were diluted into 20 μ M aliquots then incubated at 37 °C. 10 μ g/ml of CD-G and CD-I were mixed with the A β 42 solution, and kinetics of the fibrillation process were monitored through ThT assay. 10 μ M of ThT was added to the A β 42 solution. At specific time points, aliquots were taken to measure fluorescence at 440 nm excitation / 482 nm emission. After 24 hours of incubation, the morphology of the amyloid fibrils was analysed using TEM at 200 kV.

To reveal the effect of C-dots on the cytotoxicity of A β 42 peptides, SH-SY5Y cells were seeded together with 10 μ g/ml of CD-G and CD-I. 20 μ M stock A β 42 peptide solution was added to cell cultures and then incubated for 24 hours. The viability of the SH-SY5Y cells was measured using the MTT assay.

Appendix C.

Sucrose Density Gradient Centrifugation for C-dots Separation

C-dots that are synthesized from bottom-up approach normally have a relatively wide size distribution. To further separate C-dots based on their size, a sucrose density gradient centrifugation (SDGC) is performed. In SDGC, a density gradient was created by gently overlaying a lower density sucrose solution upon a higher density sucrose solution. The mixed C-dots sample was placed at the top of the sucrose gradient. Under high speed centrifugation, particles travel across the gradient and stop when the density of surrounding sucrose solution matches the particles' densities. For CD-G, 3 different bands (namely L1, L2, and L3) were observed after centrifugation. These bands were then collected separately and C-dot separation was confirmed by their different optical properties (Figure C1).

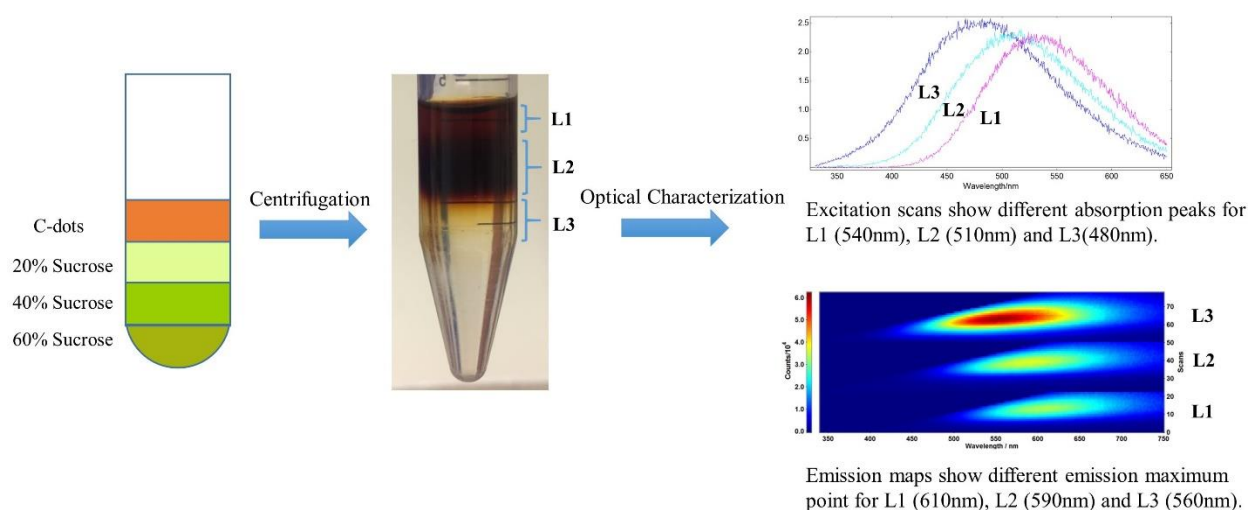


Figure C1 SDGC separation of CD-G. Particle separation was confirmed by different optical properties

Appendix D.

Labelling A β 42 peptides using CD-G

The affinity between A β 42 peptides and C-dots was also used for labeling amyloid fibrils. Amyloid fibrils were prepared by incubating 40 μ M A β 42 solution at 37 °C for 48 hours. 10 μ g/ml A β 42-C-dots conjugates were then added to the amyloid solution and incubated for 1 hour at room temperature with gentle shaking. After the C-dot staining, 30 μ l of the amyloid solution was dropped on a clean coverslip and dried in darkness. The dried amyloid fibrils were mounted to a glass slide using FluorSave™ mounting medium (EMD Millipore, USA). The labeled fibrils were imaged using LSM 800 Upright Confocal Microscope (Zeiss, German). The image is shown in Figure D1. The green fluorescence of CD-G was observed all over the amyloid fibrils.

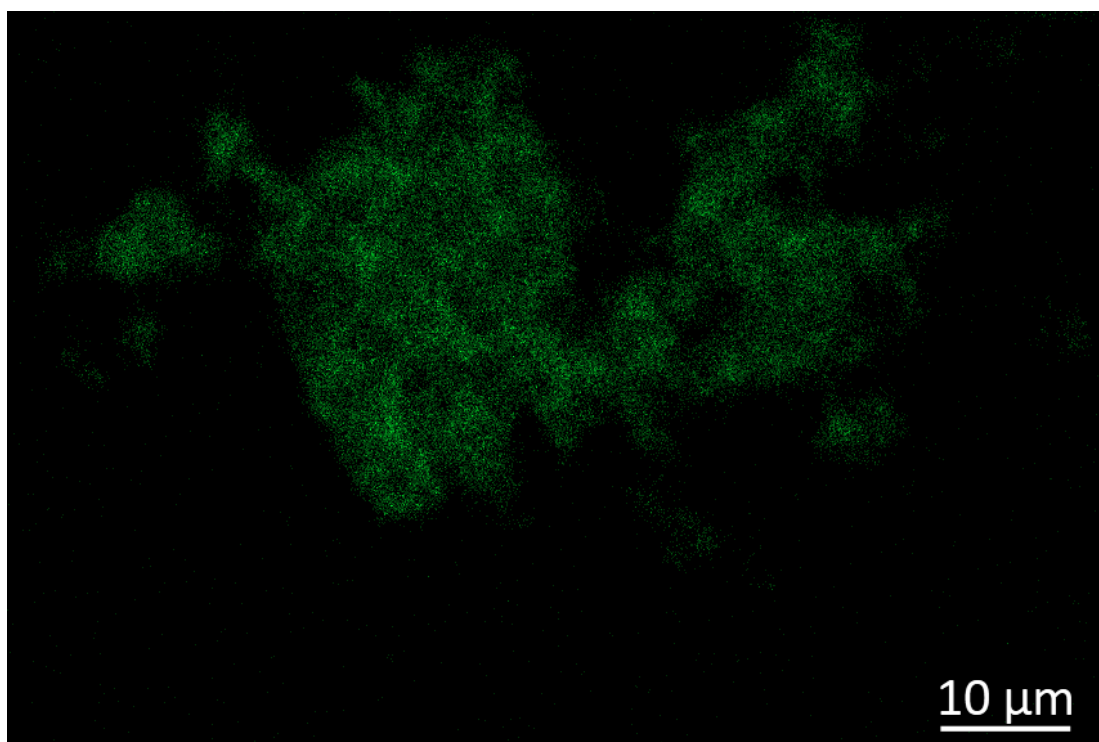


Figure D1 A β 42 fibrils labeled using A β 42-C-dots conjugates. Image was taken under 488 nm excitation.

Appendix E.

Methodology for the Preparation and Application of Atto647-A β 42-IONPs

Materials. Amine-functionalized IONPs (IONP-NH₂) with an average size of 10 nm were purchased from Ocean NanoTech (San Diego, USA). Human Beta-Amyloid (1-42) was supplied by AnaSpec Inc (Fremont, USA). Atto 647N Protein Labeling Kit, 1-ethyl-3-[3-dimethylaminopropyl] carbodiimide hydrochloride (EDC), N-hydroxysuccinimide (NHS), 0.1 % Poly-L-lysine solution (PLL) and sodium hydroxide (NaOH) were obtained from Sigma-Aldrich Co. LLC. Disposable PD-10 desalting columns were purchased from GE Healthcare (Sweden). MTT Cell Viability Assay Kit was provided by Biotium, Inc (Fremont, USA). FluorSave™ mounting medium was purchased from EMD Millipore.

A β 42 peptides labelling. The labelling of A β 42 peptides with Atto 647N dyes was conducted according to the supplier's protocols with minor modification. 0.24 mg of Atto 647N dyes was dissolved with 20 μ l of DMSO and then quickly added to 200 μ l of A β 42 solution. The mixed solution was covered with tin foil and incubated at 4°C for 12 hours with continuous shaking. After the reaction, the labeled peptides were purified by size-exclusive chromatography (SEC) using PD-10 columns. The dye/peptide ratio was determined by measuring the absorbance at 280 nm and 647 nm. The purified conjugates were lyophilized and stored at -20°C.

A β 42-IONPs conjugation. The conjugation of A β 42 with IONPs was achieved through a one-step EDC/NHS reaction. 0.1 mg of lyophilized Atto647-A β 42 peptides was dissolved in 500 μ l ice-cold PBS and then mixed with 200 μ l IONPs solution (5 mg/ml). 26.5 mg EDC and 13.5 mg NHS were mixed and then dissolved with 1 ml of PBS and then 100 μ l of the EDC/NHS solution

was immediately added to the IONPs/peptides mixture. The reaction vial was covered with a tin foil and incubated at 4°C for 12 hours with continuous shaking. The conjugated Atto647-A β 42-IONPs were purified using PD-10 columns.

Characterization. Transmission electron microscope (TEM) was conducted using a JEOL JEM-2010 electron microscope (JEOL Ltd, Japan) under 200 kV voltage. The UV-Vis spectrum was measured using Nanodrop 2000 spectrophotometers (Thermo Scientific, USA). The fluorescence emission was measured using an FS5 spectrofluorometer (Edinburgh Instruments, UK). Hydrodynamic diameters of the IONPs were measured by differential light scattering using Zeta Nanosizer (Malvern Instruments, UK).

Fluorescent Cell Imaging and PB staining. Coverslips were autoclaved and placed in six-well cell culture plates. PLL solution was used to coat the coverslips to enhance the cell adhesion [264]. 1×10^6 /well SH-SY5Y and HCT-116 cells were seeded to the plate with 2 ml of DMEM/F-12 medium (10% FBS). The cells were incubated for 48 hours and then refreshed with 2 ml of fresh medium containing Atto647-A β 42-IONPs or unconjugated IONPs. The cells were further incubated for 6 hours and then were washed with PBS for two times. For PB staining, the cells were incubated with PB working solution for 30 mins (4% PB and 4% HCl mixed in 1:1 ratio). After the PB staining, the cells were washed again with PBS. Next, the cells were fixed using 4% paraformaldehyde at RT for 5 mins. The coverslips were mounted to glass slides using FluorSave™ mounting medium. For fluorescent imaging, the fixed coverslips were imaged using an LSM 800 Upright Confocal Microscope (Zeiss, Germany). For PB stained cells, the cell images were obtained using a DM5500B upright widefield fluorescence and BF microscope (Leica, Germany).

Relaxivity Measurement. The relaxivities r_1 and r_2 of the Atto647-A β 42-IONPs and the unconjugated IONPs were measured in a 3 Tesla MAGNETOM Prisma MRI scanner (Siemens Healthcare, Germany). The particles are prepared in different Fe concentrations (0.0625, 0.125, 0.25, 0.5 and 1 mM) in 1 ml syringes. For r_1 relaxivity measurement, inversion recovery sequences were established by taking images using the following inversion times: 30, 50, 100, 200, 300, 400, 500, 600, 700, 800, 900, 1000, 1200, 1400, 1600, 1800, 2000, 2200, 2400, 2600 and 2800 msec. For r_2 relaxivity measurement, the echo times were set to be 10, 20, 30, 40, 50, 60, 70, 80, 90, 100, 110, 120, 130, 140, 150, 160, 170, 180, 190, 200 msec. The experiments were performed at room temperature with 1 mm slice thickness and 1 average. The acquired images were analyzed using ImageJ (NIH, Washington D.C.) to calculate the relaxation times (T_1 and T_2) for each concentration. Finally, the values of $1/T_1$ and $1/T_2$ were plotted against the corresponding Fe concentrations, and the relaxivities were calculated from the linear fit of these plots.

List of Publications

Journal

- [1]. Y. Xia, V. M. Murukeshan, H. Su, P. Padmanabhan, and B. Gulyás, "Nanoparticulate Contrast Agents for Multimodality Molecular Imaging," *Journal of Biomedical Nanotechnology*, vol. 12, pp. 1553-1584, 2016.
- [2]. Y. Xia, P. Padmanabhan, S.Sreelatha, B. Gulyás, and V. M. Murukeshan, "Bifunctional Fluorescent/Raman Nanoprobe for the Early Detection of Amyloid," *Scientific Reports* (Nature Publishing Group), 2019 (Under review).
- [3]. Y. Xia, P. Padmanabhan, B. Gulyás, and V. M. Murukeshan, "Bottom-up Synthesized Biocompatible Carbon Dots for Alteration of A β 42 Fibrillization and Mitigation of Amyloid Toxicity," *Journal of Biomedical Nanotechnology*, 2019 (Accepted).
- [4]. Y. Xia, P. Padmanabhan, V. Vijayaragavan, V. M. Murukeshan, and B. Gulyás, "A β 42 Peptide Functionalized Iron Oxide Nanoparticles for Specific Targeting of SH-SY5Y Neuroblastoma Cells," *Journal of Nanoscience and Nanotechnology*, 2019 (Under review).

Conference

- [1]. Y. Xia, P. Padmanabhan, V. M. Murukeshan, and B. Gulyás, "Multifunctional Nanoprobe for Amyloid Imaging," *39th Annual Meeting of the Japan Neuroscience Society*, 2016.
- [2]. Y. Xia, P. Padmanabhan, B. Gulyás, and V. M. Murukeshan, "Peptides functionalized carbon dots for *in vitro* fluorescent imaging of amyloid fibrils," *Lasers and Electro-Optics Pacific Rim (CLEO-PR)*, 2017.

References

- [1] M. Prince, A. Comas-Herrera, M. Knapp, M. Guerchet, and M. Karagiannidou, "World Alzheimer report 2016: improving healthcare for people living with dementia: coverage, quality and costs now and in the future," 2016.
- [2] K. Jin, J. W. Simpkins, X. Ji, M. Leis, and I. Stambler, "The critical need to promote research of aging and aging-related diseases to improve health and longevity of the elderly population," *Aging and disease*, vol. 6, p. 1, 2015.
- [3] T. C. Saido, "Metabolism of amyloid β peptide and pathogenesis of Alzheimer's disease," *Proceedings of the Japan Academy, Series B*, vol. 89, pp. 321-339, 2013.
- [4] R. Kaye and C. A. Lasagna-Reeves, "Molecular mechanisms of amyloid oligomers toxicity," *Journal of Alzheimer's Disease*, vol. 33, pp. S67-S78, 2013.
- [5] G. Waldemar, B. Dubois, M. Emre, J. Georges, I. McKeith, M. Rossor, *et al.*, "Recommendations for the diagnosis and management of Alzheimer's disease and other disorders associated with dementia: EFNS guideline," *European Journal of Neurology*, vol. 14, pp. e1-e26, 2007.
- [6] S. L. Risacher and A. J. Saykin, "Neuroimaging and other biomarkers for Alzheimer's disease: the changing landscape of early detection," *Annual review of clinical psychology*, vol. 9, p. 621, 2013.
- [7] M.-m. Xu, W.-m. Ren, X.-c. Tang, Y.-h. Hu, and H.-y. Zhang, "Advances in development of fluorescent probes for detecting amyloid- β aggregates," *Acta Pharmacologica Sinica*, vol. 37, p. 719, 2016.
- [8] P. L. Stiles, J. A. Dieringer, N. C. Shah, and R. P. Van Duyne, "Surface-enhanced Raman spectroscopy," *Annu. Rev. Anal. Chem.*, vol. 1, pp. 601-626, 2008.
- [9] K. Kneipp, M. Moskovits, and H. Kneipp, "Surface-enhanced Raman scattering," *Physics Today*, vol. 60, p. 40, 2007.
- [10] R. A. Alvarez - Puebla and L. M. Liz - Marzán, "SERS - based diagnosis and biodetection," *Small*, vol. 6, pp. 604-610, 2010.
- [11] K. C. Bantz, A. F. Meyer, N. J. Wittenberg, H. Im, Ö. Kurtuluş, S. H. Lee, *et al.*, "Recent progress in SERS biosensing," *Physical Chemistry Chemical Physics*, vol. 13, pp. 11551-11567, 2011.
- [12] W. Xie and S. Schlücker, "Medical applications of surface-enhanced Raman scattering," *Physical Chemistry Chemical Physics*, vol. 15, pp. 5329-5344, 2013.
- [13] S. Schlücker, "Surface - Enhanced raman spectroscopy: Concepts and chemical applications," *Angewandte Chemie International Edition*, vol. 53, pp. 4756-4795, 2014.

- [14] L. A. Lane, X. Qian, and S. Nie, "SERS nanoparticles in medicine: from label-free detection to spectroscopic tagging," *Chem. Rev.*, vol. 115, pp. 10489-10529, 2015.
- [15] M. D. Porter, R. J. Lipert, L. M. Siperko, G. Wang, and R. Narayanan, "SERS as a bioassay platform: fundamentals, design, and applications," *Chemical Society Reviews*, vol. 37, pp. 1001-1011, 2008.
- [16] J. Folch, D. Petrov, M. Ettcheto, S. Abad, E. Sánchez-López, M. L. García, *et al.*, "Current research therapeutic strategies for Alzheimer's disease treatment," *Neural plasticity*, vol. 2016, 2016.
- [17] A. Frydman - Marom, M. Rechter, I. Shefler, Y. Bram, D. E. Shalev, and E. Gazit, "Cognitive - performance recovery of Alzheimer's disease model mice by modulation of early soluble amyloid assemblies," *Angewandte Chemie International Edition*, vol. 48, pp. 1981-1986, 2009.
- [18] T. Bachhuber, N. Katzmarski, J. F. McCarter, D. Loreth, S. Tahirovic, F. Kamp, *et al.*, "Inhibition of amyloid- β plaque formation by α -synuclein," *Nature medicine*, vol. 21, p. 802, 2015.
- [19] J. Sevigny, P. Chiao, T. Bussière, P. H. Weinreb, L. Williams, M. Maier, *et al.*, "The antibody aducanumab reduces A β plaques in Alzheimer's disease," *Nature*, vol. 537, pp. 50-56, 2016.
- [20] J. S. Lee, B. I. Lee, and C. B. Park, "Photo-induced inhibition of Alzheimer's β -amyloid aggregation in vitro by rose bengal," *Biomaterials*, vol. 38, pp. 43-49, 2015.
- [21] B. I. Lee, S. Lee, Y. S. Suh, J. S. Lee, A. k. Kim, O. Y. Kwon, *et al.*, "Photoexcited Porphyrins as a Strong Suppressor of β - Amyloid Aggregation and Synaptic Toxicity," *Angewandte Chemie*, vol. 127, pp. 11634-11638, 2015.
- [22] S. Shariatizi, A. A. Meratan, A. Ghasemi, and M. Nemat-Gorgani, "Inhibition of amyloid fibrillation and cytotoxicity of lysozyme fibrillation products by polyphenols," *International journal of biological macromolecules*, vol. 80, pp. 95-106, 2015.
- [23] A. J. Doig and P. Derreumaux, "Inhibition of protein aggregation and amyloid formation by small molecules," *Current opinion in structural biology*, vol. 30, pp. 50-56, 2015.
- [24] S. S. Kelkar and T. M. Reineke, "Theranostics: Combining Imaging and Therapy," *Bioconjugate Chemistry*, vol. 22, pp. 1879-1903, 2011/10/19 2011.
- [25] N. Xiong, X.-Y. Dong, J. Zheng, F.-F. Liu, and Y. Sun, "Design of LVFFARK and LVFFARK-functionalized nanoparticles for inhibiting amyloid β -protein fibrillation and cytotoxicity," *ACS applied materials & interfaces*, vol. 7, pp. 5650-5662, 2015.
- [26] D. Hu, H. Li, B. Wang, Z. Ye, W. Lei, F. Jia, *et al.*, "Surface-Adaptive Gold Nanoparticles with Effective Adherence and Enhanced Photothermal Ablation of Methicillin-Resistant Staphylococcus aureus Biofilm," *ACS nano*, vol. 11, pp. 9330-9339, 2017.

- [27] H. Tong, K. Lou, and W. Wang, "Near-infrared fluorescent probes for imaging of amyloid plaques in Alzheimer's disease," *Acta pharmaceutica sinica B*, vol. 5, pp. 25-33, 2015.
- [28] V. Camus, P. Payoux, L. Barré, B. Desgranges, T. Voisin, C. Tauber, *et al.*, "Using PET with 18 F-AV-45 (florbetapir) to quantify brain amyloid load in a clinical environment," *European journal of nuclear medicine and molecular imaging*, vol. 39, pp. 621-631, 2012.
- [29] D. F. Wong, A. R. Moghekar, D. Rigamonti, J. R. Brašić, O. Rousset, W. Willis, *et al.*, "An in vivo evaluation of cerebral cortical amyloid with [18 F] flutemetamol using positron emission tomography compared with parietal biopsy samples in living normal pressure hydrocephalus patients," *Molecular Imaging and Biology*, vol. 15, pp. 230-237, 2013.
- [30] S. R. Cherry, "Multimodality Imaging: Beyond PET/CT and SPECT/CT," *Seminars in Nuclear Medicine*, vol. 39, pp. 348-353, 9// 2009.
- [31] T. Vo - Dinh, H. N. Wang, and J. Scaffidi, "Plasmonic nanoprobe for SERS biosensing and bioimaging," *Journal of biophotonics*, vol. 3, pp. 89-102, 2010.
- [32] X. Niu, H. Chen, Y. Wang, W. Wang, X. Sun, and L. Chen, "Upconversion fluorescence-SERS dual-mode tags for cellular and in vivo imaging," *ACS applied materials & interfaces*, vol. 6, pp. 5152-5160, 2014.
- [33] S. Lee, H. Chon, S.-Y. Yoon, E. K. Lee, S.-I. Chang, D. W. Lim, *et al.*, "Fabrication of SERS-fluorescence dual modal nanoprobe and application to multiplex cancer cell imaging," *Nanoscale*, vol. 4, pp. 124-129, 2012.
- [34] S. Bamrungsap, A. Treetong, C. Apiwat, T. Wuttikhun, and T. Dharakul, "SERS-fluorescence dual mode nanotags for cervical cancer detection using aptamers conjugated to gold-silver nanorods," *Microchimica Acta*, vol. 183, pp. 249-256, 2016.
- [35] M. V. Yigit, L. Zhu, M. A. Ifediba, Y. Zhang, K. Carr, A. Moore, *et al.*, "Noninvasive MRI-SERS imaging in living mice using an innately bimodal nanomaterial," *ACS nano*, vol. 5, pp. 1056-1066, 2010.
- [36] V. Amendola, S. Scaramuzza, L. Litti, M. Meneghetti, G. Zuccolotto, A. Rosato, *et al.*, "Magneto - Plasmonic Au - Fe Alloy Nanoparticles Designed for Multimodal SERS - MRI - CT Imaging," *Small*, vol. 10, pp. 2476-2486, 2014.
- [37] Z. Wang, S. Zong, J. Yang, J. Li, and Y. Cui, "Dual-mode probe based on mesoporous silica coated gold nanorods for targeting cancer cells," *Biosensors and Bioelectronics*, vol. 26, pp. 2883-2889, 2011.
- [38] P. S. Aisen, S. Gauthier, S. H. Ferris, D. Saumier, D. Haine, D. Garceau, *et al.*, "Tramiprosate in mild-to-moderate Alzheimer's disease—a randomized, double-blind, placebo-controlled, multi-centre study (the Alphase Study)," *Archives of medical science: AMS*, vol. 7, p. 102, 2011.
- [39] M. Zhang, X. Mao, Y. Yu, C. X. Wang, Y. L. Yang, and C. Wang, "Nanomaterials for reducing amyloid cytotoxicity," *Advanced Materials*, vol. 25, pp. 3780-3801, 2013.

- [40] B. Song, Y. Zhang, J. Liu, X. Feng, T. Zhou, and L. Shao, "Is neurotoxicity of metallic nanoparticles the cascades of oxidative stress?," *Nanoscale research letters*, vol. 11, p. 291, 2016.
- [41] L. M. Billings, S. Oddo, K. N. Green, J. L. McGaugh, and F. M. LaFerla, "Intraneuronal A β causes the onset of early Alzheimer's disease-related cognitive deficits in transgenic mice," *Neuron*, vol. 45, pp. 675-688, 2005.
- [42] A. Alzheimer, *A Characteristic Disease of the Cerebral Cortex: Meeting of South-West Germany Psychiatrists Held in Tübingen on November 3rd and 4th, 1906*, 1907.
- [43] E. Karran, M. Mercken, and B. De Strooper, "The amyloid cascade hypothesis for Alzheimer's disease: an appraisal for the development of therapeutics," *Nature reviews Drug discovery*, vol. 10, p. 698, 2011.
- [44] A. Goate, M.-C. Chartier-Harlin, M. Mullan, J. Brown, F. Crawford, L. Fidani, *et al.*, "Segregation of a missense mutation in the amyloid precursor protein gene with familial Alzheimer's disease," *Nature*, vol. 349, p. 704, 1991.
- [45] R. Sherrington, E. Rogaev, Y. a. Liang, E. Rogaeva, G. Levesque, M. Ikeda, *et al.*, "Cloning of a gene bearing missense mutations in early-onset familial Alzheimer's disease," *Nature*, vol. 375, p. 754, 1995.
- [46] E. Levy-Lahad, W. Wasco, P. Poorkaj, D. M. Romano, J. Oshima, W. H. Pettingell, *et al.*, "Candidate gene for the chromosome 1 familial Alzheimer's disease locus," *Science*, vol. 269, pp. 973-977, 1995.
- [47] C. Bohm, F. Chen, J. Sevalle, S. Qamar, R. Dodd, Y. Li, *et al.*, "Current and future implications of basic and translational research on amyloid- β peptide production and removal pathways," *Molecular and Cellular Neuroscience*, vol. 66, pp. 3-11, 2015.
- [48] J. Kim, J. M. Basak, and D. M. Holtzman, "The role of apolipoprotein E in Alzheimer's disease," *Neuron*, vol. 63, pp. 287-303, 2009.
- [49] M. P. Lambert, A. Barlow, B. A. Chromy, C. Edwards, R. Freed, M. Liosatos, *et al.*, "Diffusible, nonfibrillar ligands derived from A β 1-42 are potent central nervous system neurotoxins," *Proceedings of the National Academy of Sciences*, vol. 95, pp. 6448-6453, 1998.
- [50] C. G. Glabe, "Common mechanisms of amyloid oligomer pathogenesis in degenerative disease," *Neurobiology of aging*, vol. 27, pp. 570-575, 2006.
- [51] I. Grundke-Iqbal, K. Iqbal, L. George, Y.-C. Tung, K. S. Kim, and H. M. Wisniewski, "Amyloid protein and neurofibrillary tangles coexist in the same neuron in Alzheimer disease," *Proceedings of the National Academy of Sciences*, vol. 86, pp. 2853-2857, 1989.
- [52] G. K. Gouras, J. Tsai, J. Naslund, B. Vincent, M. Edgar, F. Checler, *et al.*, "Intraneuronal A β 42 accumulation in human brain," *The American journal of pathology*, vol. 156, pp. 15-20, 2000.

- [53] K. A. Gyure, R. Durham, W. F. Stewart, J. E. Smialek, and J. C. Troncoso, "Intraneuronal A β -amyloid precedes development of amyloid plaques in Down syndrome," *Archives of pathology & laboratory medicine*, vol. 125, pp. 489-492, 2001.
- [54] R. H. Takahashi, T. A. Milner, F. Li, E. E. Nam, M. A. Edgar, H. Yamaguchi, *et al.*, "Intraneuronal Alzheimer A β 42 accumulates in multivesicular bodies and is associated with synaptic pathology," *The American journal of pathology*, vol. 161, pp. 1869-1879, 2002.
- [55] C. G. Almeida, R. H. Takahashi, and G. K. Gouras, " β -Amyloid accumulation impairs multivesicular body sorting by inhibiting the ubiquitin-proteasome system," *Journal of Neuroscience*, vol. 26, pp. 4277-4288, 2006.
- [56] F. M. LaFerla, K. N. Green, and S. Oddo, "Intracellular amyloid- β in Alzheimer's disease," *Nature Reviews Neuroscience*, vol. 8, p. 499, 2007.
- [57] R. D. Readnower, A. D. Sauerbeck, and P. G. Sullivan, "Mitochondria, amyloid β , and Alzheimer's disease," *International Journal of Alzheimer's Disease*, vol. 2011, 2011.
- [58] S. Oddo, A. Caccamo, J. D. Shepherd, M. P. Murphy, T. E. Golde, R. Kaye, *et al.*, "Triple-transgenic model of Alzheimer's disease with plaques and tangles: intracellular A β and synaptic dysfunction," *Neuron*, vol. 39, pp. 409-421, 2003.
- [59] T. Hartmann, S. C. Bieger, B. Brühl, P. J. Tienari, N. Ida, D. Allsop, *et al.*, "Distinct sites of intracellular production for Alzheimer's disease A β 40/42 amyloid peptides," *Nature medicine*, vol. 3, p. 1016, 1997.
- [60] R. Deane, S. Du Yan, R. K. Subramanian, B. LaRue, S. Jovanovic, E. Hogg, *et al.*, "RAGE mediates amyloid- β peptide transport across the blood-brain barrier and accumulation in brain," *Nature medicine*, vol. 9, p. 907, 2003.
- [61] R. Nagele, M. D'andrea, W. Anderson, and H.-Y. Wang, "Intracellular accumulation of β -amyloid1-42 in neurons is facilitated by the α 7 nicotinic acetylcholine receptor in Alzheimer's disease," *Neuroscience*, vol. 110, pp. 199-211, 2002.
- [62] P. M. Clifford, S. Zarrabi, G. Siu, K. J. Kinsler, M. C. Kosciuk, V. Venkataraman, *et al.*, "A β peptides can enter the brain through a defective blood-brain barrier and bind selectively to neurons," *Brain research*, vol. 1142, pp. 223-236, 2007.
- [63] X. Hu, S. L. Crick, G. Bu, C. Frieden, R. V. Pappu, and J.-M. Lee, "Amyloid seeds formed by cellular uptake, concentration, and aggregation of the amyloid-beta peptide," *Proceedings of the National Academy of Sciences*, vol. 106, pp. 20324-20329, 2009.
- [64] K. Chiang and E. H. Koo, "Emerging therapeutics for Alzheimer's disease," *Annual review of pharmacology and toxicology*, vol. 54, pp. 381-405, 2014.
- [65] B. P. Imbimbo and G. AM Giardina, " γ -secretase inhibitors and modulators for the treatment of Alzheimer's disease: disappointments and hopes," *Current topics in medicinal chemistry*, vol. 11, pp. 1555-1570, 2011.

- [66] V. Coric, C. H. van Dyck, S. Salloway, N. Andreasen, M. Brody, R. W. Richter, *et al.*, "Safety and tolerability of the γ -secretase inhibitor avagacestat in a phase 2 study of mild to moderate Alzheimer disease," *Archives of neurology*, vol. 69, pp. 1430-1440, 2012.
- [67] J. L. Eriksen, S. A. Sagi, T. E. Smith, S. Weggen, P. Das, D. McLendon, *et al.*, "NSAIDs and enantiomers of flurbiprofen target γ -secretase and lower A β 42 in vivo," *The Journal of clinical investigation*, vol. 112, pp. 440-449, 2003.
- [68] P. Pasqualetti, C. Bonomini, G. Dal Forno, L. Paulon, E. Sinforiani, C. Marra, *et al.*, "A randomized controlled study on effects of ibuprofen on cognitive progression of Alzheimer's disease," *Aging clinical and experimental research*, vol. 21, pp. 102-110, 2009.
- [69] H. Vanderstichele, E. V. Kerschaver, C. Hesse, P. Davidsson, M.-A. Buyse, N. Andreasen, *et al.*, "Standardization of measurement of β -amyloid (1-42) in cerebrospinal fluid and plasma," *Amyloid*, vol. 7, pp. 245-258, 2000.
- [70] R. J. Baranello, K. L. Bharani, V. Padmaraju, N. Chopra, D. K. Lahiri, N. H. Greig, *et al.*, "Amyloid-beta protein clearance and degradation (ABCD) pathways and their role in Alzheimer's disease," *Current Alzheimer Research*, vol. 12, pp. 32-46, 2015.
- [71] R. J. Bateman, L. Y. Munsell, J. C. Morris, R. Swarm, K. E. Yarasheski, and D. M. Holtzman, "Human amyloid- β synthesis and clearance rates as measured in cerebrospinal fluid in vivo," *Nature medicine*, vol. 12, p. 856, 2006.
- [72] M. Pappolla, K. Sambamurti, R. Vidal, J. Pacheco-Quinto, B. Poeggeler, and E. Matsubara, "Evidence for lymphatic A β clearance in Alzheimer's transgenic mice," *Neurobiology of disease*, vol. 71, pp. 215-219, 2014.
- [73] A. Bilikiewicz and W. Gaus, "Colostrinin 1 (a naturally occurring, proline-rich, polypeptide mixture) in the treatment of Alzheimer's disease," *Journal of Alzheimer's Disease*, vol. 6, pp. 17-26, 2004.
- [74] J. H. Viles, "Metal ions and amyloid fiber formation in neurodegenerative diseases. Copper, zinc and iron in Alzheimer's, Parkinson's and prion diseases," *Coordination Chemistry Reviews*, vol. 256, pp. 2271-2284, 2012.
- [75] M. Cui, "Past and recent progress of molecular imaging probes for β -amyloid plaques in the brain," *Current medicinal chemistry*, vol. 21, pp. 82-112, 2014.
- [76] W. E. Klunk, M. L. Debnath, and J. W. Pettegrew, "Chrysamine-G binding to Alzheimer and control brain: autopsy study of a new amyloid probe," *Neurobiology of aging*, vol. 16, pp. 541-548, 1995.
- [77] W. E. Klunk, H. Engler, A. Nordberg, Y. Wang, G. Blomqvist, D. P. Holt, *et al.*, "Imaging brain amyloid in Alzheimer's disease with Pittsburgh Compound - B," *Annals of neurology*, vol. 55, pp. 306-319, 2004.

- [78] R. Vandenberghe, K. Van Laere, A. Ivanoiu, E. Salmon, C. Bastin, E. Triau, *et al.*, "¹⁸F - flutemetamol amyloid imaging in Alzheimer disease and mild cognitive impairment: A phase 2 trial," *Annals of neurology*, vol. 68, pp. 319-329, 2010.
- [79] H. F. Kung, S. R. Choi, W. Qu, W. Zhang, and D. Skovronsky, "¹⁸F stilbenes and styrylpyridines for PET imaging of A β plaques in Alzheimer's disease: a miniperspective," *Journal of medicinal chemistry*, vol. 53, pp. 933-941, 2009.
- [80] K. Serdons, D. Vanderghinste, M. Van Eeckhoudt, P. Borghgraef, H. Kung, F. Van Leuven, *et al.*, "Synthesis and evaluation of two fluorine - 18 labelled phenylbenzothiazoles as potential in vivo tracers for amyloid plaque imaging," *Journal of Labelled Compounds and Radiopharmaceuticals*, vol. 52, pp. 473-481, 2009.
- [81] K. A. Stephenson, R. Chandra, Z.-P. Zhuang, C. Hou, S. Oya, M.-P. Kung, *et al.*, "Fluoro-pegylated (FPEG) imaging agents targeting A β aggregates," *Bioconjugate chemistry*, vol. 18, pp. 238-246, 2007.
- [82] H. Kobayashi, M. Ogawa, R. Alford, P. L. Choyke, and Y. Urano, "New strategies for fluorescent probe design in medical diagnostic imaging," *Chemical reviews*, vol. 110, pp. 2620-2640, 2009.
- [83] M. Biancalana and S. Koide, "Molecular mechanism of Thioflavin-T binding to amyloid fibrils," *Biochimica et Biophysica Acta (BBA)-Proteins and Proteomics*, vol. 1804, pp. 1405-1412, 2010.
- [84] U. Resch-Genger, M. Grabolle, S. Cavaliere-Jaricot, R. Nitschke, and T. Nann, "Quantum dots versus organic dyes as fluorescent labels," *Nat Meth*, vol. 5, pp. 763-775, 09//print 2008.
- [85] A. Louie, "Multimodality Imaging Probes: Design and Challenges," *Chemical Reviews*, vol. 110, pp. 3146-3195, 2010/05/12 2010.
- [86] Y. Xia, M. V. Matham, H. Su, P. Padmanabhan, and B. Gulyás, "Nanoparticulate Contrast Agents for Multimodality Molecular Imaging," *Journal of Biomedical Nanotechnology*, vol. 12, pp. 1553-1584, // 2016.
- [87] Z. Cheng, A. Al Zaki, J. Z. Hui, V. R. Muzykantov, and A. Tsourkas, "Multifunctional nanoparticles: cost versus benefit of adding targeting and imaging capabilities," *Science*, vol. 338, pp. 903-910, 2012.
- [88] H. Maeda, J. Wu, T. Sawa, Y. Matsumura, and K. Hori, "Tumor vascular permeability and the EPR effect in macromolecular therapeutics: a review," *Journal of Controlled Release*, vol. 65, pp. 271-284, 3/1/ 2000.
- [89] C. Fornaguera, A. Dols-Perez, G. Caldero, M. Garcia-Celma, J. Camarasa, and C. Solans, "PLGA nanoparticles prepared by nano-emulsion templating using low-energy methods as efficient nanocarriers for drug delivery across the blood-brain barrier," *Journal of Controlled Release*, vol. 211, pp. 134-143, 2015.

- [90] Z. Liu, X. Gao, T. Kang, M. Jiang, D. Miao, G. Gu, *et al.*, "B6 peptide-modified PEG-PLA nanoparticles for enhanced brain delivery of neuroprotective peptide," *Bioconjugate chemistry*, vol. 24, pp. 997-1007, 2013.
- [91] K. L. Viola, J. Sbarboro, R. Sureka, M. De, M. A. Bicca, J. Wang, *et al.*, "Towards non-invasive diagnostic imaging of early-stage Alzheimer's disease," *Nature nanotechnology*, vol. 10, p. 91, 2015.
- [92] H. Skaat, E. Corem-Slakmon, I. Grinberg, D. Last, D. Goez, Y. Mardor, *et al.*, "Antibody-conjugated, dual-modal, near-infrared fluorescent iron oxide nanoparticles for anti-amyloidogenic activity and specific detection of amyloid- β fibrils," *International journal of nanomedicine*, vol. 8, p. 4063, 2013.
- [93] L. Feng, H.-Y. Long, R.-K. Liu, D.-N. Sun, C. Liu, L.-L. Long, *et al.*, "A Quantum Dot Probe Conjugated with A β Antibody for Molecular Imaging of Alzheimer's Disease in a Mouse Model," *Cellular and molecular neurobiology*, vol. 33, pp. 759-765, 2013.
- [94] C. Zhang, X. Wan, X. Zheng, X. Shao, Q. Liu, Q. Zhang, *et al.*, "Dual-functional nanoparticles targeting amyloid plaques in the brains of Alzheimer's disease mice," *Biomaterials*, vol. 35, pp. 456-465, 2014.
- [95] S. Mourtas, M. Canovi, C. Zona, D. Aurilia, A. Niarakis, B. La Ferla, *et al.*, "Curcumin-decorated nanoliposomes with very high affinity for amyloid- β 1-42 peptide," *Biomaterials*, vol. 32, pp. 1635-1645, 2011.
- [96] A. L. Clos, R. Kaye, and C. Lasagna Reeves, "Association of skin with the pathogenesis and treatment of neurodegenerative amyloidosis," *Frontiers in neurology*, vol. 3, p. 5, 2012.
- [97] J. P. Castaneda-Cazares and I. Rodriguez-Leyva, "Skin biomarkers for neurodegenerative disease: a future perspective," ed: Future Medicine, 2015.
- [98] T. Shah, S. Gupta, P. Chatterjee, M. Campbell, and R. Martins, "Beta-amyloid sequelae in the eye: a critical review on its diagnostic significance and clinical relevance in Alzheimer's disease," *Molecular psychiatry*, vol. 22, p. 353, 2017.
- [99] F. S. Matsuo, L. F. B. De Paulo, J. P. S. Servato, P. R. de Faria, S. V. Cardoso, and A. M. Loyola, "Involvement of oral tissues by AL amyloidosis: a literature review and report of eight new cases," *Clinical oral investigations*, vol. 20, pp. 1913-1920, 2016.
- [100] L. Guerrini, R. Arenal, B. Mannini, F. Chiti, R. Pini, P. Matteini, *et al.*, "SERS detection of amyloid oligomers on metallorganic-decorated plasmonic beads," *ACS applied materials & interfaces*, vol. 7, pp. 9420-9428, 2015.
- [101] D. Drago, M. Bettella, S. Bolognin, L. Cendron, J. Scancar, R. Milacic, *et al.*, "Potential pathogenic role of β -amyloid1-42-aluminum complex in Alzheimer's disease," *The international journal of biochemistry & cell biology*, vol. 40, pp. 731-746, 2008.
- [102] O. S. Wolfbeis, "An overview of nanoparticles commonly used in fluorescent bioimaging," *Chemical Society Reviews*, vol. 44, pp. 4743-4768, 2015.

- [103] H. M. Kim and B. R. Cho, "Small-molecule two-photon probes for bioimaging applications," *Chemical reviews*, vol. 115, pp. 5014-5055, 2015.
- [104] P. Verwilt, S. Park, B. Yoon, and J. S. Kim, "Recent advances in Gd-chelate based bimodal optical/MRI contrast agents," *Chemical Society Reviews*, vol. 44, pp. 1791-1806, 2015.
- [105] Z. Gao, T. Ma, E. Zhao, D. Docter, W. Yang, R. H. Stauber, *et al.*, "Small is smarter: nano MRI contrast agents—advantages and recent achievements," *Small*, vol. 12, pp. 556-576, 2016.
- [106] B. N. Clarke, "PET Radiopharmaceuticals: What's new, what's reimbursed, and what's next?," *Journal of nuclear medicine technology*, vol. 46, pp. 12-16, 2018.
- [107] J. Garcia, T. Tang, and A. Y. Louie, "Nanoparticle-based multimodal PET/MRI probes," *Nanomedicine*, vol. 10, pp. 1343-1359, 2015.
- [108] J. Zhu, L. Zhao, Y. Cheng, Z. Xiong, Y. Tang, M. Shen, *et al.*, "Radionuclide ¹³¹I-labeled multifunctional dendrimers for targeted SPECT imaging and radiotherapy of tumors," *Nanoscale*, vol. 7, pp. 18169-18178, 2015.
- [109] D. Pan, E. Roessl, J.-P. Schlomka, S. D. Caruthers, A. Senpan, M. J. Scott, *et al.*, "Computed Tomography in Color: NanoK-Enhanced Spectral CT Molecular Imaging," *Angewandte Chemie*, vol. 122, pp. 9829-9833, 2010.
- [110] J. Weber, P. C. Beard, and S. E. Bohndiek, "Contrast agents for molecular photoacoustic imaging," *Nature methods*, vol. 13, p. 639, 2016.
- [111] J. A. Izatt, M. A. Choma, and A.-H. Dhalla, "Theory of optical coherence tomography," in *Optical coherence tomography*, ed: Springer, 2015, pp. 65-94.
- [112] H. Yang, W. Cai, L. Xu, X. Lv, Y. Qiao, P. Li, *et al.*, "Nanobubble–Affibody: Novel ultrasound contrast agents for targeted molecular ultrasound imaging of tumor," *Biomaterials*, vol. 37, pp. 279-288, 2015.
- [113] M. F. Kircher, A. de la Zerda, J. V. Jokerst, C. L. Zavaleta, P. J. Kempen, E. Mittra, *et al.*, "A brain tumor molecular imaging strategy using a new triple-modality MRI-photoacoustic-Raman nanoparticle," *Nat Med*, vol. 18, pp. 829-834, 05//print 2012.
- [114] R. Madru, P. Svenmarker, C. Ingvar, F. Ståhlberg, S.-A. Engels, L. Knutsson, *et al.*, "Development of a Hybrid Nanoprobe for Triple-Modality MR/SPECT/Optical Fluorescence Imaging," *Diagnostics*, vol. 4, p. 13, 2014.
- [115] J. C. Park, M. K. Yu, G. I. An, S.-I. Park, J. Oh, H. J. Kim, *et al.*, "Facile Preparation of a Hybrid Nanoprobe for Triple-Modality Optical/PET/MR Imaging," *Small*, vol. 6, pp. 2863-2868, 2010.
- [116] J. Xie, K. Chen, J. Huang, S. Lee, J. Wang, J. Gao, *et al.*, "PET/NIRF/MRI triple functional iron oxide nanoparticles," *Biomaterials*, vol. 31, pp. 3016-3022, 4// 2010.

- [117] H. Kobayashi, M. R. Longmire, M. Ogawa, and P. L. Choyke, "Rational chemical design of the next generation of molecular imaging probes based on physics and biology: mixing modalities, colors and signals," *Chemical Society Reviews*, vol. 40, pp. 4626-4648, 2011.
- [118] H. B. Na, I. C. Song, and T. Hyeon, "Inorganic Nanoparticles for MRI Contrast Agents," *Advanced Materials*, vol. 21, pp. 2133-2148, 2009.
- [119] H. Soo Choi, W. Liu, P. Misra, E. Tanaka, J. P. Zimmer, B. Itty Ipe, *et al.*, "Renal clearance of quantum dots," *Nat Biotech*, vol. 25, pp. 1165-1170, 10//print 2007.
- [120] M. Longmire, P. L. Choyke, and H. Kobayashi, "Clearance properties of nano-sized particles and molecules as imaging agents: considerations and caveats," *Nanomedicine*, vol. 3, pp. 703-717, 2008/10/01 2008.
- [121] T. Passuello, M. Pedroni, F. Piccinelli, S. Polizzi, P. Marzola, S. Tambalo, *et al.*, "PEG-capped, lanthanide doped GdF₃ nanoparticles: luminescent and T₂ contrast agents for optical and MRI multimodal imaging," *Nanoscale*, vol. 4, pp. 7682-7689, 2012.
- [122] N. Erathodiyil and J. Y. Ying, "Functionalization of Inorganic Nanoparticles for Bioimaging Applications," *Accounts of Chemical Research*, vol. 44, pp. 925-935, 2011/10/18 2011.
- [123] J. M. Harris and R. B. Chess, "Effect of pegylation on pharmaceuticals," *Nat Rev Drug Discov*, vol. 2, pp. 214-221, 03//print 2003.
- [124] S.-D. Li and L. Huang, "Stealth Nanoparticles: High Density but Sheddable PEG is a Key for Tumor Targeting," *Journal of controlled release : official journal of the Controlled Release Society*, vol. 145, pp. 178-181, 03/23 2010.
- [125] C. Allen, N. Dos Santos, R. Gallagher, G. N. C. Chiu, Y. Shu, W. M. Li, *et al.*, "Controlling the Physical Behavior and Biological Performance of Liposome Formulations Through Use of Surface Grafted Poly(ethylene Glycol)," *Bioscience Reports*, vol. 22, pp. 225-250, 2002/04/01 2002.
- [126] K. Y. Choi, H. Y. Yoon, J.-H. Kim, S. M. Bae, R.-W. Park, Y. M. Kang, *et al.*, "Smart Nanocarrier Based on PEGylated Hyaluronic Acid for Cancer Therapy," *ACS Nano*, vol. 5, pp. 8591-8599, 2011/11/22 2011.
- [127] K. Y. Choi, K. H. Min, H. Y. Yoon, K. Kim, J. H. Park, I. C. Kwon, *et al.*, "PEGylation of hyaluronic acid nanoparticles improves tumor targetability in vivo," *Biomaterials*, vol. 32, pp. 1880-1889, 3// 2011.
- [128] J.-H. Ke, J.-J. Lin, J. R. Carey, J.-S. Chen, C.-Y. Chen, and L.-F. Wang, "A specific tumor-targeting magnetofluorescent nanoprobe for dual-modality molecular imaging," *Biomaterials*, vol. 31, pp. 1707-1715, 3// 2010.
- [129] S. Wang, B. R. Jarrett, S. M. Kauzlarich, and A. Y. Louie, "Core/Shell Quantum Dots with High Relaxivity and Photoluminescence for Multimodality Imaging," *Journal of the American Chemical Society*, vol. 129, pp. 3848-3856, 2007/04/01 2007.

- [130] H.-T. Wong, M.-K. Tsang, C.-F. Chan, K.-L. Wong, B. Fei, and J. Hao, "In vitro cell imaging using multifunctional small sized KGdF₄:Yb³⁺,Er³⁺ upconverting nanoparticles synthesized by a one-pot solvothermal process," *Nanoscale*, vol. 5, pp. 3465-3473, 2013.
- [131] S. K. Yen, D. P. Varma, W. M. Guo, V. H. B. Ho, V. Vijayaragavan, P. Padmanabhan, *et al.*, "Synthesis of Small-Sized, Porous, and Low-Toxic Magnetite Nanoparticles by Thin POSS Silica Coating," *Chemistry – A European Journal*, vol. 21, pp. 3914-3918, 2015.
- [132] M. Wang and M. Thanou, "Targeting nanoparticles to cancer," *Pharmacological Research*, vol. 62, pp. 90-99, 8// 2010.
- [133] F. Dubois, B. Mahler, B. Dubertret, E. Doris, and C. Mioskowski, "A Versatile Strategy for Quantum Dot Ligand Exchange," *Journal of the American Chemical Society*, vol. 129, pp. 482-483, 2007/01/01 2007.
- [134] W.-Y. Huang and J. J. Davis, "Multimodality and nanoparticles in medical imaging," *Dalton Transactions*, vol. 40, pp. 6087-6103, 2011.
- [135] S. K. Yen, P. Padmanabhan, and S. T. Selvan, "Multifunctional iron oxide nanoparticles for diagnostics, therapy and macromolecule delivery," *Theranostics*, vol. 3, p. 986, 2013.
- [136] H. Li, Z. Kang, Y. Liu, and S.-T. Lee, "Carbon nanodots: synthesis, properties and applications," *Journal of Materials Chemistry*, vol. 22, pp. 24230-24253, 2012.
- [137] S. N. Baker and G. A. Baker, "Luminescent Carbon Nanodots: Emergent Nanolights," *Angewandte Chemie International Edition*, vol. 49, pp. 6726-6744, 2010.
- [138] Y.-P. Sun, X. Wang, F. Lu, L. Cao, M. J. Meziani, P. G. Luo, *et al.*, "Doped Carbon Nanoparticles as a New Platform for Highly Photoluminescent Dots," *The Journal of Physical Chemistry C*, vol. 112, pp. 18295-18298, 2008/11/27 2008.
- [139] L. Tian, D. Ghosh, W. Chen, S. Pradhan, X. Chang, and S. Chen, "Nanosized Carbon Particles From Natural Gas Soot," *Chemistry of Materials*, vol. 21, pp. 2803-2809, 2009/07/14 2009.
- [140] P. G. Luo, S. Sahu, S.-T. Yang, S. K. Sonkar, J. Wang, H. Wang, *et al.*, "Carbon "quantum" dots for optical bioimaging," *Journal of Materials Chemistry B*, vol. 1, pp. 2116-2127, 2013.
- [141] L. Cao, P. Anilkumar, X. Wang, J.-H. Liu, S. Sahu, M. J. Meziani, *et al.*, "Reverse Stern–Volmer behavior for luminescence quenching in carbon nanoparticles," *Canadian Journal of Chemistry*, vol. 89, pp. 104-109, 2011/02/01 2010.
- [142] X. Li, H. Wang, Y. Shimizu, A. Pyatenko, K. Kawaguchi, and N. Koshizaki, "Preparation of carbon quantum dots with tunable photoluminescence by rapid laser passivation in ordinary organic solvents," *Chemical Communications*, vol. 47, pp. 932-934, 2011.
- [143] S.-L. Hu, K.-Y. Niu, J. Sun, J. Yang, N.-Q. Zhao, and X.-W. Du, "One-step synthesis of fluorescent carbon nanoparticles by laser irradiation," *Journal of Materials Chemistry*, vol. 19, pp. 484-488, 2009.

- [144] H. Li, X. He, Z. Kang, H. Huang, Y. Liu, J. Liu, *et al.*, "Water-Soluble Fluorescent Carbon Quantum Dots and Photocatalyst Design," *Angewandte Chemie International Edition*, vol. 49, pp. 4430-4434, 2010.
- [145] P. Anilkumar, X. Wang, L. Cao, S. Sahu, J.-H. Liu, P. Wang, *et al.*, "Toward quantitatively fluorescent carbon-based "quantum" dots," *Nanoscale*, vol. 3, pp. 2023-2027, 2011.
- [146] M. Schäferling, D. Dregely, M. Hentschel, and H. Giessen, "Tailoring enhanced optical chirality: design principles for chiral plasmonic nanostructures," *Physical Review X*, vol. 2, p. 031010, 2012.
- [147] E. C. Dreaden, A. M. Alkilany, X. Huang, C. J. Murphy, and M. A. El-Sayed, "The golden age: gold nanoparticles for biomedicine," *Chemical Society Reviews*, vol. 41, pp. 2740-2779, 2012.
- [148] M. Faraday, "The Bakerian lecture: experimental relations of gold (and other metals) to light," *Philosophical Transactions of the Royal Society of London*, vol. 147, pp. 145-181, 1857.
- [149] P. Zhao, N. Li, and D. Astruc, "State of the art in gold nanoparticle synthesis," *Coordination Chemistry Reviews*, vol. 257, pp. 638-665, 2013.
- [150] M. Grzelczak, J. Pérez-Juste, P. Mulvaney, and L. M. Liz-Marzán, "Shape control in gold nanoparticle synthesis," *Chemical Society Reviews*, vol. 37, pp. 1783-1791, 2008.
- [151] A. M. Alkilany, P. K. Nagaria, C. R. Hexel, T. J. Shaw, C. J. Murphy, and M. D. Wyatt, "Cellular uptake and cytotoxicity of gold nanorods: molecular origin of cytotoxicity and surface effects," *Small*, vol. 5, pp. 701-708, 2009.
- [152] R. Mout, D. F. Moyano, S. Rana, and V. M. Rotello, "Surface functionalization of nanoparticles for nanomedicine," *Chemical Society Reviews*, vol. 41, pp. 2539-2544, 2012.
- [153] A. Z. Wang, F. Gu, L. Zhang, J. M. Chan, A. Radovic-Moreno, M. R. Shaikh, *et al.*, "Biofunctionalized targeted nanoparticles for therapeutic applications," *Expert Opinion on Biological Therapy*, vol. 8, pp. 1063-1070, 2008.
- [154] M. Srinivasarao, C. V. Galliford, and P. S. Low, "Principles in the design of ligand-targeted cancer therapeutics and imaging agents," *Nature reviews Drug discovery*, vol. 14, p. 203, 2015.
- [155] P. D. Kaiser, J. Maier, B. Traenkle, F. Emele, and U. Rothbauer, "Recent progress in generating intracellular functional antibody fragments to target and trace cellular components in living cells," *Biochimica Et Biophysica Acta (BBA)-Proteins and Proteomics*, vol. 1844, pp. 1933-1942, 2014.
- [156] J. Zhou and J. Rossi, "Aptamers as targeted therapeutics: current potential and challenges," *Nature Reviews Drug Discovery*, vol. 16, p. 181, 2017.
- [157] P. S. Low and S. A. Kularatne, "Folate-targeted therapeutic and imaging agents for cancer," *Current Opinion in Chemical Biology*, vol. 13, pp. 256-262, 6// 2009.

- [158] F. Gu, L. Zhang, B. A. Teply, N. Mann, A. Wang, A. F. Radovic-Moreno, *et al.*, "Precise engineering of targeted nanoparticles by using self-assembled biointegrated block copolymers," *Proceedings of the National Academy of Sciences*, vol. 105, pp. 2586-2591, February 19, 2008 2008.
- [159] N. Dos Santos, C. Allen, A.-M. Doppen, M. Anantha, K. A. K. Cox, R. C. Gallagher, *et al.*, "Influence of poly(ethylene glycol) grafting density and polymer length on liposomes: Relating plasma circulation lifetimes to protein binding," *Biochimica et Biophysica Acta (BBA) - Biomembranes*, vol. 1768, pp. 1367-1377, 6// 2007.
- [160] F. Chiti and C. M. Dobson, "Protein misfolding, functional amyloid, and human disease," *Annu. Rev. Biochem.*, vol. 75, pp. 333-366, 2006.
- [161] L. M. Young, J. C. Saunders, R. A. Mahood, C. H. Revill, R. J. Foster, L.-H. Tu, *et al.*, "Screening and classifying small-molecule inhibitors of amyloid formation using ion mobility spectrometry–mass spectrometry," *Nature chemistry*, vol. 7, p. 73, 2015.
- [162] Q. Wang, X. Yu, L. Li, and J. Zheng, "Inhibition of amyloid- β aggregation in Alzheimer's disease," *Current pharmaceutical design*, vol. 20, pp. 1223-1243, 2014.
- [163] C. W. Ritchie, A. I. Bush, A. Mackinnon, S. Macfarlane, M. Mastwyk, L. MacGregor, *et al.*, "Metal-protein attenuation with iodochlorhydroxyquin (clioquinol) targeting A β amyloid deposition and toxicity in Alzheimer disease: a pilot phase 2 clinical trial," *Archives of neurology*, vol. 60, pp. 1685-1691, 2003.
- [164] A. C. McKee, I. Carreras, L. Hossain, H. Ryu, W. L. Klein, S. Oddo, *et al.*, "Ibuprofen reduces A β , hyperphosphorylated tau and memory deficits in Alzheimer mice," *Brain research*, vol. 1207, pp. 225-236, 2008.
- [165] B. Y. Feng, B. H. Toyama, H. Wille, D. W. Colby, S. R. Collins, B. C. May, *et al.*, "Small-molecule aggregates inhibit amyloid polymerization," *Nature chemical biology*, vol. 4, p. 197, 2008.
- [166] A. Abelein, B. Bolognesi, C. M. Dobson, A. Gräslund, and C. Lendel, "Hydrophobicity and conformational change as mechanistic determinants for nonspecific modulators of amyloid β self-assembly," *Biochemistry*, vol. 51, pp. 126-137, 2011.
- [167] L. Whitmore and B. A. Wallace, "Protein secondary structure analyses from circular dichroism spectroscopy: methods and reference databases," *Biopolymers*, vol. 89, pp. 392-400, 2008.
- [168] G. Son, B. I. Lee, Y. J. Chung, and C. B. Park, "Light-triggered dissociation of self-assembled β -amyloid aggregates into small, nontoxic fragments by ruthenium (II) complex," *Acta biomaterialia*, 2017.
- [169] S. Sharma, B. Nehru, and A. Saini, "Inhibition of Alzheimer's amyloid-beta aggregation in-vitro by carbenoxolone: Insight into mechanism of action," *Neurochemistry international*, vol. 108, pp. 481-493, 2017.

- [170] J. Ni, A. Taniguchi, S. Ozawa, Y. Hori, Y. Kuninobu, T. Saito, *et al.*, "Near-infrared photoactivatable oxygenation catalysts of amyloid peptide," *Chem*, vol. 4, pp. 807-820, 2018.
- [171] J. Bieschke, M. Herbst, T. Wiglenda, R. P. Friedrich, A. Boeddrich, F. Schiele, *et al.*, "Small-molecule conversion of toxic oligomers to nontoxic β -sheet-rich amyloid fibrils," *Nature chemical biology*, vol. 8, p. 93, 2012.
- [172] Q. I. Churches, J. Caine, K. Cavanagh, V. C. Epa, L. Waddington, C. E. Tranberg, *et al.*, "Naturally occurring polyphenolic inhibitors of amyloid beta aggregation," *Bioorganic & medicinal chemistry letters*, vol. 24, pp. 3108-3112, 2014.
- [173] G. W. Arendash and C. Cao, "Caffeine and coffee as therapeutics against Alzheimer's disease," *Journal of Alzheimer's Disease*, vol. 20, pp. S117-S126, 2010.
- [174] R. A. Orlando, A. M. Gonzales, R. E. Royer, L. M. Deck, and D. L. Vander Jagt, "A chemical analog of curcumin as an improved inhibitor of amyloid Abeta oligomerization," *PloS one*, vol. 7, p. e31869, 2012.
- [175] A. Thapa, S. D. Jett, and E. Y. Chi, "Curcumin attenuates amyloid- β aggregate toxicity and modulates amyloid- β aggregation pathway," *ACS chemical neuroscience*, vol. 7, pp. 56-68, 2015.
- [176] F. Re, C. Airolidi, C. Zona, M. Masserini, B. L. Ferla, N. Quattrocchi, *et al.*, "Beta amyloid aggregation inhibitors: small molecules as candidate drugs for therapy of Alzheimer's disease," *Current medicinal chemistry*, vol. 17, pp. 2990-3006, 2010.
- [177] K. L. Sciarretta, D. J. Gordon, and S. C. Meredith, "Peptide - based inhibitors of amyloid assembly," *Methods in enzymology*, vol. 413, pp. 273-312, 2006.
- [178] M. Carballo-Pacheco, A. E. Ismail, and B. Strodel, "Oligomer formation of toxic and functional amyloid peptides studied with atomistic simulations," *The Journal of Physical Chemistry B*, vol. 119, pp. 9696-9705, 2015.
- [179] N. G. Sgourakis, Y. Yan, S. A. McCallum, C. Wang, and A. E. Garcia, "The Alzheimer's peptides A β 40 and 42 adopt distinct conformations in water: a combined MD/NMR study," *Journal of molecular biology*, vol. 368, pp. 1448-1457, 2007.
- [180] B. Urbanc, L. Cruz, S. Yun, S. V. Buldyrev, G. Bitan, D. B. Teplow, *et al.*, "In silico study of amyloid β -protein folding and oligomerization," *Proceedings of the National Academy of Sciences of the United States of America*, vol. 101, pp. 17345-17350, 2004.
- [181] Z. Chen, G. Krause, and B. Reif, "Structure and orientation of peptide inhibitors bound to beta-amyloid fibrils," *Journal of molecular biology*, vol. 354, pp. 760-776, 2005.
- [182] G. Yamin, P. Ruchala, and D. B. Teplow, "A peptide hairpin inhibitor of amyloid β -protein oligomerization and fibrillogenesis," *Biochemistry*, vol. 48, pp. 11329-11331, 2009.

- [183] N. Rezaei-Ghaleh, E. Andreetto, L.-M. Yan, A. Kapurniotu, and M. Zweckstetter, "Interaction between amyloid beta peptide and an aggregation blocker peptide mimicking islet amyloid polypeptide," *PLoS One*, vol. 6, p. e20289, 2011.
- [184] K. E. Marshall, K. L. Morris, D. Charlton, N. O'Reilly, L. Lewis, H. Walden, *et al.*, "Hydrophobic, aromatic, and electrostatic interactions play a central role in amyloid fibril formation and stability," *Biochemistry*, vol. 50, pp. 2061-2071, 2011.
- [185] H. Liu, B. Ojha, C. Morris, M. Jiang, E. P. Wojcikiewicz, P. P. Rao, *et al.*, "Positively charged chitosan and N-trimethyl chitosan inhibit A β 40 fibrillogenesis," *Biomacromolecules*, vol. 16, pp. 2363-2373, 2015.
- [186] Y. H. Liao, Y. J. Chang, Y. Yoshiike, Y. C. Chang, and Y. R. Chen, "Negatively Charged Gold Nanoparticles Inhibit Alzheimer's Amyloid - β Fibrillization, Induce Fibril Dissociation, and Mitigate Neurotoxicity," *Small*, vol. 8, pp. 3631-3639, 2012.
- [187] H. Liu, B. Xie, X. Dong, L. Zhang, Y. Wang, F. Liu, *et al.*, "Negatively charged hydrophobic nanoparticles inhibit amyloid β -protein fibrillation: the presence of an optimal charge density," *Reactive and Functional Polymers*, vol. 103, pp. 108-116, 2016.
- [188] H.-M. Chan, L. Xiao, K.-M. Yeung, S.-L. Ho, D. Zhao, W.-H. Chan, *et al.*, "Effect of surface-functionalized nanoparticles on the elongation phase of beta-amyloid (1–40) fibrillogenesis," *Biomaterials*, vol. 33, pp. 4443-4450, 2012.
- [189] A. Assarsson, E. Hellstrand, C. Cabaleiro-Lago, and S. Linse, "Charge dependent retardation of amyloid β aggregation by hydrophilic proteins," *ACS chemical neuroscience*, vol. 5, pp. 266-274, 2014.
- [190] S. Sudhakar, P. Kalipillai, P. B. Santhosh, and E. Mani, "Role of Surface Charge of Inhibitors on Amyloid Beta Fibrillation," *The Journal of Physical Chemistry C*, vol. 121, pp. 6339-6348, 2017.
- [191] Z. Jiang, X. Dong, and Y. Sun, "Charge effects of self-assembled chitosan-hyaluronic acid nanoparticles on inhibiting amyloid β -protein aggregation," *Carbohydrate Research*, 2018.
- [192] X. Han, Z. Jing, W. Wu, B. Zou, Z. Peng, P. Ren, *et al.*, "Biocompatible and blood–brain barrier permeable carbon dots for inhibition of A β fibrillation and toxicity, and BACE1 activity," *Nanoscale*, vol. 9, pp. 12862-12866, 2017.
- [193] A. Bobylev, A. Kornev, L. Bobyleva, M. Shpagina, I. Fadeeva, R. Fadeev, *et al.*, "Fullerenolates: metallated polyhydroxylated fullerenes with potent anti-amyloid activity," *Organic & biomolecular chemistry*, vol. 9, pp. 5714-5719, 2011.
- [194] H. Li, Y. Luo, P. Derreumaux, and G. Wei, "Carbon nanotube inhibits the formation of β -sheet-rich oligomers of the Alzheimer's amyloid- β (16-22) peptide," *Biophysical journal*, vol. 101, pp. 2267-2276, 2011.
- [195] M. Mahmoudi, O. Akhavan, M. Ghavami, F. Rezaee, and S. M. A. Ghiasi, "Graphene oxide strongly inhibits amyloid beta fibrillation," *Nanoscale*, vol. 4, pp. 7322-7325, 2012.

- [196] J. Luo, S. K. Wärmländer, C.-H. Yu, K. Muhammad, A. Gräslund, and J. P. Abrahams, "The A β peptide forms non-amyloid fibrils in the presence of carbon nanotubes," *Nanoscale*, vol. 6, pp. 6720-6726, 2014.
- [197] L. Xie, Y. Luo, D. Lin, W. Xi, X. Yang, and G. Wei, "The molecular mechanism of fullerene-inhibited aggregation of Alzheimer's β -amyloid peptide fragment," *Nanoscale*, vol. 6, pp. 9752-9762, 2014.
- [198] Y. Liu, L.-P. Xu, W. Dai, H. Dong, Y. Wen, and X. Zhang, "Graphene quantum dots for the inhibition of β amyloid aggregation," *Nanoscale*, vol. 7, pp. 19060-19065, 2015.
- [199] T. Yin, W. Xie, J. Sun, L. Yang, and J. Liu, "Penetratin peptide-functionalized gold nanostars: enhanced BBB permeability and NIR photothermal treatment of Alzheimer's disease using ultralow irradiance," *ACS applied materials & interfaces*, vol. 8, pp. 19291-19302, 2016.
- [200] G. Liu, P. Men, W. Kudo, G. Perry, and M. A. Smith, "Nanoparticle–chelator conjugates as inhibitors of amyloid- β aggregation and neurotoxicity: a novel therapeutic approach for Alzheimer disease," *Neuroscience letters*, vol. 455, pp. 187-190, 2009.
- [201] H. Skaat, G. Shafir, and S. Margel, "Acceleration and inhibition of amyloid- β fibril formation by peptide-conjugated fluorescent-maghemite nanoparticles," *Journal of Nanoparticle Research*, vol. 13, pp. 3521-3534, 2011.
- [202] M. Yu and J. Zheng, "Clearance pathways and tumor targeting of imaging nanoparticles," *ACS nano*, vol. 9, pp. 6655-6674, 2015.
- [203] F. Alexis, E. Pridgen, L. K. Molnar, and O. C. Farokhzad, "Factors affecting the clearance and biodistribution of polymeric nanoparticles," *Molecular pharmaceuticals*, vol. 5, pp. 505-515, 2008.
- [204] H. Arami, A. Khandhar, D. Liggitt, and K. M. Krishnan, "In vivo delivery, pharmacokinetics, biodistribution and toxicity of iron oxide nanoparticles," *Chemical Society Reviews*, vol. 44, pp. 8576-8607, 2015.
- [205] C. Disdier, J. Devoy, A. Cosnefroy, M. Chalansonnet, N. Herlin-Boime, E. Brun, *et al.*, "Tissue biodistribution of intravenously administrated titanium dioxide nanoparticles revealed blood-brain barrier clearance and brain inflammation in rat," *Particle and fibre toxicology*, vol. 12, p. 27, 2015.
- [206] L. Zheng and Y. Hu, "The study of blue LED to induce fluorescence spectroscopy and fluorescence imaging for oral carcinoma detection," in *Proc. of SPIE Vol*, 2009, pp. 73821B-1.
- [207] G. f. Du, C. z. Li, H. z. Chen, X. m. Chen, Q. Xiao, Z. g. Cao, *et al.*, "Rose bengal staining in detection of oral precancerous and malignant lesions with colorimetric evaluation: a pilot study," *International journal of cancer*, vol. 120, pp. 1958-1963, 2007.

- [208] J. Kneipp, H. Kneipp, A. Rajadurai, R. W. Redmond, and K. Kneipp, "Optical probing and imaging of live cells using SERS labels," *Journal of Raman Spectroscopy*, vol. 40, pp. 1-5, 2009.
- [209] H. E. Wong, J. A. Irwin, and I. Kwon, "Halogenation generates effective modulators of amyloid-Beta aggregation and neurotoxicity," *PloS one*, vol. 8, p. e57288, 2013.
- [210] F. Tian, F. Bonnier, A. Casey, A. E. Shanahan, and H. J. Byrne, "Surface enhanced Raman scattering with gold nanoparticles: effect of particle shape," *Analytical Methods*, vol. 6, pp. 9116-9123, 2014.
- [211] E. Panzarini, V. Inguscio, and L. Dini, "Timing the multiple cell death pathways initiated by Rose Bengal acetate photodynamic therapy," *Cell death & disease*, vol. 2, p. e169, 2011.
- [212] B. Wang, J.-H. Wang, Q. Liu, H. Huang, M. Chen, K. Li, *et al.*, "Rose-bengal-conjugated gold nanorods for in vivo photodynamic and photothermal oral cancer therapies," *Biomaterials*, vol. 35, pp. 1954-1966, 2014.
- [213] R. Toy, P. M. Peiris, K. B. Ghaghada, and E. Karathanasis, "Shaping cancer nanomedicine: the effect of particle shape on the in vivo journey of nanoparticles," *Nanomedicine*, vol. 9, pp. 121-134, 2014.
- [214] S. K. Ghosh, S. Nath, S. Kundu, K. Esumi, and T. Pal, "Solvent and Ligand Effects on the Localized Surface Plasmon Resonance (LSPR) of Gold Colloids," *The Journal of Physical Chemistry B*, vol. 108, pp. 13963-13971, 2004/09/01 2004.
- [215] J.-H. Wang, B. Wang, Q. Liu, Q. Li, H. Huang, L. Song, *et al.*, "Bimodal optical diagnostics of oral cancer based on Rose Bengal conjugated gold nanorod platform," *Biomaterials*, vol. 34, pp. 4274-4283, 2013.
- [216] E. Dulkeith, T. Niedereichholz, T. Klar, J. Feldmann, G. Von Plessen, D. Gittins, *et al.*, "Plasmon emission in photoexcited gold nanoparticles," *Physical Review B*, vol. 70, p. 205424, 2004.
- [217] J. van Meerloo, G. J. Kaspers, and J. Cloos, "Cell sensitivity assays: the MTT assay," in *Cancer cell culture*, ed: Springer, 2011, pp. 237-245.
- [218] A. Uppal, B. Jain, P. K. Gupta, and K. Das, "Photodynamic action of Rose Bengal silica nanoparticle complex on breast and oral cancer cell lines," *Photochemistry and photobiology*, vol. 87, pp. 1146-1151, 2011.
- [219] S. Wang, K. Li, Y. Chen, H. Chen, M. Ma, J. Feng, *et al.*, "Biocompatible PEGylated MoS₂ nanosheets: Controllable bottom-up synthesis and highly efficient photothermal regression of tumor," *Biomaterials*, vol. 39, pp. 206-217, 2015.
- [220] G. Socrates, *Infrared and Raman characteristic group frequencies: tables and charts*: John Wiley & Sons, 2001.

- [221] T. Vosgröne and A. Meixner, "Surface - and Resonance - Enhanced Micro - Raman Spectroscopy of Xanthene Dyes: From the Ensemble to Single Molecules," *ChemPhysChem*, vol. 6, pp. 154-163, 2005.
- [222] A. M. Gabudean, M. Focsan, and S. Astilean, "Gold nanorods performing as dual-modal nanoprobe via metal-enhanced fluorescence (MEF) and surface-enhanced Raman scattering (SERS)," *The Journal of Physical Chemistry C*, vol. 116, pp. 12240-12249, 2012.
- [223] M. Zhu, S. Rajamani, J. Kaylor, S. Han, F. Zhou, and A. L. Fink, "The flavonoid baicalein inhibits fibrillation of α -synuclein and disaggregates existing fibrils," *Journal of Biological Chemistry*, vol. 279, pp. 26846-26857, 2004.
- [224] W. Yang, Y. Wong, O. T. Ng, L. P. Bai, D. W. Kwong, Y. Ke, *et al.*, "Inhibition of Beta - Amyloid Peptide Aggregation by Multifunctional Carbazole - Based Fluorophores," *Angewandte Chemie International Edition*, vol. 51, pp. 1804-1810, 2012.
- [225] N. P. Cook, K. Kilpatrick, L. Segatori, and A. A. Martí, "Detection of α -synuclein amyloidogenic aggregates in vitro and in cells using light-switching dipyrrophenazine ruthenium (ii) complexes," *Journal of the American Chemical Society*, vol. 134, pp. 20776-20782, 2012.
- [226] P. Murasecco - Suardi, E. Gassmann, A. M. Braun, and E. Oliveros, "Determination of the quantum yield of intersystem crossing of rose bengal," *Helvetica chimica acta*, vol. 70, pp. 1760-1773, 1987.
- [227] S. Radic, T. P. Davis, P. C. Ke, and F. Ding, "Contrasting effects of nanoparticle-protein attraction on amyloid aggregation," *RSC advances*, vol. 5, pp. 105489-105498, 2015.
- [228] M. Wang, A. Kakinen, E. H. Pilkington, T. P. Davis, and P. C. Ke, "Differential effects of silver and iron oxide nanoparticles on IAPP amyloid aggregation," *Biomaterials science*, vol. 5, pp. 485-493, 2017.
- [229] J. Perumal, K. V. Kong, U. Dinish, R. M. Bakker, and M. Olivo, "Design and fabrication of random silver films as substrate for SERS based nano-stress sensing of proteins," *RSC Advances*, vol. 4, pp. 12995-13000, 2014.
- [230] N. T. Bailey, *Statistical methods in biology*: Cambridge university press, 1995.
- [231] M. Krzywinski and N. Altman, "Points of significance: Significance, P values and t-tests," ed: Nature Publishing Group, 2013.
- [232] T. Lagache, N. Sauvonnet, L. Danglot, and J. C. Olivo - Marin, "Statistical analysis of molecule colocalization in bioimaging," *Cytometry Part A*, vol. 87, pp. 568-579, 2015.
- [233] M. Ahmed, J. Davis, D. Aucoin, T. Sato, S. Ahuja, S. Aimoto, *et al.*, "Structural conversion of neurotoxic amyloid- β 1-42 oligomers to fibrils," *Nature Structural and Molecular Biology*, vol. 17, p. 561, 2010.

- [234] T. Lühres, C. Ritter, M. Adrian, D. Riek-Loher, B. Bohrmann, H. Döbeli, *et al.*, "3D structure of Alzheimer's amyloid- β (1–42) fibrils," *Proceedings of the National Academy of Sciences of the United States of America*, vol. 102, pp. 17342-17347, 2005.
- [235] L.-P. Xu, Y. Liu, and X. Zhang, "Interfacial self-assembly of amino acids and peptides: Scanning tunneling microscopy investigation," *Nanoscale*, vol. 3, pp. 4901-4915, 2011.
- [236] N. Gong, H. Wang, S. Li, Y. Deng, X. a. Chen, L. Ye, *et al.*, "Microwave-Assisted Polyol Synthesis of Gadolinium-Doped Green Luminescent Carbon Dots as a Bimodal Nanoprobe," *Langmuir*, vol. 30, pp. 10933-10939, 2014/09/16 2014.
- [237] X. Jia, J. Li, and E. Wang, "One-pot green synthesis of optically pH-sensitive carbon dots with upconversion luminescence," *Nanoscale*, vol. 4, pp. 5572-5575, 2012.
- [238] L. Wang and H. S. Zhou, "Green synthesis of luminescent nitrogen-doped carbon dots from milk and its imaging application," *Analytical chemistry*, vol. 86, pp. 8902-8905, 2014.
- [239] H. Wang and X. Wang, "In vitro nucleus nanoprobe with ultra-small polyethylenimine functionalized graphene quantum dots," *Rsc Advances*, vol. 5, pp. 75380-75385, 2015.
- [240] L. Yuan, W. Lin, and H. Chen, "Analogues of Changsha near-infrared dyes with large Stokes Shifts for bioimaging," *Biomaterials*, vol. 34, pp. 9566-9571, 2013.
- [241] J. Kovalevich and D. Langford, "Considerations for the use of SH-SY5Y neuroblastoma cells in neurobiology," in *Neuronal Cell Culture*, ed: Springer, 2013, pp. 9-21.
- [242] H. Xicoy, B. Wieringa, and G. J. M. Martens, "The SH-SY5Y cell line in Parkinson's disease research: a systematic review," *Molecular Neurodegeneration*, vol. 12, p. 10, January 24 2017.
- [243] A. S. Pai, I. Rubinstein, and H. Önyüksel, "PEGylated phospholipid nanomicelles interact with β -amyloid (1–42) and mitigate its β -sheet formation, aggregation and neurotoxicity in vitro," *Peptides*, vol. 27, pp. 2858-2866, 2006.
- [244] D. Brambilla, R. Verpillot, B. Le Droumaguet, J. Nicolas, M. Taverna, J. Kóňa, *et al.*, "PEGylated nanoparticles bind to and alter amyloid-beta peptide conformation: toward engineering of functional nanomedicines for Alzheimer's disease," *ACS nano*, vol. 6, pp. 5897-5908, 2012.
- [245] S. Mirsadeghi, S. Shanehsazzadeh, F. Atyabi, and R. Dinarvand, "Effect of PEGylated superparamagnetic iron oxide nanoparticles (SPIONs) under magnetic field on amyloid beta fibrillation process," *Materials Science and Engineering: C*, vol. 59, pp. 390-397, 2016.
- [246] A. Delgado, F. Gonzalez-Caballero, and J. Bruque, "On the zeta potential and surface charge density of montmorillonite in aqueous electrolyte solutions," *Journal of colloid and interface science*, vol. 113, pp. 203-211, 1986.

- [247] R. D. Terry, "The pathogenesis of Alzheimer disease: an alternative to the amyloid hypothesis," *Journal of Neuropathology & Experimental Neurology*, vol. 55, pp. 1023-1025, 1996.
- [248] T. Umeda, T. Tomiyama, N. Sakama, S. Tanaka, M. P. Lambert, W. L. Klein, *et al.*, "Intraneuronal amyloid β oligomers cause cell death via endoplasmic reticulum stress, endosomal/lysosomal leakage, and mitochondrial dysfunction in vivo," *Journal of neuroscience research*, vol. 89, pp. 1031-1042, 2011.
- [249] S. Nath, L. Agholme, F. R. Kurudenkandy, B. Granseth, J. Marcusson, and M. Hallbeck, "Spreading of neurodegenerative pathology via neuron-to-neuron transmission of β -amyloid," *Journal of Neuroscience*, vol. 32, pp. 8767-8777, 2012.
- [250] O. Veisheh, J. W. Gunn, and M. Zhang, "Design and fabrication of magnetic nanoparticles for targeted drug delivery and imaging," *Advanced Drug Delivery Reviews*, vol. 62, pp. 284-304, 3/8/ 2010.
- [251] S. Laurent, A. A. Saei, S. Behzadi, A. Panahifar, and M. Mahmoudi, "Superparamagnetic iron oxide nanoparticles for delivery of therapeutic agents: opportunities and challenges," *Expert opinion on drug delivery*, vol. 11, pp. 1449-1470, 2014.
- [252] S. Mura, J. Nicolas, and P. Couvreur, "Stimuli-responsive nanocarriers for drug delivery," *Nature materials*, vol. 12, p. 991, 2013.
- [253] C. A. Quinto, P. Mohindra, S. Tong, and G. Bao, "Multifunctional superparamagnetic iron oxide nanoparticles for combined chemotherapy and hyperthermia cancer treatment," *Nanoscale*, vol. 7, pp. 12728-12736, 2015.
- [254] E. Ruoslahti, "Peptides as targeting elements and tissue penetration devices for nanoparticles," *Advanced materials*, vol. 24, pp. 3747-3756, 2012.
- [255] E. Koren and V. P. Torchilin, "Cell-penetrating peptides: breaking through to the other side," *Trends in molecular medicine*, vol. 18, pp. 385-393, 2012.
- [256] E. Vivès, J. Schmidt, and A. Pèlegri, "Cell-penetrating and cell-targeting peptides in drug delivery," *Biochimica et Biophysica Acta (BBA)-Reviews on Cancer*, vol. 1786, pp. 126-138, 2008.
- [257] W. J. M. Mulder, A. W. Griffioen, G. J. Strijkers, D. P. Cormode, K. Nicolay, and Z. A. Fayad, "Magnetic and fluorescent nanoparticles for multimodality imaging," *Nanomedicine*, vol. 2, pp. 307-324, 2007/06/01 2007.
- [258] G. S. Paranjape, S. E. Terrill, L. K. Gouwens, B. M. Ruck, and M. R. Nichols, "Amyloid- β (1-42) protofibrils formed in modified artificial cerebrospinal fluid bind and activate microglia," *Journal of NeuroImmune Pharmacology*, vol. 8, pp. 312-322, 2013.
- [259] H. Wang, J. Ma, Y. Tan, Z. Wang, C. Sheng, S. Chen, *et al.*, "Amyloid- β 1-42 induces reactive oxygen species-mediated autophagic cell death in U87 and SH-SY5Y cells," *Journal of Alzheimer's Disease*, vol. 21, pp. 597-610, 2010.

-
- [260] É. Tóth, L. Helm, and A. E. Merbach, "Relaxivity of MRI contrast agents," in *Contrast Agents I*, ed: Springer, 2002, pp. 61-101.
- [261] S. Dumas, V. Jacques, W.-C. Sun, J. S. Troughton, J. T. Welch, J. M. Chasse, *et al.*, "High relaxivity MRI contrast agents part 1: Impact of single donor atom substitution on relaxivity of serum albumin-bound gadolinium complexes," *Investigative radiology*, vol. 45, p. 600, 2010.
- [262] H. Duan, M. Kuang, X. Wang, Y. A. Wang, H. Mao, and S. Nie, "Reexamining the effects of particle size and surface chemistry on the magnetic properties of iron oxide nanocrystals: new insights into spin disorder and proton relaxivity," *The Journal of Physical Chemistry C*, vol. 112, pp. 8127-8131, 2008.
- [263] N. Wanichacheva, O. Hanmeng, S. Kraithong, and K. Sukrat, "Dual optical Hg²⁺-selective sensing through FRET system of fluorescein and rhodamine B fluorophores," *Journal of Photochemistry and Photobiology A: Chemistry*, vol. 278, pp. 75-81, 2014.
- [264] E. Yavin and Z. Yavin, "Attachment and culture of dissociated cells from rat embryo cerebral hemispheres on polylysine-coated surface," *The Journal of cell biology*, vol. 62, p. 540, 1974.